UNIVERSIDAD DE CHILE
FACULTAD DE CIENCIAS FÍSICAS Y MATEMÁTICAS
DEPARTAMENTO DE ASTRONOMÍA

# STUDYING SPIRAL STRUCTURES IN PROTOPLANETARY DISKS THROUGH MULTI-WAVELENGTH ALMA OBSERVATIONS

TESIS PARA OPTAR AL GRADO DE MAGÍSTER EN CIENCIAS,
MENCIÓN ASTRONOMÍA

**TERESA PAZ PANEQUE CARREÑO**

PROFESORA GUÍA:
LAURA PÉREZ MUÑOZ

MIEMBROS DE LA COMISIÓN:
MYRIAM BENISTY
GIUSEPPE LODATO
JAMES JENKINS

Este trabajo ha sido parcialmente financiado por:

FONDECYT Iniciación project #11181068,
National Aeronautics and Space Administration
under grant No. 15XRP15_20140
issued through the Exoplanets Research Program.

SANTIAGO DE CHILE
2020

RESUMEN DE LA TESIS PARA OPTAR
AL TÍTULO DE MAGÍSTER EN CIENCIAS
POR: **TERESA PAZ PANEQUE CARREÑO**
FECHA: 2020
PROF. GUÍA: LAURA PÉREZ MUÑOZ

# STUDYING SPIRAL STRUCTURES IN PROTOPLANETARY DISKS THROUGH MULTI-WAVELENGTH ALMA OBSERVATIONS

Estudiar las estructuras presentes en discos protoplanetarios nos permite caracterizar los procesos dinámicos en ellos. Específicamente, las estructuras espirales tienen dos posibles orígenes, inestabilidades gravitacionales en un disco masivo o la presencia de un cuerpo, ligado o no, al sistema. En pocos discos protoplanetarios en se han observado estructuras espirales en longitudes de onda milimétricas, lo cual hace el estudio de estos sistemas particularmente interesante. En esta tesis analizamos el caso de Elias 2-27, un sistema jóven que alberga un disco inusualmente masivo. Debido a su alto cuociente de masa disco-estrella ($\sim$0.3) es candidato a ser el primer disco observado con inestabilidades gravitacionales. Alternativamente, la estructura espiral de Elias 2-27 podría ser provocada por un planeta aun no detectado.

Analizamos observaciones ALMA de lineas espectrales y polvo en múltiples longitudes de onda para Elias 2-27, buscando determinar el origen de la estructura espiral observada en el polvo. Nuestra meta es derivar nuevas características observacionales y determinar si existe atrapamiento de sólidos, desviaciones de movimiento Kepleriano, o cualquier indicador que favorezca algún origen para la estructura espiral. Los sólidos son observados a través de observaciones con resolución de $\sim$0.2 arcsec ($\sim$23 ua) en 0.89mm, 1.3mm and 3.3mm, la componente gaseosa y su cinemática son observadas usando $^{13}$CO y C$^{18}$O, en la transición $J$ =3-2 y moléculas de CN en las transiciones $J = 7/2 - 5/2$ y $J = 5/2 - 3/2$.

En las observaciones de polvo aplicamos técnicas de sustracción para destacar la estructura espiral y trazar la morfología en cada una de las longitudes de onda estudiadas. También medimos las variaciones de contraste e índice espectral a lo largo de las espirales, buscando señales de atrapamiento de partículas. Aplicamos el método de Pinte et al. (2018a) a los isotopólogos de CO para trazar la morfología de la superficie de emisión de $^{13}$CO y C$^{18}$O y obtener el perfil de velocidad. Con lo anterior, obtenemos el perfil radial de altura para la superficie de emisión y una medición independiente de la masa estelar para el sistema. Buscamos desviaciones de movimiento Kepleriano a través del análisis de residuos de los mapas de velocidad y perturbaciones presentes en los canales de velocidad, usando las curvas esperadas de isovelocidades. La emisión de CN es únicamente caracterizada a través de sus características morfológicas principales. También desarrollamos y comparamos las observaciones de polvo y gas con simulaciones hidrodinámicas de un disco gravitacionalmente inestable.

Trazamos la estructura espiral en todas las observaciones de polvo, la morfología es simétrica y con ángulo característico relativamente constante a distintas longitudes de onda. Detectamos señales tenues de atrapamiento de partículas en el análisis de contraste e índice espectral. De las observaciones de gas trazamos una altura de la superficie emisora asimétrica y variable azimutalmente. Detectamos emisión de gran escala en torno al disco y fuertes perturbaciones en la ubicación de las espirales, en los canales de velocidad. Considerando las características observadas y las similitudes con simulaciones hidrodinámicas, proponemos inestabilidades gravitacionales, inducidas por la caida de material sobre el disco, son el origen de la estructura espiral observada en Elias 2-27.

RESUMEN DE LA TESIS PARA OPTAR
AL TÍTULO DE MAGÍSTER EN CIENCIAS
POR: **TERESA PAZ PANEQUE CARREÑO**
FECHA: 2020
PROF. GUÍA: LAURA PÉREZ MUÑOZ

## STUDYING SPIRAL STRUCTURES IN PROTOPLANETARY DISKS THROUGH MULTI-WAVELENGTH ALMA OBSERVATIONS

Studying the structure present in protoplanetary disks offers an insight into the ongoing dynamical processes. Spiral structures are associated with either a massive, gravitationally unstable disk or the presence of a bound or unbound companion. There are few protoplanetary disks in which spiral structures have been observed at millimeter wavelengths, making the study of these sources particularly interesting. In this thesis we analyze the case of Elias 2-27, a young system that harbours an unusually large disk, due to its large disk-to-star mass ratio ($\sim$0.3) it is a candidate for being the first observed disk that is undergoing gravitational instabilities. Alternatively, the spiral arm structure of Elias 2-27 could also be produced by an undetected planetary companion.

We analyze multi-wavelength continuum and spectral line ALMA observations of Elias 2-27 to determine the origin of the spiral substructure observed in the dust. Our goal is to derive new observational constraints on this system and test for dust-trapping, deviations from Keplerian motion, or any other indicator that may favor a spiral-formation scenario. The solids are traced by dust continuum observations at a resolution of $\sim$0.2 arcsec ($\sim$23 au) at 0.89mm, 1.3mm and 3.3mm, while the gaseous component and its kinematics are traced by $^{13}$CO and C$^{18}$O observations in the $J$ =3-2 transition and CN $N = 3 - 2$ molecules in $J = 7/2 - 5/2$ and $J = 5/2 - 3/2$ transitions.

In the continuum, we apply subtraction techniques to enhance the spiral structure and delineate the morphology at the observed wavelengths. We also measure contrast and spectral index variations along the spiral arms to test for dust-trapping signatures. To the CO isotopologues, we apply the method of Pinte et al. (2018a) to trace the morphology of the $^{13}$CO and C$^{18}$O emitting surface and the velocity profile. From this, we determine a height profile for the emitting surface and an independent stellar-mass measurement of the system. We test for deviations from Keplerian motion through residual analysis of the velocity map and perturbations from the expected isovelocity curves in the channel maps. The CN emission is characterized through its main morphological features only. We also develop and compare the observations of dust and gas to hydrodynamical simulations of a gravitationally unstable disk.

The spiral structure is traced at all wavelengths in the dust continuum observations, with a symmetric morphology and roughly constant pitch angle across varying wavelengths. We detect subtle dust-trapping signatures in the contrast and spectral index analysis. From the gas observations, we determine that there is an azimuthally varying, highly assymmetric, scale height in the system. We observe large-scale emission surrounding the disk, and detect strong perturbations in the channel maps, co-located with the spiral arm location. Finally, considering the derived observational constrains and the similarities with the hydrodynamical simulations, we propose infall-triggered gravitational instability as the origin of the observed spiral structure of Elias 2-27.

*A mis padres, Paz y Manuel*
*por enseñarme de familia, amor y ciencia.*

# Agradecimientos

Terminar esta tesis, durante un año como el 2020, fue un trabajo en equipo. Me siento profundamente agradecida y afortunada de haber estado rodeada de amor y apoyo incondicional.

En primer lugar, gracias Mamá, eres la mujer más increíble que conozco, gracias por compartir tus experiencias de vida conmigo, por hacerme reír y haber sido mi compañera de yoga, trabajo y escritorio durante estos meses, eres mi mejor amiga. A mi Papá, gracias por haberme enseñado a ser valiente, a levantar la voz, por siempre haberme apoyado e impulsado a ir más lejos y por tus comentarios sobre mi "papel". A mis hermanos, Carlos y Miguel, me inspiran día a día con sus logros, me hacen buscar que el mundo sea un mejor lugar para ustedes. Gracias por tantas risas al almuerzo, por apoyarme en todos mis proyectos de difusión, son los mejores ayudantes. Gracias a mis abuelas, Norma y Nivia, independiente de la distancia siempre han estado presentes en todos los momentos de mi vida. A mis abuelos, Carlos y Manolo, que siempre han estado y continuarán estando a mi lado. A todas mis tías y tíos, a mis primos, me siento tremendamente afortunada de la familia gigante que me apoya y con quienes siempre cuento, especialmente gracias a mi Tía Pink. A mi segunda familia, Juan, Elena, Julio, Abi, los adoro con todo mi corazón. A la Sra. Sandra y Tía Vero, por tantas risas, cariño y conversaciones. A los amores de mi vida, Kuky, Pedro y Flora.

A mi profesora, Laura Pérez, gracias por la confianza de entregarme los datos de Elias 27, por la dedicación al enseñarme tantas herramientas y buscar siempre maximizar mi aprendizaje, por los espacios de conversación. Te considero una referente e inspiración, espero algún día volver a trabajar juntas en el mismo grupo. A mi comisión, James, Giuseppe y Myriam, tengo la suerte de haber podido trabajar y aprender de todos ustedes, gracias por tantas oportunidades y apoyo.

Cuando todo se veía gris y no sabía cómo escribir un paper, alguien me habló del Síndrome del Impostor y me re-encantó con la física y el trabajo académico. Gracias Rodrigo, a ti y a tu familia, por tantos Domingos y tardes de estudio, por tu ayuda en todos los temas físicos y muchísimo más.

Lucas, solo nosotros sabemos cuánto nos hemos apoyado este año, gracias por ser de esas amistades que nunca van a desaparecer, por tu asertividad y cariño. Sca, porque eres increíble, tu amistad, tu dulzura y tus consejos son invaluables, gracias infinitas. Esteban, jamás habría pensado que ibas a ser la persona a la que recurrir cuando todo se rompía a mi alrededor, gracias por escuchar, por tu paciencia y franqueza. Simón, no hay palabras para agradecerte, gracias por confiar en mí desde primer año, por haber permanecido y por el vínculo que compartimos. Coni, porque todo es más lindo después de una ida a tu casa, comida, gatas y conversación, gracias bella.

A mis amigas del colegio, Cele, Kta, Pame, Scarlett, gracias por nuestras juntas, conversaciones y confianza. José y Tere, sin ustedes no habría superado especialidad, gracias por cuidarme. A Andrea Puccio, gracias por tu dedicación, profesionalismo y amistad. Jorge, porque conocerte, las videollamadas y risas le dieron color a la cuarentena y escribir la tesis. A mis amigos, compañeros, futuros colegas, gracias Mathi, Marcelo, Fabby, Cris, Maiguel, Bica, Seba, Fran, Checho, Picken.

A la fundación SparkTalents, Kirstin, Lith y toda la comunidad FLL que me han acompañado desde el 2009. Al PENTA UC, donde fui estudiante desde el 2008, por permitirme volver como profesora. A TXS Radio y Cooperativa, especialmente a Jorge Lira, por los espacios de divulgación astronómica. A mis estudiantes, escolares y universitarios, me inspiran con sus preguntas y ganas de aprender. A la comunidad que me sigue, confía en mí y me da el espacio para hablar de ciencia.

# Contents

# Table Index

# Figure Index

# Chapter 1

# Introduction

## 1.1. Motivation

In the past decade the technological advancement of astronomical instrumentation has allowed us to observe emission from various sources at unprecedented angular resolution. High resolution imaging has been fundamental for planet-formation studies, it has allowed us to observe and resolve various structures present in the protoplanetary disks of gas and dust around young stars, where we expect planet-formation processes to occur. The study of these structures, from observational and theoretical standpoints, is crucial to be able to constrain the physical or chemical processes that may be producing them. In this work we will focus on the spiral structure of a specific source: Elias 2-27. The presence of two large, symmetric spirals in Elias 2-27 was first detected in Pérez et al. (2016), with the Atacama Large Millimeter/submillimeter Array (ALMA). As will be discussed in the upcoming sections, the possible origins of spirals in protoplanetary disks are well studied: either they are produced by perturbations of an external companion (such as a planet or a binary, e.g. Bae and Zhu (2018b); Rosotti et al. (2020)) or they are induced by effects of the disk itself via gravitational instabilities (e.g. Rice, 2016; Kratter and Lodato, 2016). Previous studies on Elias 2-27 have used observations of a single wavelength (1.3mm) and highly absorbed kinematic data of $^{12}$CO and $^{13}$CO in J = 2-1 transition to try determining the spiral's origin (Pérez et al., 2016; Huang et al., 2018c). This has not been possible, as the system shows different characteristics and additional substructure (a dust gap), making it hard to reconcile the spiral observations with one of the two proposed origins based only on morphological constrains from the dust continuum emission.

This work will analyze new ALMA observations, at comparable angular resolution to the 1.3mm observations of Pérez et al. (2016), but at wavelengths 0.89mm and 3.3mm. The combined analysis of the three emissions will allow us to further discuss on the origin of the spiral structures, by testing for predictions related to dust growth and trapping in the scenarios of companion-disk interactions and gravitational instabilities. Additionally, from the constrains on the spiral morphology at each wavelength, we aim to reproduce the observed dust structure through Smooth-Particle Hydrodynamic simulations of a gravitationally unstable disk, to directly test the theoretical predictions, using observational constrains. We also present

the study of gas observations of $^{13}$CO and C$^{18}$O emission, taken at a higher energy transition (J=3-2) to avoid the previous data's reported absorption. The analysis of the emission from these CO isotopologues will allow us to test for the kinematical features expected in either one of the proposed mechanism responsible for the spiral structure. We additionally study emission from CN molecules, which, if arising from the midplane, is expected to trace shocks (Ilee et al., 2011). Overall, we expect this work to offer a comprehensive observational analysis of Elias 2-27, adequately studying both dust continuum and kinematical tracers and proposing the mechanism responsible for the spiral structure.

If the spirals are caused by companion-disk interactions we are probably observing an extremely short-lived interaction, as the disk is quite massive with respect to the star (disk-to-star mass ratio of 0.1-0.3) and in this case, planet migration rates are very fast (Baruteau et al., 2011). The location of the planet would be very interesting to study (inwards or outside of the spirals) and it would give us further insight into the formation mechanisms and timescales of planets in massive disks. On the other hand, if gravitational instabilities are responsible, then Elias 2-27 would be the first observational detection of this process, offering unprecedented insight and constrains for theoretical models.

This thesis is distributed as follows: The remainder of Chapter 1 offers a theoretical background on planet-formation, observed structure in protoplanetary disks, spiral-forming mechanisms and Elias 2-27. Chapter 2 describes the ALMA observations, calibration procedures and final imaging parameters for the multiwavelength continuum and spectral line data, Chapter 3 describes the analysis and results from the dust continuum data, separating the analysis of spiral arm morphology, contrast variations and spectral index analysis, Chapter 4 presents the study of the CO isotopologue data, from where we reconstruct the emission surface of the gas and constrain Keplerian deviations in the velocity maps, Chapter 5 shows the spectral line emission from the CN molecules and how the found features relate with the dust continuum structures, and Chapter 6 describes smooth-particle hydrodynamic simulations of a gravitationally unstable disk, which where developed in order to accurately compare the possibility of the spiral morphology in the observations originating due to GI mechanisms. Finally Chapter 7 offers an overall discussion on all the results, trying to determine the origin of the spiral structure based on the new observational evidence and model comparison. Chapter 8 concludes and summarizes the findings of this work.

## 1.2. Star and Planet Formation

Stars form from the gravitational collapse of over-dense cores in a molecular cloud, these cores have sizes of about $\sim 10^3$ au (van der Marel, 2015) and are slowly rotating (Terebey et al., 1984). As the core contracts, more distant material, with higher angular momentum falls inwards and rotates faster, due to the conservation of angular momentum. This will quickly form a fast-rotating, flattened disk of material, orbiting around the protostar (Terebey et al., 1984). These disks initially have the same composition as their parent clouds (dust and gas, with dust-to-gas ratios of 100) and receive the name of protoplanetary or planet-forming disks, as they are considered the material reservoirs and birthplace of planetary systems.

Going from a protostellar core to a planetary system, young stellar objects (YSO) are classified into Classes (0, I, II or III) through the analysis of the slope of their spectral energy distribution (SED) between 2-25$\mu$m (Lada, 1987). At these wavelengths the emission comes from the infrared excess, which arises from the circumstellar disk. In the early Class 0-I phases, core material rapidly accretes onto the protostar through the disk, which grows significantly (Williams and Cieza, 2011), these processes last for a period of a few thousand years to a few Myr (Evans et al., 2009) and during this time the disk is deeply embedded in an envelope of material making it invisible for wavelengths $\lesssim$1$\mu$m (Evans et al., 2009). In Class II systems the envelope material is expected to have been removed via molecular outflows and accretion (van der Marel, 2015), therefore only the accretion disk and central star should remain. Measured disk masses at this stage are only a few percent of their central star mass (Williams and Cieza, 2011), systems will be in Class II phase for $\lesssim$10 Myr (Andrews, 2020). Most surveys of near star-forming regions have been conducted on Class II disks (e.g. Cieza et al., 2019; Williams et al., 2019; Andrews et al., 2013; Akeson et al., 2019; Ansdell et al., 2016, 2018; Pascucci et al., 2016; Long et al., 2018a), at this stage we can clearly observe the emission from the disk (Class 0-I emissions have strong emission from the envelope and it is hard to disentangle disk and envelope emissions from each other, Tobin et al. (2015)). Finally, Class III systems have debris disks, these sources have mostly dissipated or accreted their disk material and are gas-poor in comparison to the initial amount of gas they contained (Evans et al., 2009; van der Marel, 2015). The SED is dominated by the stellar photosphere, though some infrared excess from the disk remains (Williams and Cieza, 2011), planets are expected to have formed by this stage. As the central star evolves towards the main sequence and the remaining disk material is dissipated and thus, a planetary system has been formed.

### 1.2.1. Dust Evolution in Protoplanetary Disk

We have roughly described the timeline concerning disk evolution and dissipation, with respect to the central star, but an interesting question is how planets are able to form during the few Myr before this material reservoir is completely dissipated. Protoplanetary disks have a characteristic morphology with a cold, dusty midplane and a warmer, upper layer of gas (Andrews, 2020; Armitage, 2015; Testi et al., 2014). The forces to which gas and dust components are subject differ: gas particles are subject to gravitational, centrifugal and pressure forces, but dust grains do not feel this pressure support and therefore, their motion is determined by gravitational and centrifugal forces (idealized situation, not considering any external perturbations). Pressure support will point outwards from the inner disk, causing gas particles to have a slightly sub-Keplerian motion, this velocity difference with respect to the dust particles (that should follow Keplerian orbits) will cause the deceleration of dust particles, which causes the particle to loose angular momentum, drifting towards the inner disk (Testi et al., 2014). This process is called radial drift and has been largely studied (see Whipple, 1972; Weidenschilling, 1977), the main problem it presents is that the timescales in which particles are expected to accrete on to the central star are much shorter than dust growth timescales (Testi et al., 2014; Andrews, 2015). This implies that large dust particles should not be able to form, unless the radial drift process is somehow slowed. It is important to note that radial drift will mostly affect large dust particles ($\sim$ 1mm), as smaller grains ($\sim$ 0.1$\mu$m) will be well coupled to the gas and follow its motion (Testi et al., 2014). Drift

is most efficient for mm/cm sizes at $\sim$ 10–100 au from the central star (Andrews, 2020). The formation of large particles (eventually planetesimals and planets) is possible and they are not immediately accreted onto the star due to the effects of the radial pressure gradient. This gradient, which is proportional to the drift velocity (Nakagawa et al., 1986), must be locally reversed, specifically if the pressure gradient is zero or positive, there will not be radial drift or the particles will drift to the outwards of the disk. The latter will occur at locations of pressure maxima in the disk structure, dust grains will drift towards these locations and accumulate (dust traps), avoiding radial drift (Pinilla et al., 2012). Dust grains well coupled to the gas will also be transported in the disk through the gas motion, leading to turbulent mixing in radial and vertical directions (see Testi et al., 2014).

To describe the different dust grain sizes, the Stokes number (St) of the particles is used. If the particles are large (St $>$ 1), they will not accurately follow the gas motion, if the dust grains are small enough (St $<$ 1) then they will be well coupled to the gas. The Stokes number can be calculated for a given particle at the disk mid-plane following;

$$St = \frac{a\rho_s}{\Sigma_g}\frac{2}{\pi}, \tag{1.1}$$

where $a$ is the particle radius, $\rho_s$ the mean material density of the dust particle and $\Sigma_g$ the gas surface density. As the Stokes number is linearly dependent on the particle size, which is true for most regions of the disk (excluding the most dense locations), it is easier to refer to a Stokes number rather than particle size, as this value accurately describes the aerodynamical behaviour of a given particle with respect to the gas (Birnstiel et al., 2016).

Dust grains are expected to somehow grow from their initial $\sim 0.1\mu$m sizes (as found in the primordial molecular cloud) to planets, which requires a growth of $>$12 orders of magnitude (Andrews, 2020). Initially, as the small grains collide, they are expected to stick together and produce larger grains (mm sizes) that will decouple from the gas motion and settle in the disk midplane, in a process known as vertical settling (Nakagawa et al., 1986). In the midplane, if the grains are accumulated in pressure maxima, their interactions may excite further growth, depending on material properties (porosity, ice coating, charge), sizes and relative velocities. A collision may be productive (mass transfer, Teiser and Wurm (2009)), neutral (bouncing, Zsom et al. (2010)) or destructive (fragmentation, Krijt et al. (2015)). Through observations we are able to measure and detect the presence of large grains throughout the disk by combining multi-wavelength observations. Grains of size $a$ will emit more efficiently at wavelengths $\lambda \sim a$ (Andrews, 2020), therefore observing in various wavelengths will allow us to roughly trace the individual behaviour of many dust grain populations.

Figure 1.1 shows a schematic of the previously discussed dust grain evolution processes that are present in the disk at different vertical and radial locations. The different emission layers of the disk, and examples of instruments for adequate observations of each layer are shown as discussed in Testi et al. (2014). Scattered light observations are better tracers of the disk surface layers, as they trace $\sim \mu$m-sized grains, which will be suspended in the gas (Andrews, 2020). On the other hand, observing in the millimeter and sub-millimeter range with instruments such as ALMA will allow us to trace larger grains that are settled in the midplane. In order to understand planet formation processes, observations at wavelengths

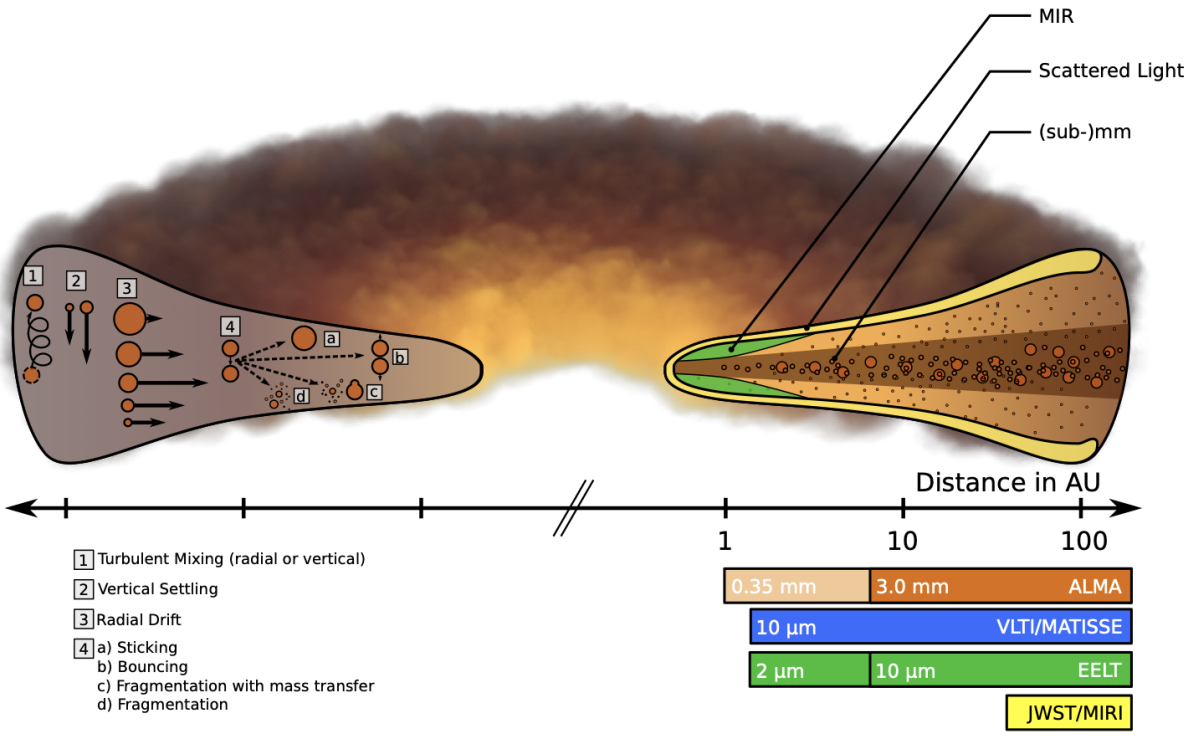


Figure 1.1: Schematic of protoplanetary disk emission layers, grain evolution processes and observational constraints, from Testi et al. 2014.

that trace the cold mid-plane, are critical, since they are sensitive to where the larger solids are located and we may observe substructures where pressure maxima are created and dust concentrated.

### 1.2.2. Gas structure in Protoplanetary Disk

The gas structure of a disk will largely depend on the temperature and activity of the central star (Dutrey et al., 2014). The vertical structure of the gas emitting layer follows hydrostatic equilibrium, supported by gas pressure and flaring at large radial distances. This is determined from the temperature profile of the disk, as the scale height will be proportional to the sound speed ($c_s$), such that $h = c_s/\Omega_k$ where $\Omega_k = \sqrt{GM_*/r^3}$ is the Keplerian angular velocity, as $c_s \propto T^{0.5}$, then $h \propto (Tr^3/M_*)^{0.5}$ (Armitage, 2015; Andrews, 2020). The usual way to obtain the temperature distribution is to forward model the infrared SED, however with sufficient spatial and spectral sensitivity it may also be obtained from observations by directly tracing the emitting layer (e.g. Rosenfeld et al., 2013; Pinte et al., 2018a). Analytic estimations indicate that $T_{disk} \propto r^{-3/4}$ far from the stellar surface ($R_*/r << 1$) which means that $h/r \propto r^{1/8}$, predicting a flared surface at larger radii (Armitage, 2015). The temperature vertical structure is shown in Figure 1.2, the main source of heating comes from the central star, as the disk material is optically thick to the stellar radiation, the disk interior is colder than the upper layers, where gas is heated by energetic stellar radiation. Small grains, well coupled with the gas and suspended in the disk atmosphere absorb starlight

and re-radiate some energy towards the midplane (D'Alessio et al., 1998), this produces an increasing temperature gradient from the midplane to the upper layers (Calvet et al., 1991) and a decreasing radial temperature from the central star to the outer parts of the disk.

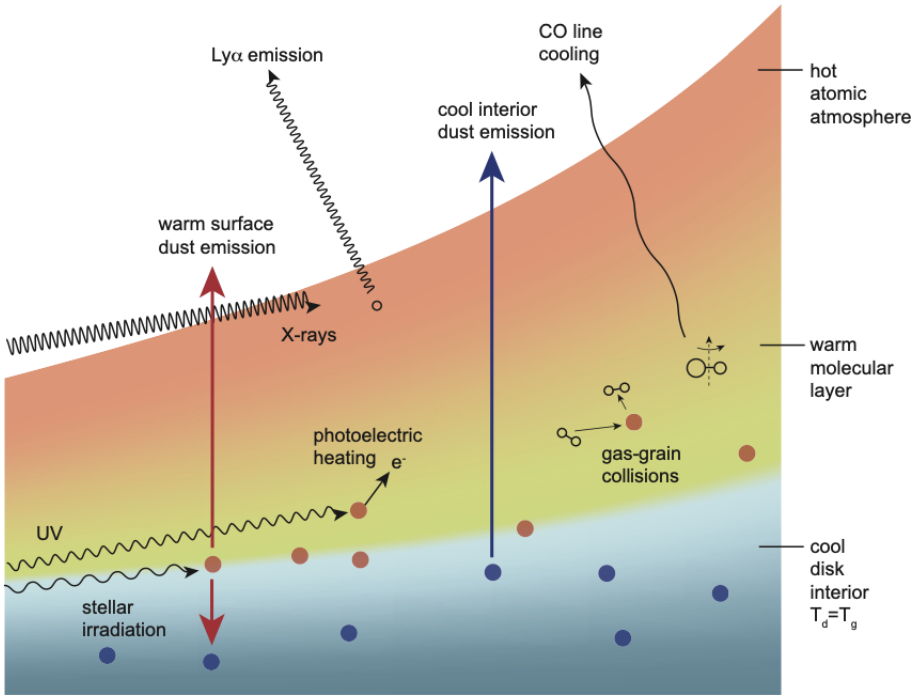


Figure 1.2: Schematic of vertical temperature structure and relevant heating processes from Armitage (2015).

This vertical temperature gradient is relevant for zones where we expect chemical reactions. Although there is a lower density of particles in the disk atmosphere, the high temperatures and exposure to higher energy stellar photons make the upper regions of the disk important for chemistry. There are three distinct chemical zones: (1) the heavily irradiated, hot and dilute atomic atmosphere (upper layer), consisting of simple ions, neutral species, and small dust grains; (2) the warm molecular layer, with many molecules in the gas phase and rapid gas-dust interactions; and (3) the cool disk interior (mid-plane), so cold at large radii (∼20-200 au, Dutrey et al., 2014) that many gaseous molecules are frozen out onto dust grains forming icy mantels around them (see Figure 1.2). We are interested in the processes that will permit molecules initially present in the gaseous component of a protoplanetary disk to remain and be captured by the forming planets (Kama et al., 2016). The evolution of various gas molecules and their presence on dust grains will be largely dependant on the excitement of dust growth in pressure traps throughout the disk (Dutrey et al., 2014; McClure and Dominik, 2019).

## 1.3. Observations of Protoplanetary Disks

### 1.3.1. Structure in dust continuum emission

Disks in the near-by star-forming regions are at a distance of ∼100-200pc from Earth and their dust emission substends ∼1 arcsecond in the sky (Andrews, 2020). This implies the need for sub-arcsecond resolution in millimeter/sub-millimeter observations in order to probe the innermost structure of the disk and resolve features present in the continuum. To date, several surveys have been conducted in order to characterize the dust emission and mass relations of protoplanetary disks from nearby star forming regions; Ophiuchus (Cieza et al., 2019; Williams et al., 2019), Taurus (Andrews et al., 2013; Akeson et al., 2019), Lupus (Ansdell et al., 2016, 2018), Chamaeleon (Pascucci et al., 2016; Long et al., 2018a), IC 348 (Ruíz-Rodríguez et al., 2018) and Upper Scorpius (Barenfeld et al., 2017). In addition, high spatial resolution studies (∼1-5au resolution) at millimeter/sub-millimeter and scattered light have traced a wide range of structures and features in the dust continuum emission (Zhang et al., 2016; Garufi et al., 2018; Long et al., 2018b; Andrews et al., 2018a). From these observation campaigns we have learned that disks have plenty and various substructures, which can be classified, based on their morphology, in distinct groups: rings/cavities (primary bright ring encircling a cavity), rings/gaps (concentric pattern of alternating bright rings and dark gaps), arcs and spirals (see figure 11 in Andrews, 2020).

As previously discussed, the presence of substructure in disks is expected, due to the pressure maxima that must occur throughout the disk to allow the necessary timescales for dust growth to overcome radial drift from rapidly accreting the dust grains onto the central star. Through the study of the morphology and dynamical characteristics of the traced substructures, assuming they are tracing dust density enhancements, we aim to determine their physical or chemical origin. We will briefly describe the proposed origins for rings and gaps, which seem to be the most common substructures in disks (see Andrews et al., 2018a; Huang et al., 2018b; Long et al., 2018b), and non-axisymmetric arcs (e.g., van der Marel et al., 2013). Spiral structures will be analyzed in depth in the upcoming section.

Structures are formed through three main mechanisms; the fluid perturbations caused by the physical conditions of the disk itself, dynamical interactions with companions and condensation fronts (Andrews, 2020). Figure 1.3 shows examples of the mechanisms that may explain cavities, rings and arcs in panel a) and in panel b) the possible origins for subsequent rings and gaps. In the case of cavities, outflows from magnetohydrodynamic (MHD) driven winds predict inner cavities surrounded by a bright emission ring, depending on the mass-loss profile (Takahashi and Muto, 2018). Simulations have shown that MHD turbulence may form various features in the pressure distribution, including axysimmetric distributions (Johansen et al., 2009). When the gas dynamics is modified by concentric concentrations of magnetic flux, gas will be piled up in annuli, pushing away from regions of peak magnetic stress (e.g., Uribe et al., 2011; Simon and Armitage, 2014). The latter will create depletions and enhancements in the radial pressure distribution, which in turn induces annuli where solids will be trapped, leading to the observation of concentric rings and gaps of material. Vortices or arc-like structures may be created through Rossby wave instability (Lovelace et al., 1999; Lyra et al., 2009), baroclinic instabilities (Klahr and Bodenheimer, 2003) or vertical shear instability (Richard et al., 2016). Vortices are sites that attract a vast amount of solids, which makes them possible locations of active planetesimal formation (Klahr and Bodenheimer,

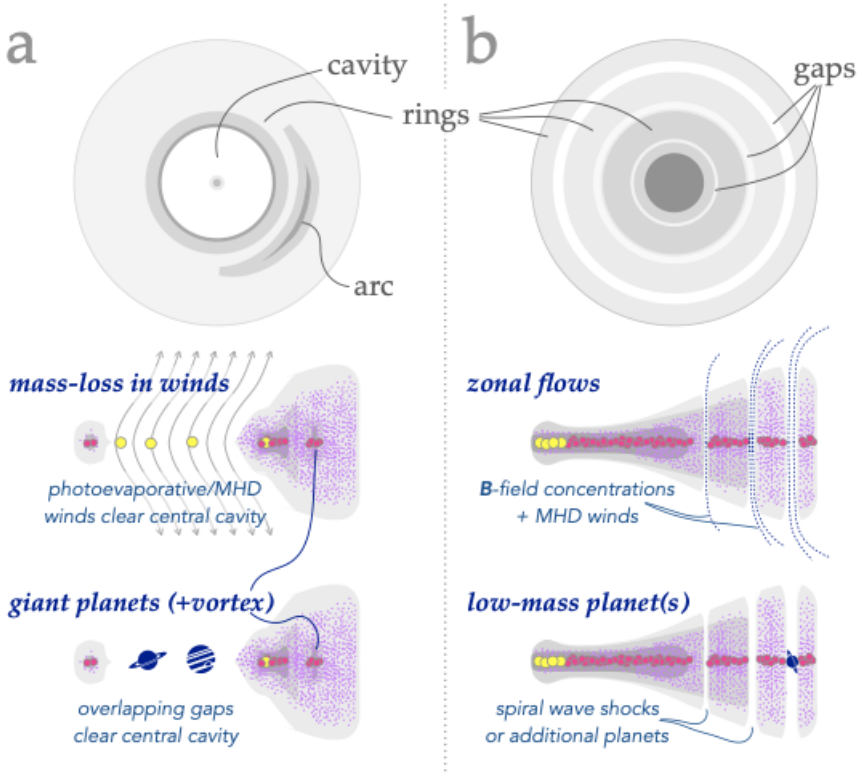


Figure 1.3: Schematic of processes that may create cavity, rings, gaps and arcs traced in the dust continuum emission. Grey scale traces the gas density and solids are marked with exaggerated sizes and colors. Image is taken from Andrews (2020).

2006). Given their large mass, vortices may also produce dust density enhancements in the disk surface (Surville et al., 2016). Companion-disk interactions will also lead to substantial substructures, the strength of the perturbation will depend on the mass of the perturber. Gaps are expected to form as a planet clears the material surrounding its orbital path, additionally, pressure maxima outside of the gap may act as a "particle filter" and trap large solids in the outside (Rice et al., 2006). Multiple giant planets ($>M_J$) with overlapping gaps may create cavities (Zhu et al., 2011) and planets in inclined orbits may create warped structures in the disk (Nealon et al., 2018).

### 1.3.2. Gas observations and Kinematic Tracers

In the gas component of disks, several molecules have been detected, most commonly observations of CO, $HCO^+$ , $H_2CO$, CS, CN, HCN and HNC are obtained (Dutrey et al., 2014). The most abundant molecule in a disk is $H_2$, however, it is not directly observed, for it does not emit efficiently, due to lack of a permanent dipole moment (Dutrey et al., 2014; Andrews, 2020). To trace the bulk of gas, observations rely on spectral line emission from other molecules, however, estimates of gas masses from these measurements and interpretation of spectral lines in general have large uncertainties, due to the intrinsic uncertainties on

molecular abundances ($X_j$) and high optical depths (Andrews, 2020).

Besides studying the presence of various molecules and chemical interactions, if we have an adequate spectral resolution, valuable dynamical information may be obtained from gas observations, by reconstructing the three-dimensional disk velocity field and analyzing any deviations from the expected Keplerian motion of the gas particles. The dominant factor in the kinematic structure of a disk is orbital motion, however, it is also affected by contributions from other mechanisms of the disk such as: magnetic fields (Turner et al., 2014), viscous transport (Lynden-Bell and Pringle, 1974), pressure support (Weidenschilling, 1977), winds (Ercolano and Pascucci, 2017) and gravitational instabilities, if the disk mass is sufficiently large (Bertin and Lodato, 1999).

External perturbations will also affect the orbital motion of the gas, for example, the presence of planets or companions leaves distinct traces in the kinematics, these perturbations may be constrained by the amplitude of the gas deviations from the expected Keplerian motion of an unperturbed disk. The current state-of-the-art methods vary from: tracing vertical pressure gradients (Teague et al., 2018a), observing deviations from expected isovelocity curves in the channel maps ("kinks") (Perez et al., 2015; Pinte et al., 2018b, 2019, 2020) and using the mean velocity maps maps to model the velocity structure of the disk and detection of doppler flips in the residuals (Pérez et al., 2020, 2018b). Analyzing the disk kinematics complements the analysis of the observed dust structures and allows us to understand and connect the various ongoing processes, whether the disk is influenced solely by its own dynamical perturbations or if there are disk-companion interactions.

## 1.4. Spiral Structures in Protoplanetary Disks

Though much less common than axisymmetric structures such as rings or gaps (e.g. ALMA Partnership et al., 2015; Andrews et al., 2018a; Huang et al., 2018b; Long et al., 2018a), spiral structures have been observed in different components of several protoplanetary disks, mainly through scattered light observations (e.g. Muto et al., 2012; Grady et al., 2013; Akiyama et al., 2016; Benisty et al., 2017). Spirals in spectral line emission have also been found in some sources (Tang et al., 2012; Christiaens et al., 2014; Teague et al., 2019) and most recently, with ALMA, a few disks with spirals waves arising from the midplane have been detected (Pérez et al., 2016; Huang et al., 2018c; Kurtovic et al., 2018). Figure 1.4 shows different systems with spirals traced in dust continuum with millimeter (top row) and scattered light observations (bottom row). It is important to note that in the case of disks with spirals observed in scattered light, most do not show simultaneous spirals in millimeter emission. Indeed, some of these sources show non-axisymmetric arc-like structures in the millimeter emission from the midplane (Dong et al., 2018; Cazzoletti et al., 2018a). The interesting question is how we relate the presence of a spiral perturbation, detected by any given tracer, to a dynamical process occurring in the disk.

In the case of spiral structures traced to the midplane, their origin may be linked to the presence of a companion: stellar, fly-by or planetary (Forgan et al., 2018b; Cuello et al., 2019; Bae and Zhu, 2018a; Dong et al., 2018), or to the disk itself, as spirals may be excited in

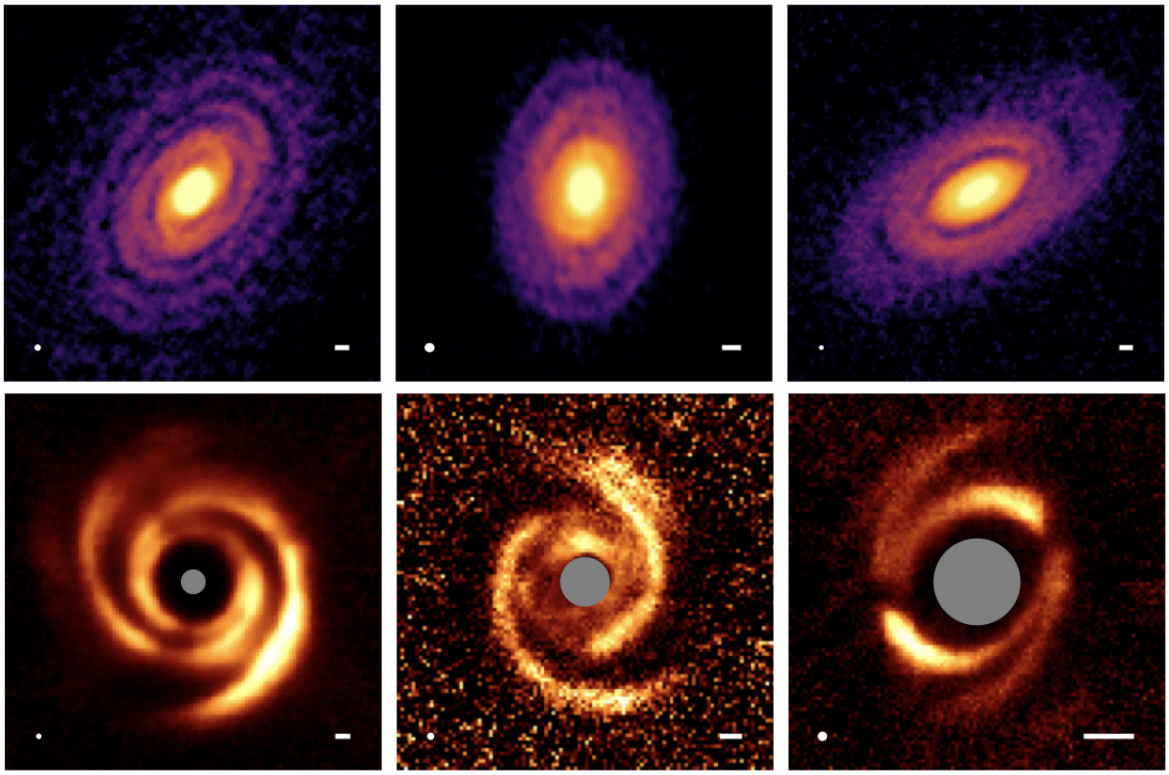

Figure 1.4: Gallery of different spirals traced at millimeter wavelenghts (Top row) and in scattered light (Bottom row) image taken from Andrews (2020). Systems from left to right correspond to: Top, IM Lup, WaOph 6, Elias 27 (all from Huang et al. (2018c)), Bottom, SAO 206462 (Stolker et al., 2017), MWC 758 (Benisty et al., 2015), and HD 100453 (Benisty et al., 2017)

large disks were the disk-to-star mass ratio is larger than ∼0.1 and therefore the system is gravitationally unstable (Gammie, 2001; Cossins et al., 2009; Kratter and Lodato, 2016; Rice, 2016; Hall et al., 2016; Zhang and Zhu, 2020; Hall et al., 2019). To date not many observations of spirals in dust continuum emission have a clear origin, except for those in multiple systems where the presence of spirals has been linked to the tidal interaction between the disk and the stellar companion (Kurtovic et al., 2018; Rosotti et al., 2020). On the other hand, there are disks were spirals have been reported at millimeter wavelengths (Elias 2-27, IM Lup, WaOph 6, MWC 758) and where no companion to which the spiral origin may be linked to, has been detected yet (Pérez et al., 2016; Huang et al., 2018c; Dong et al., 2018, 2015a,b). If no companion is detected and the disk is massive compared to the host star mass, the gravitational instability (GI) scenario arises as a possible explanation for the origin of the observed spirals. Studying such a disk is interesting, population synthesis models show that GI primarily ends up forming brown dwarf mass objects (Forgan et al., 2018a), which is backed up by hydrodynamical simulations (Hall et al., 2017). It seems that giant planet formation through GI is rare (Rice et al., 2015), but it may still be the dominant formation mechanism for rare objects such as HR 8799 (Vigan et al., 2017, 2020). Potentially studying these mechanisms, through the observation of a gravitationally unstable disk, would help towards the further development of theories in the field

### 1.4.1. Spirals arising from Gravitational Instability

Self-gravity in a protoplanetary disk, refers to the effect of the gravitational field of the disk itself, rather than the center star, on the evolution of the system. The instability manifests itself by the generation of spiral arms, small scale density fluctuations, and fragmentation of the disk itself (Kratter and Lodato, 2016). The standard reference for quantifying the degree to which a disk is self-gravitating is the Toomre $Q$ parameter (Toomre, 1964), defined as:

$$Q = \frac{c_s \kappa}{\pi G \Sigma} \tag{1.2}$$

here $c_s$ is the sound speed of the gas, $\kappa$ the epicyclic frequency ($\Omega_k$ in a Keplerian disk), $\Sigma$ is the disk surface density and $G$ the universal gravitational constant. As $Q$ approaches 1, self-gravity becomes increasingly important, higher values of $Q$ will be more stable than lower values. If we want to determine the value of $Q$ from observational constrains of a protoplanetary disk, then we may use the following relation;

$$Q = f \frac{M_*}{M_d} \frac{H}{r} \tag{1.3}$$

where $M_*$ is the central star mass, $M_d$ is the disk mass, $H/r$ is the disk's aspect ratio (height at a certain radius $r$) and $f$ is a prefactor that considers numerical factors of orden unity (Kratter and Lodato, 2016). From here we can see that lower values of $H/r$ (thinner disks, therefore colder disks, see section 1.2.2) will be more prone to self-gravity. Using standard assumptions on disk temperatures, sizes, and scale height distribution it can be shown that self-gravity is expected to be important for disk-to-star mass ratios greater than $\sim$0.1 (Kratter and Lodato, 2016; Lodato, 2007).

From current observational constrains on disk and stellar masses, most systems do not seem to have large enough disk-to-star mass ratios to excite GI, as most young stars only harbor disks with a few percentage of their stellar mass or less. Large disk masses, where GI could be relevant, are expected in the early stages of core collapse (Class 0-I), but in these epochs the disk emission is very optically thick, even at mm wavelengths, therefore, it is difficult to obtain mass estimates and/or trace structures in the disk. Even then, masses in Class 0-I sources range from $\sim$0.02-0.1$M_\odot$ with a median 0.04$M_\odot$ (Williams and Cieza, 2011). However, these mass estimates should probably be considered lower bounds, as optically thick emission will prevent measuring the absolute mass value, therefore, disk masses could be much higher than measured. GI present at the earlier stages of disk formation is one of the main proposed mechanisms for planet formation in early epochs, via fragmentation of the GI spirals (Boss, 1997; Nayakshin, 2010).

What is certain is that, if a disk is gravitationally unstable, spiral features will be excited. The excitation of spiral arms is closely related to the temperature of the disk, and they are considered a way of self-regulation of the disk temperature (recall that GI is excited in cooler disks). GI spirals will cause shocks that will heat the disk surface, if sufficient heat is retained, the whole disk will heat back up, quenching the instability, which in turn decreases

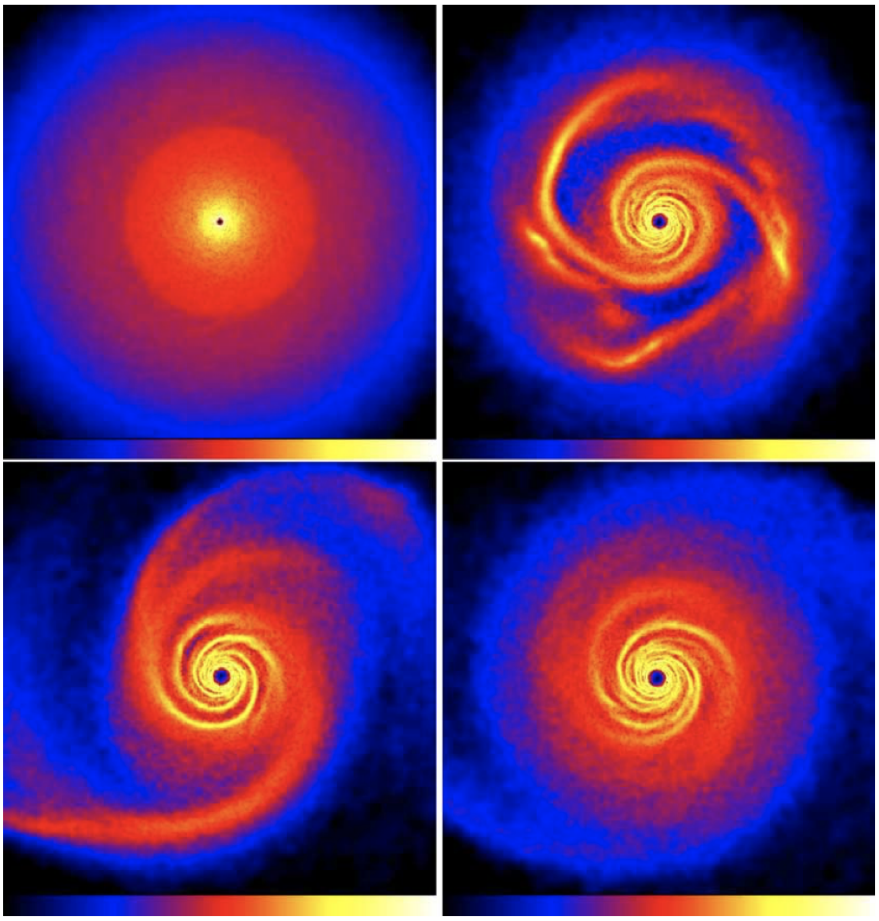

Figure 1.5: Time evolution of the surface density of a self-gravitating disk with $M_{disk} = 0.5 M_{star}$. Evolution times are: $t = 0$ (upper left), $t = 1.9 t_0$ (upper right), $t = 2.5 t_0$ (lower left) and $t = 3 t_0$ (lower right). $t_0$ indicates the rotation period of the outer disk, such that $t_0 = 2\pi/\Omega_{out}$. Panel from Lodato and Rice (2005).

the heating rate, allowing the disk to cool back towards instability. This cyclic condition allows for disks with $Q$ values higher than unity to possibly be in a marginally unstable state (Kratter and Lodato, 2016; Lodato, 2007).

Spiral arms formed via GI mechanisms are expected to have distinct dynamical and observational characteristics. These spirals will co-rotate with the disk structure, therefore dust trapping is expected to occur along the spiral structure and grain growth processes could be excited (Dong et al., 2015a; Rice et al., 2004; Dipierro et al., 2015). Additionally, the number of spirals will depend on the disk-to-star mass ratio ($q$) and will roughly follow $\sim 1/q$ (Dong et al., 2015a; Kratter and Lodato, 2016; Lodato, 2007). We expect spirals generated by GI to have similar contrast between them and be symmetric when comparing their pitch angle values, which should be constant at all radii (Forgan et al., 2018b; Bae and Zhu, 2018b). Kinematic signatures will also be distinct for GI spirals and recent work by Hall et al. (2020), characterizes the presence of a "GI-wiggle" that, contrary to companion-disk interactions, will not be spatially localized, it will be a large scale perturbation across several channel maps co-located with the spirals.

### 1.4.2. Spirals arising from Planet-Disk Interaction

Planet-disk interactions cause density waves in the form of spiral arms, due to the gravitational influence of planets and their perturbations on the disks (Goldreich and Tremaine, 1979). There is always at least one spiral arm excited (Ogilvie and Lubow, 2002), that originates from the planet, however, two spiral arms may be excited, if planets are massive enough and orbit at large distances from the star (Zhu et al., 2015; Dong et al., 2015b; Bae and Zhu, 2018a). These secondary spirals have lower contrast than the primary spiral arm and studying the differences in pitch angle between both spirals, or the spatial separation between them it is possible to characterize the planetary companion (Bae and Zhu, 2018b).

Overall, the morphology of the spirals depends largely on the planet mass and disk properties and is also affected by the temperature and scale height (Bae and Zhu, 2018b; Juhász et al., 2015; Juhász and Rosotti, 2018). This implies that studying spiral features at multiple wavelengths (near-infrared and sub-millimetre), which trace different height and temperature layers, can help us constrain a planetary origin and determine the planet's position and mass (Juhász and Rosotti, 2018; Rosotti et al., 2020). Figure 1.6 shows the difference in the spiral number and morphology when varying the companion mass and scale height. Additionally, if adequate angular resolution is available, planetary spirals traced in the midplane are expected to have a varying pitch angle, as a function of radial distance (Bae and Zhu, 2018b; Forgan et al., 2018b).

Another characteristic of planet-disk interaction spirals is that they will co-rotate with the planet (at the Keplerian speed of the planet), therefore they will move with respect to the background gas, at a given radial location (Juhász et al., 2015). The velocity difference will prevent dust from accumulating at the spiral location, as the dust accumulation timescales are much longer than local orbital periods (Birnstiel et al., 2013), therefore dust-growth processes are not expected in these spirals. The presence of large dust grains will alter the dust opacity of the emission ($\kappa_\nu$), which is related to the observed frequency ($\nu$) through the power-law spectral index of the dust opacity, $\beta$, with $\kappa_\nu \propto \nu^\beta$. As grains reach millimeter or larger sizes, $\beta$ becomes smaller, this can be related to the intensity measurements if the emission is in the Rayleigh-Jeans regime ($h\nu << kT$) and so, $I_\nu \propto \nu^\alpha$, with $\beta = \alpha - 2$. Therefore, one can observationally test for the presence or lack of large grains at the spiral location using multi-wavelength observations. If the spirals are formed through planet-disk interactions, then no spectral index variations should be observed at the spiral arm location.

Spiral arms excited by planetary companions may create gaps through shock dissipation (Bae et al., 2017), however both structures will not always be observed simultaneously, as gap-opening depends on the viscosity of the disk and the timescales of spiral and gap formation are very different. Spiral arms appear and reach a quasi-steady state over a few planetary orbits, however rings and gaps may require up to 100 orbital times (Bae et al., 2017; Bae and Zhu, 2018b). Additionally, if the planet is located at a large orbital distance from the star, as in the cases shown in Figure 1.6, we will not see a gap at the planet location, for it will be further out than the dust component of the disk. In the latter case, we may detect the location of the planet through its kinematic signature.

If spirals are caused by a companion, we should detect localized kinematic signatures in

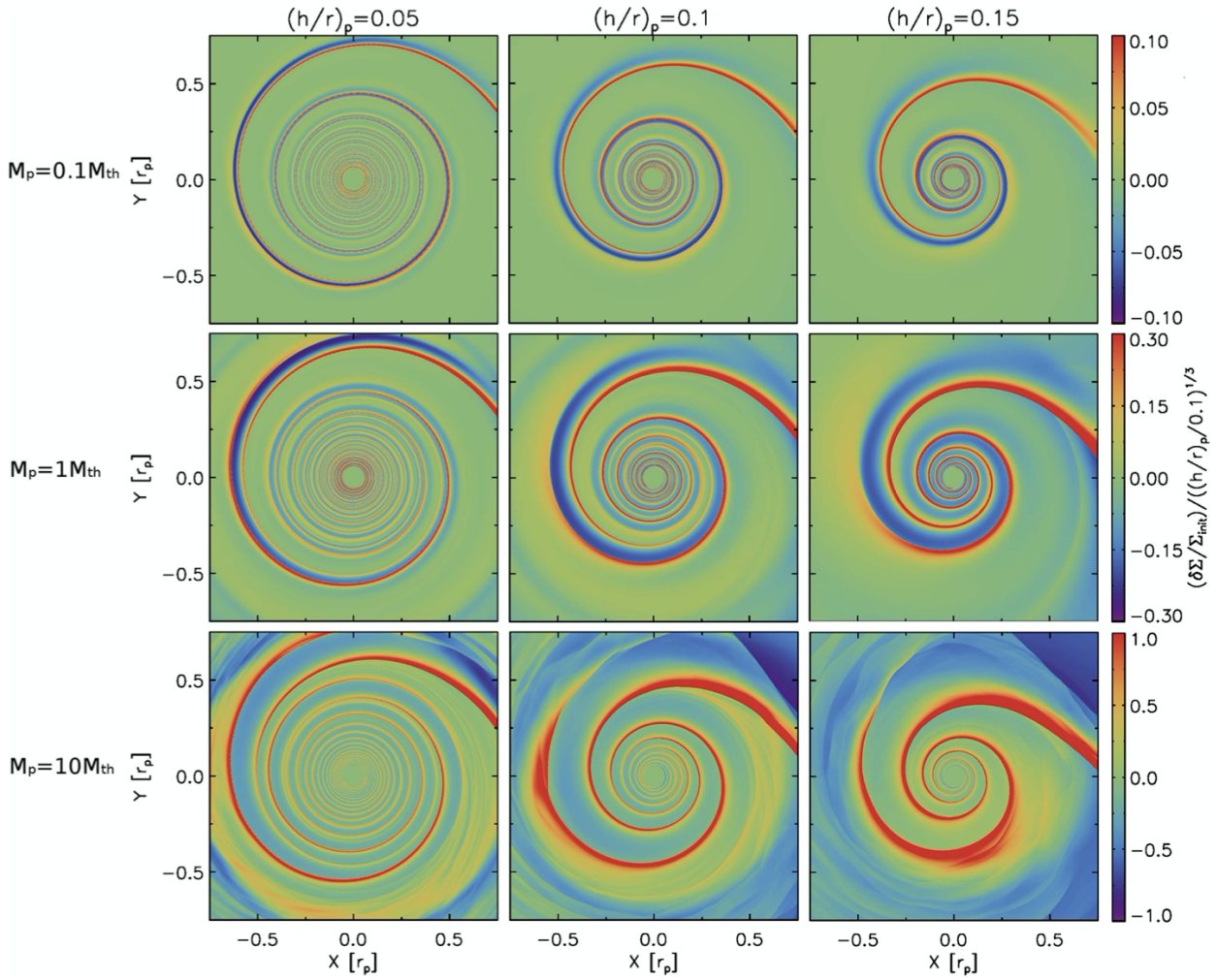


Figure 1.6: Surface density perturbations for various disk aspect ratio values $(h/r)_p$ and planet masses $M_p$. Planet is located at (X, Y) = (1, 0), for further information refer to Bae and Zhu (2018b).

spectral line observations, especially if the perturber has a high mass ($>1M_J$), which is expected if more than one spiral wave is excited (Bae and Zhu, 2018b). In systems where spirals are believed to be caused by large planets or binary companions, spiral arcs of gas have been detected, connecting the companion with the main disk emission (Kurtovic et al., 2018; Juhász and Rosotti, 2018; Cuello et al., 2020). If the perturber is planetary, with masses in the order of at least $\sim 1M_J$, it should produce measurable, local kinematic perturbations, deviating the gas velocity from expected Keplerian motion by $\sim 15\,\%$ (Perez et al., 2015; Pinte et al., 2018b). The latter can be traced and detected through channel map analysis, with adecuate spectral and angular resolution (see Pinte et al., 2019, 2018b). If the perturber is $<1M_J$ it will leave more subtle kinematic perturbations, if these perturbations cause deviations of at least $\sim 2\,\%$ from Keplerian motion, they may be measured testing for local pressure gradients (Teague et al., 2018b,a).

## 1.5. The young star Elias 2-27

As mentioned in the initial Motivation (section 1.1), this thesis focuses on the analysis of the spiral structure observed in Elias 2-27, through observations of dust continuum emission at multiple wavelengths (0.89mm, 1.3mm and 3.3mm) and kinematic tracers using CO isotopologues and CN molecules. Elias 2-27 is a young 0.8 Myr ± 3yr M0 star (Andrews et al., 2018a) located at a distance of $115.88^{+19}_{-10}$ pc (Gaia Collaboration et al., 2018) in the $\rho$ Oph star-forming region (Luhman and Rieke, 1999). It harbors an unusually large protoplanetary disk, the disk-to-star mass ratio of Elias 2-27 is reported to be $\sim 0.3$ (Andrews et al., 2009; Pérez et al., 2016) . After the initial detection of two large-scale spiral arms with medium-resolution ALMA observations (Pérez et al., 2016) it became one of the "Disk Substructures at High Angular Resolution Project" (DSHARP) targets, to further analyze the dust emission at high resolution (Andrews et al., 2018a; Huang et al., 2018c). Its distinctive morphology consists of two grand-scale quasi-symmetric spiral arms and a distinct, 14 au wide gap, located at 69 au from the star (Huang et al., 2018b). Due to its characteristic structure, the system has been subject to several theoretical studies, trying to determine the origin of the observed spirals. There is general agreement about the likelihood of the spiral arms originating due to GI given their symmetric morphology, but an external massive companion may also reproduce a similar structure (Hall et al., 2018; Forgan et al., 2018b; Meru et al., 2017; Bae and Zhu, 2018b). Additionally, even though GI seems to explain the spiral morphology, it does not explain the dust gap, which could be carved by a companion of $\sim$0.1 $M_J$ as constrained in hydrodynamical simulations by Zhang et al. (2018). Localized deviations from Keplerian motions at the location of this dust gap have been recently found, strengthening the hypothesis of a planetary-mass companion (Pinte et al., 2020). These latter studies can explain the presence of the gap, but not of the large-scale spirals, as it has been shown that a lower mass inner companion, such as the one proposed to open the gap, would not be able to excite the observed large-scale spiral arms (Meru et al., 2017).

Overall, Elias 2-27 seems to be a strong candidate to be a protoplanetary disk undergoing gravitational instabilities. However, there are many observational tests to be done in order to determine if this is in fact the origin of the observed spirals. We have previously discussed the main physical and morphological differences between GI and planet-disk originated spirals. If GI is the mechanism responsible for the spirals, we expect to measure dust growth signatures along the spiral structure (Dipierro et al., 2015) and constrain symmetric spiral morphology (Forgan et al., 2018b). If the spirals come from planet-disk interactions, we should measure asymmetric spirals in shape and contrast (Bae and Zhu, 2018b; Forgan et al., 2018b) and no signatures of grain growth (Juhász et al., 2015). To measure the lack or presence of these characteristics, we present the analysis of multi-wavelength dust continuum observations, with multiple wavelengths we will be able to constrain the presence of grain growth and any changes in the spiral morphology at different frequencies. These results are discussed in chapter 3.

To better constrain the dynamical processes in Elias 2-27, we also conduct a kinematical analysis, with different gas tracers (CO isotopologues and CN). It has been discussed that both planetary companions and GI perturbations will leave distinct kinematical signatures in the velocity maps that may be differentiated by their amplitude and spatial localization.

Previously published gas observations of Elias 2-27 were of $^{12}$CO and $^{13}$CO in J: 2-1 transition and showed heavy absorption, as the star is quite embedded in its cloud (Andrews et al., 2009; Pérez et al., 2016; Andrews et al., 2018a). In this study we present $^{13}$CO and C$^{18}$O observations in J: 3-2 transition, this higher energy transition allows us to avoid some of the cloud contamination while also probing closer to the midplane than previous work, by tracing a less abundant CO isotopologue (C$^{18}$O). We will combine our kinematical analysis with the study of multiwavelength dust continuum observations, which will allow us to propose an origin of the observed structure.

# Chapter 2

# Observations

## 2.1. Observing with ALMA

In this work we use observations taken with the Atacama Large Millimeter/submillimeter Array (ALMA), composed of 66 high-precision antennas distributed between the 12-m array (fifty 12-meter wide antennas), Atacama Compact Array (twelve 7-m antennas) and the Total Power (TP) Array (four 12-m antennas). ALMA captures emission in the millimeter/submillimeter range, between 84GHz-950GHz (soon to be extended up to 35 GHz when Bands 1 and 2 are deployed), at high angular resolution (22mas at 950GHz). Antennas are arranged in specific configurations, where the separation between a pair of antennas (baseline) goes between 0.16 - 16.2 km[1]. The baseline separation between antenna pairs, together with the observed frequency, will define the final spatial resolution of the observations (larger baselines and higher frequencies will offer better spatial resolution).

ALMA combines the measurements of each pair of antennas through a technique called interferometry. An interferometer samples the power spectrum of the sky brightness distribution, each antenna pair will obtain a single data point, which will be located in a specific position on the uv-plane. The uv-plane is a cartesian coordinate system, such that it is always perpendicular to the observed source's direction and will hold the information on the relative position between each antenna pair. Each baseline vector (position vector from antenna 1 to antenna 2), will be deprojected in this uv-plane, in units of wavelength (Thompson et al., 2017). Obtaining a good image of a source requires adequate sampling (coverage) of the uv-plane, which may be achieved by having multiple baselines and/or integrating over sufficiently long periods of time (Earth's rotation will rotate the baseline vectors and better uv-coverage will be achieved). ALMA's multiple configurations are used to improve the uv-coverage, combining them allows to have antennas closer together (short baselines) and further apart (long baselines). Short baselines will sample large-scale angular structure, while

[1] For detailed and further information on ALMA see: https://almascience.eso.org/documents-and-tools/latest/documents-and-tools/cycle8/alma-science-primer, https://almascience.nrao.edu/documents-and-tools/cycle8/alma-technical-handbook and https://almascience.nrao.edu/documents-and-tools/cycle8/alma-proposers-guide

long baselines sample small-scale angular structure. ALMA correlators will process the data from each antenna-pair and can handle up to 64 antennas, therefore, up to 1225 antenna pairs may offer a data point at each integration (typically a few seconds).

Each baseline will measure the brightness distribution of the sky through a complex visibility defined as

$$V_v(\mathbf{b}) = Ae^{-i\phi} = \iint_{\Omega} I_\nu(s) e^{-2\pi i \nu \mathbf{b}\cdot\mathbf{s}/c} d\Omega \tag{2.1}$$

The visibility measurement will be defined through the phase ($\phi$) and amplitude ($A$), which relate to the location and flux of the source, respectively. The real emission of the source, with a position defined by unit direction vector $\mathbf{s}$, at a frequency $\nu$ ($I_\nu(s)$) will be related to the measured visibilities of baseline $\mathbf{b}$ ($V_v(\mathbf{b})$) through a Fourier transform (the complex visibility is the 2D Fourier transform of the sky brightness distribution). While the visibilities may be analyzed directly in the complex plane to infer the source's properties, we will be mainly interested in producing images of the source emission. However, before studying the source emission, it is necessary to account for possible sources of corruption to the visibilities. These can be separated into antenna-based, amplitude and phase-based, dispersive and non-dispersive. Several corrections are needed to account for all of them. Antenna-based corrections aim towards correcting any issues of an independent antenna within the antenna array. Amplitude and phase corrections will be neccessary to account for changes in the atmosphere that may affect the data, these corrections depend on the observation frequency and observing time-scales. Dispersive and non-dispersive errors will happen when there are delay variations along the antenna signal path. These calibration errors produce antenna-based phase changes, if the phase changes vary linearly with frequency they will be non-dispersive, any other phase changes will be dispersive. To accurately account for most of the needed calibrations, ALMA processes the data from each observation through a standard ALMA data reduction and performs quality assurance tests so the required signal-to-noise and resolution are reached. Further calibration can be done to reach better signal-to-noise and image quality, through a process of self-calibration, that will correct remaining phase or amplitude variations, based on a selected reference antenna. Self-calibration is an iterative process which may be applied when there is sufficient signal-to-noise in the data and the baseline number is much larger than the antennas, as the corrections to the visibilities are obtained by comparing the data to a model generated by the same data. Each iteration is determined by a time interval, over which the data is averaged and gain solutions interpolated, in each consecutive iteration the time interval is decreased until signal-to-noise improvements aren't sufficient (in most cases we will expect a minimum of 5 % signal-to-noise improvement should be reached in each iteration).

Finally, to obtain the image from the calibrated visibilities, deconvolution algorithms are applied, the two most common are CLEAN (Högbom, 1974) and maximum entropy (Gull and Daniell, 1978). We will use the CLEAN algorithm, as implemented in the Common Astronomy Software Applications (CASA, McMullin et al. (2007)), to obtain the image of the estimate of the true sky brightness $I_\nu$ of the observation target. As a first step, the synthesized beam (analogous of the point-spread function (PSF) in an optical telescope, also called

"dirty beam") is obtained through the Fourier transform of the uv-plane coverage, previously weighted by a determined weighting function $W(u, v)$. Through an iterative proccess, the deconvolution algorithm will create an emission model for the source, convolve it with the PSF and compare it to the "dirty beam" (which corresponds to the true emission, convolved with the PSF). Ultimately the algorithm obtains a clean image for analysis, convolving the model with an elliptical Gaussian fit to the main lobe of the PSF. We can change the angular resolution and sensitivity of the final image by changing the weighting function $W(u, v)$ and modifying the PSF. There are two main forms to define the weighting scheme: natural weighting, where $W(u, v) = 1/\sigma^2(u, v)$, here $\sigma^2(u, v)$ is the noise variance of the (u,v) sample and uniform weighting, where $W(u, v)$ is inversely proportional to the local density of (u,v) points. Natural weighting will deliver maximum sensitivity, but a larger synthesized beam, as there is typically a higher density of short-baseline antennas. Uniform weighting will give higher considerations to baselines of under-sampled regions, generally corresponding to longer baselines and in this way it increases angular resolution at the expense of sensitivity. We use the tclean[2] task from CASA, which allows us to set the weighting scheme through the robust parameter (Briggs weighting). Robust values go between -2 and 2, robust=-2 is equivalent to uniform weighting and natural weighting corresponds to robust=2, intermediate values are allowed to bridge the extremes between both weighting schemes. Additionally, we can apply "uv-tappering" to multiply the weights of the visibilities by a Gaussian, giving us more control over the geometry of the PSF and "uv-range" to consider only a determined range of (u,v) points for an image, this is used for filtering large-scale emission. Another important aspect in the imaging is how the deconvolution algorithm will construct the source emission model, which is generally done through a collection of point sources. We use multi-scale tclean, which allows us the model to be constructed from extended sources of various angular sizes, instead of from point sources.

## 2.2. Elias 2-27 Observations

We present multi-wavelength (Band 3, 6 and 7) dust continuum and gas ALMA data of Elias 2-27 (Right Ascension (J2000) = 16h 26m 45.024s, Declination (J2000) = –24d 23m 08.250s ). In the case of the Band 6 (1.3mm) observations, the imaged data corresponds to the one presented in Pérez et al. (2016). Detailed information regarding the calibration of this dataset may be found in the original publication. For the Band 7 (0.89mm) and Band 3 (3.3mm) observations, the dust continuum data was first calibrated through the ALMA pipeline and afterwards, phase and amplitude self-calibration was applied. Additionally, following the calibration procedure described in Andrews et al. (2018a), we applied astrometric and flux scale alignment, to correct for spatial offsets between the center of emission of different observations and relative flux scale differences. In both bands we have short (15m-313.7m in Band 7, 15.1m-2.5km in Band 3) and long (15.1m-1.4km in Band 7, 21m-3.6km in Band 3) baseline observations, in order to account for all of the emission from different spatial scales of the disk. Spatial offsets are corrected by locating the center of emission through a Gaussian fit on the image plane of each observation and adjusting phase and pointing centers with the CASA tasks FIXVIS and FIXPLANETS respectively. Flux calibration error of the data after

[2] Documentation available in https://casa.nrao.edu/docs/taskref/tclean-task.html

reduction through the ALMA pipeline is expected to be ∼10 %, however self-calibration (self-cal) results (regarding signal-to-noise) significantly improve if the relative flux scales between observations are consistent within ∼5 % (Andrews et al., 2018a). To adjust these amplitude scale differences we compare the deprojected, azimuthally averaged, visibility profiles and scale using the short-baseline data as reference frame using the GAINCAL task. For Band 7 data we apply the spatial offset corrections and amplitude scaling before any self calibration as relative flux scales vary $5-10$ % between observation sets. In the Band 3 data set we have a higher flux scale difference from the initial datasets (∼20 %), probably due to atmospheric conditions as we can visually see that the image quality is not the best. Therefore, in Band 3 we conduct self-cal of the short-baseline observation and afterwards, with a flux scale difference of ∼3 %, we do the spatial and amplitude scale corrections.

### 2.2.1. Imaging dust continuum emission

After flux-scale alignment, self-calibration was first conducted on the dust continuum emission short baseline data and then, the self-calibrated measurement set was combined with the long-baseline data and was then self-calibrated together. For the time intervals, in both phase and amplitude self-calibrations, the initial round was always done with the longest available total observation period, and afterwards, each following time interval was half of the previous interval. The longest and shortest intervals used, in seconds (s), were 1500s and 46s for the phase calibration of the joint 0.89mm data, and 2860s and 178s for the phase calibration of the joint 3.3mm data. For the calibration of the short baseline data the time intervals of phase calibration were between 1080s and 270s for the 0.89mm data, and 304s and 9.5s for the 3.3mm data. In the case of the amplitude self-cal time intervals, in Band 7 only one round was required in both short baseline and joint data, so the solutions were obtained from the longest time interval. In Band 3 the short baseline data had one round of amplitude calibration and the joint data set had two rounds. Self-calibration rounds were applied until signal-to-noise ratio (SNR) improvement was less than 5 % in the case of Band 7 data and until there was no SNR improvement in the case of Band 3. For the short base-line data at 0.89mm, we conducted 3 rounds of phase calibration and 1 round of amplitude calibration. The combined dataset at 0.89mm had 7 rounds of phase calibration and 1 round of amplitude calibration, overall the peak SNR in the joint dataset improved 300 %. The short base-line data at 3.3mm had 6 rounds of phase calibration and 1 round of amplitude calibration, the joint data set had 2 rounds of phase calibration and 1 round of amplitude calibration. In the joint dataset, the SNR improvement was 6 %.

For the final imaging we used multi-scale TCLEAN for all the images, using a $1\sigma$ stopping threshold (where $\sigma$ is the image rms) for the Bands 3 and 6 data, and a $2\sigma$ stopping threshold in Band 7. Robust weighting values were 1.0 in the case of Band 6, and 0.5 for Bands 3 and 7. We also set the GAIN value to 0.05 and CYCLEFACTOR parameter in TCLEAN to 2.0, to have a more detailed cleaning, by subtracting a smaller fraction of the source flux from the residual image and triggering a major cycle sooner. All images have comparable beam sizes: 0.22" x 0.17" beam (26 au x 20 au) at 0.89mm, 0.26" x 0.22" beam (30 au x 26 au) at 1.3mm, and 0.26" x 0.20" (30 au x 23 au) beam at 3.3mm. At each wavelength the image RMS is approximately 93$\mu$Jy/beam , 86$\mu$Jy/beam and 10$\mu$Jy/beam, for the 0.89mm, 1.3mm and

Table 2.1: Dust Imaging Summary

| Band | Frequency [GHz] | robust | Synthesized Beam arcsec["] | Peak $I_\nu$ [mJy beam$^{-1}$] | RMS noise [mJy beam$^{-1}$] |
|---|---|---|---|---|---|
| 3 | 90.500 | 0.5 | 0.26 x 0.20 | 5.7 | 0.0098 |
| 6 | 231.200 | 1.0 | 0.26 x 0.22 | 31.4 | 0.0862 |
| 7 | 336.151 | 0.5 | 0.22 x 0.17 | 46.9 | 0.0938 |

3.3mm maps, respectively. The final images for each wavelength and analysis are shown in Chapter 3.

### 2.2.2. Imaging molecular gas emission

The observations of $C^{18}O$ and $^{13}CO$ data, obtained simultaneous to the dust continuum emission in Band 7 (0.89mm), were done in the $J = 3-2$ transition to avoid the heavy cloud contamination reported in previous studies using the lower $J = 2-1$ transition (Pérez et al., 2016; Huang et al., 2018c). $C^{18}O$ is observed at 329.330 GHz, with a spectral resolution of 35.278 kHz and $^{13}CO$ at 330.588 GHz, with a spectral resolution of 0.121 MHz. After applying the same self-calibration solutions as to the dust continuum of Band 7, the emission was first imaged using natural weighting (robust parameter of 2.0) and not applying any uvtapering or uv-range filtering, in order to be sensitive to large-scale emission with a 0.29" x 0.22" ($\sim$ 34x25 au) for $^{13}CO$ and 0.30" x 0.23" ($\sim$ 35x27 au) for $C^{18}O$ (see figures 4.6 and 4.7, respectively). Aditionally, when analyzing the disk emission and in order to avoid the cloud contamination present in the disk, we used a robust weighting of 0.5 for $^{13}CO$ and 1.3 for $C^{18}O$ emission, while excluding large-scale emission by considering only baselines larger than 36m for $^{13}CO$ (scales larger than 6.4", $\sim$740 au) and 45m for $C^{18}O$ (scales larger than 5.11", $\sim$590 au). We also applied uvtapering of 0.2"x0.115" for $^{13}CO$ and 0.2" x 0.0" for $C^{18}O$, in order to obtain a roughly round beam. The final images that trace the disk emission have a beam size of 0.26" x 0.25" ($\sim$ 29 au) for $^{13}CO$ and 0.31" x 0.29" ($\sim$ 35 au) for $C^{18}O$. We imaged all channel maps in both $^{13}CO$ and $C^{18}O$ using a 0.111km s$^{-1}$ spectral resolution, though the $C^{18}O$ data was observed with a finer spectral resolution (0.032km s$^{-1}$), and found the best compromise of SNR by using a broader spectral resolution, matching the available $^{13}CO$ channel widths. The analysis of the CO isotopologue's emission is done in Chapter 4.

Additionally we also imaged emission of CN v= 0, N = 3 − 2 in $J = 7/2 - 5/2$ and $J = 5/2 - 3/2$, the spectral windows for these observations are centered in 340.248 GHz and 340.014 GHz, respectively, however the $J = 5/2 - 3/2$ emission is observed in the border channels of the spectral window, at 340.035 GHz. These molecules are studied separately from the CO isotopologues, but were obtained and imaged following the same procedure regarding self calibration as in the CO. The CN $J = 7/2-5/2$ is imaged with a robust parameter of 1.3, considering baselines larger than 34m to exclude large-scale emission of over 6.5" ($\sim$750au). We apply uvtapering of 0.175" x 0" and obtain a final beam of 0.29"x0.29" ($\sim$34au). CN

$J = 5/2 - 3/2$ is imaged with robust parameter 1.8, using baselines over 35m (excluding emission over 6") and with uvtapering of 0.18"x0.01" to achieve a final beam of 0.3"x0.3" ($\sim$35au). From the channel maps of both CN transitions (see Figures 5.1 and 5.2) we notice that in CN $J = 5/2 - 3/2$ we detect a hyperfine transition, imaging both $F = 3/2 - 1/2$ and $F = 7/2 - 5/2$. A detailed analysis on this emission is done in Chapter 5.

Table 2.2: Gas Imaging Summary

| Molecule | Rest Frequency [GHz] | robust | uv-taper arcsec["] | uv-range [meter] | Synthesized Beam arcsec["] | Peak $I_\nu$ [mJy beam$^{-1}$] | RMS noise [mJy beam$^{-1}$] | Channel Width [km/s] |
|---|---|---|---|---|---|---|---|---|
| $^{13}$CO $J = 3 - 2$ | 330.588 | 0.5 | 0.2 x 0.115 | >36 | 0.26 x 0.25 | 169.456 | 3.3 | 0.111 |
| C$^{18}$O $J = 3 - 2$ | 329.330 | 1.3 | 0.2 x 0.0 | >45 | 0.31 x 0.29 | 105.612 | 4.4 | 0.111 |
| C$^{18}$O $J = 3 - 2$ finer-res | 329.330 | 1.3 | 0.2 x 0.0 | >45 | 0.31 x 0.29 | 116.054 | 6.6 | 0.05 |
| $^{13}$CO $J = 3 - 2$ large-scale | 330.588 | 2.0 | - | - | 0.29 x 0.22 | 178.448 | 3.3 | 0.111 |
| C$^{18}$O $J = 3 - 2$ large-scale | 329.330 | 2.0 | - | - | 0.30 x 0.23 | 81.031 | 4.2 | 0.111 |
| CN $N = 3 - 2$, $J = 7/2 - 5/2$ | 340.248 | 1.3 | 0.175 x 0.0 | >34 | 0.29 x 0.29 | 48.917 | 2.2 | 2.0 |
| CN $N = 3 - 2$, $J = 5/2 - 3/2$ | 340.035 | 1.8 | 0.18 x 0.01 | >35 | 0.30 x 0.30 | 28.121 | 2.2 | 2.0 |

# Chapter 3

# Dust Spiral Structure

*The analysis presented in this chapter is part of a paper titled "Spiral arms and a massive dust disk with non-Keplerian kinematics: Possible evidence for gravitational instability in Elias 2-27" by Paneque-Carreño et al. 2020 (in preparation).*

## 3.1. Previous analysis of Continuum Emission in Elias 2-27

The spiral structure of Elias 2-27 has been analyzed in 1.3mm emission by Pérez et al. (2016) and Huang et al. (2018c). Both studies differ in their angular resolution, ∼0.2" (∼25au) in Pérez et al. (2016) and ∼0.05" (∼6au) in Huang et al. (2018c). As the spiral structure is faint, compared to the inner disk emission, the morphological analysis of the spirals, in both works, was conducted using an enhanced image, obtained through unsharped masking in Pérez et al. (2016) and substracting the azimuthally averaged radial profile in Huang et al. (2018c). Figure 3.1 shows the high resolution emission from Elias 2-27 and the substracted image from Huang et al. (2018c), together with the polar deprojection of both images.

While Pérez et al. (2016) reported in the initial observations of Elias 2-27 the symmetric morphology of the spirals and also the presence of a dust gap located at ∼70au, the high angular resolution of the DSHARP collaboration (Andrews et al., 2018a) allowed these structures to be very precisely traced, therefore, we will describe only the spiral morphology constrains from Huang et al. (2018c) in this matter. From the substracted image (left panel, figure 3.1) the maxima along the spiral arms were traced and modelled with a constant pitch angle logarithmic function. The pitch angle of each spiral was 15.7° and 16.4° for S1 (North-West spiral in this work) and S2 (South-East spiral in this work), respectively. Following the best-fit parametrization, the contrast of the spirals was calculated on the original image. Contrast values are similar, as can be seen in the bottom panels of Figure 3.2, in both spirals there is a local maximum at ∼123 au and a local minimum ∼147 au.

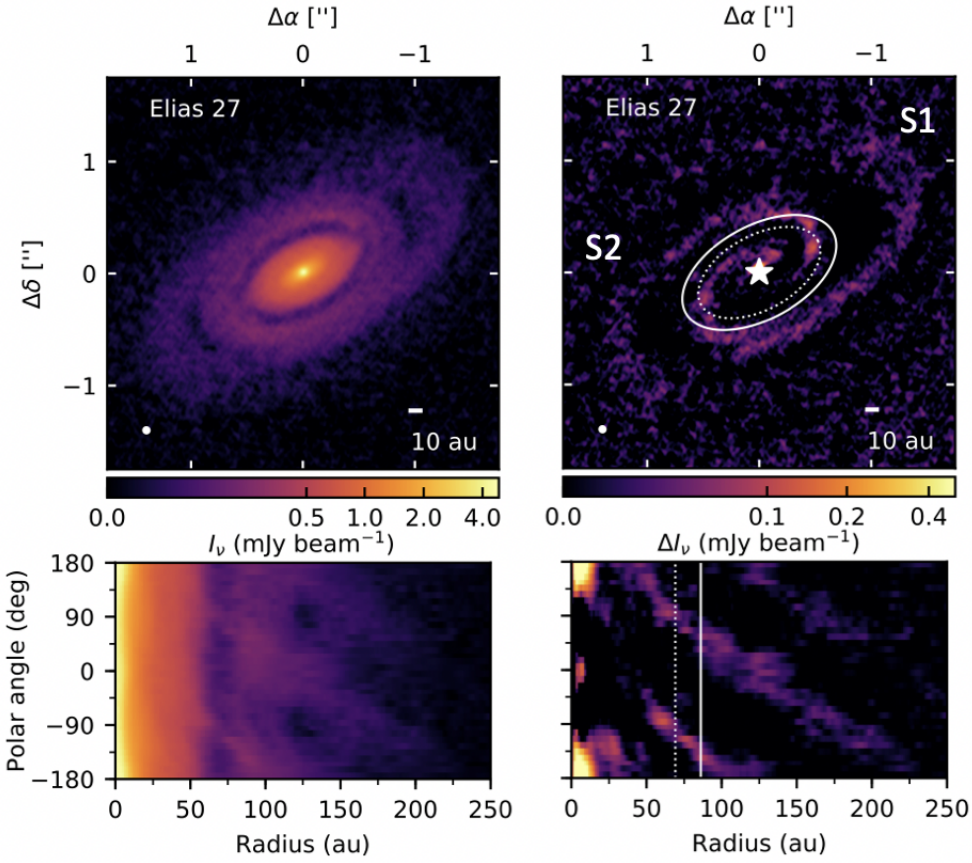


Figure 3.1: Left column shows 1.3 emission of Elias 2-27 at high angular resolution (top) and the polar deprojection of the data (bottom). Right column is the same, but for the substracted data, white star indicates the center of the image and ellipse marks the dust gap's location. Image taken from Huang et al. (2018c).

Huang et al. (2018b) presents an overall study on the annular structure of Elias 2-27, adequately characterizing the dust gap and the disk's inclination and position angles. The dust gap according to their study is located at 69.1 ± 0.4au and has a width of 14.3 ± 1.1au, the depth of the gap is 0.73 ± 0.02 (depth is defined as the intensity ratio at the gap's radial location and the brightest annuli's radial location). If the gap was produced by a planetary companion orbiting at the gap location, Zhang et al. (2018) estimates the planet mass would be 0.02-0.12$M_J$ (values vary depending on the disk viscosity value). The inclination and position angle derived (based on the gap) are, respectively, $56.2^{\odot} \pm 0.8^{\odot}$ and $118.8^{\odot} \pm 0.7^{\odot}$.

Besides the morphology analysis of the spirals, Pérez et al. (2016) performed radiative transfer modelling of the source, to compute the dust temperature and surface density, together with the optical depth radial profile. Their results indicate a total disk mass of $M_{disk}$ = 0.1$M_{\odot}$ (considering gas-to-dust-ratio of 100). Using the constrained temperature surface density profiles, they additionally calculated the Toomre $Q$ instability parameter, to test for the possibility of a GI origin to the spirals. Considering a dust mass opacity of $\kappa_{1.3mm} = 2.3$ $cm^2g^1$ the obtained $Q$ is well within the expected values for a stable regime, with a minimum value of ∼6 at 150au. To obtain values of $Q$<2, a four times lower opacity is needed.

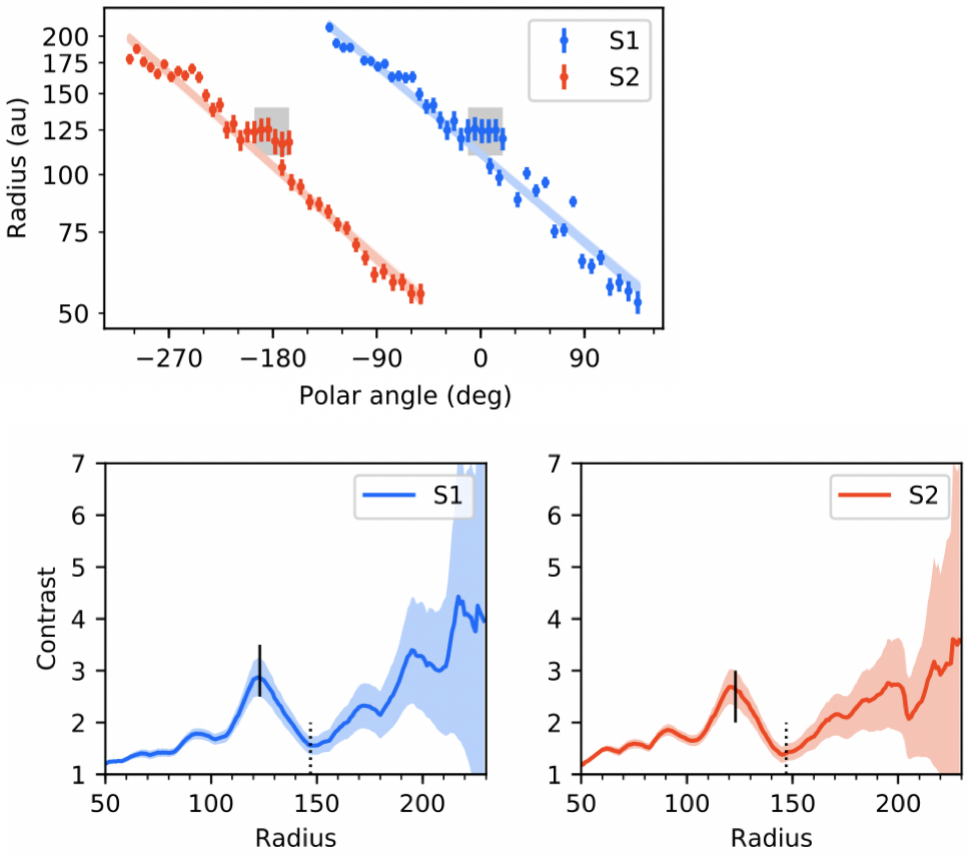


Figure 3.2: Elias 2-27 spiral structure analysis from Huang et al. (2018c). Top row shows logarithmic spiral fit to the deprojected data from tracing the maxima of emission along the spirals in the substracted image. Bottom row shows the contrast analysis along the spiral arms. For further information refer to the original work.

## 3.2. Tracing the Spiral Morphology

We image our continuum dust emission data, as described in Chapter 2, and recover the spiral structure at all wavelengths (0.89mm, 1.3mm and 3.3mm), as shown in Figure 3.3. Given the ∼25au beam size, we are not able to resolve the gap at 69au, which has an estimated width of 14.3au (Huang et al., 2018b), so for all calculations throughout this study, we will assume the gap location as derived in Huang et al. (2018b). In addition, we adopt the position and inclination angles derived in that same work (position angle of 118.8° and inclination of 56.2°).

To trace the spiral structure from our dust continuum images, we radially subtract an azimuthally-averaged radial profile of the emission and trace the spiral features from these "substracted images" (as performed in Huang et al., 2018c). From the subtracted images, shown in the top panels of Fig 3.4, we trace the spirals by finding the radial location of maximum emission along each spiral, at azimuthal steps sampled every 9°, between a determined azimuthal angle range (values in Table 6.2). We then fit a logarithmic spiral model with cons-

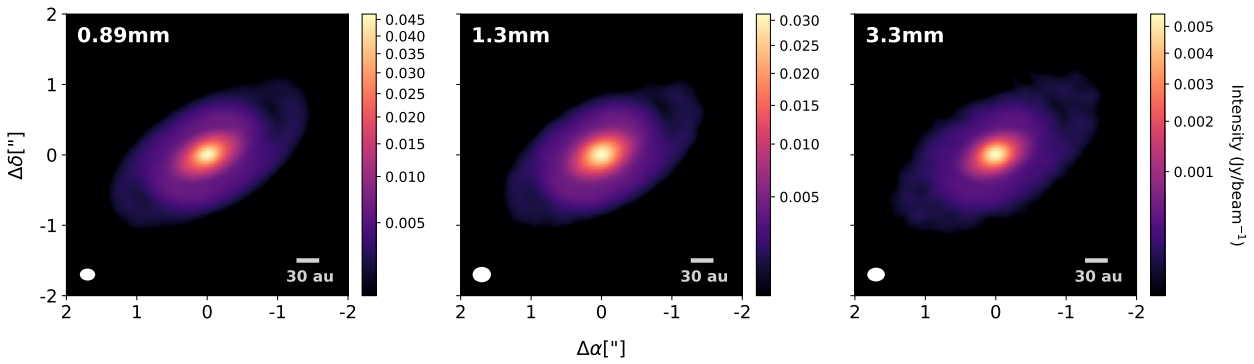


Figure 3.3: Dust continuum observations of Elias 2-27 at 0.89mm, 1.3mm and 3.3mm. For each panel: scale bar values vary as shown to the right of each emission, bar in lower right corner indicates 30au distance and ellipse corresponds to achieved angular resolution (26 au x 20 au in 0.89mm, 30 au x 26 au in 1.3mm and 30 au x 23 au in 3.3mm).

tant pitch angle to the location data of each spiral and wavelength, following $r(\theta) = R_0 e^{b\theta}$. Here $\theta$ is the polar angle in radians measured from the North and to the East (left) , $R_0, b$ are free parameters, with $R_0$ the radius at $\theta = 0$, measured in au, and $b$ relates to the pitch angle of the spiral arms ($\phi$), which can be derived as $\phi = arctan(b)$.

The uncertainty on the location of each measured maxima is assumed to be the astrometric error[1]:

$$\Delta p = 60000 * (\nu * B * SNR)^{-1} \tag{3.1}$$

were $\Delta p$ is the approximate position uncertainty of a feature in miliarcseconds, $SNR$ is the peak/rms intensity ratio of the data point on the image, $\nu$ is the observing frequency in GHz and $B$ is the maximum baseline length in kilometers. For example, at Band 7 (350 GHz), for the 1km baseline configuration (C40-5), and for SNR = 40, the theoretical astrometric accuracy is 4.2 mas.

To obtain the best-fit parametric model we use Markov chain Monte Carlo (MCMC) (Goodman and Weare, 2010) as a method to accurately sample a parameter space, find the best model and estimate the associated errors. This method is implemented with the python package EMCEE (Foreman-Mackey et al., 2019), we need only specify a parameter range and a likelihood function, to determine the similarity between our data set and the proposed model. In MCMC the number of times the parameter space is sampled will be determined by the amount of steps and walkers that are chosen. At each step, a walker will represent a determined set of parameters and the resulting model with those parameters will have its likelihood value calculated. In each subsequent step, the walkers will favor parameters where the likelihood of the model with respect to the data increases. The number of steps must be

[1] see https://almascience.nrao.edu/documents-and-tools/cycle5/alma-technical-handbook/view for further details.

Table 3.1: Parameters Logarithmic Spiral model

| Wavelength | Spiral Arm | Angle Range | $R_0$ [au] | $b$ | Pitch Angle |
|---|---|---|---|---|---|
| 0.89mm | NW | -251° to -5° | $249.8^{+1.2}_{-1.1}$ | $0.230 \pm 0.002$ | $12.9° \pm 0.1°$ |
| | SE | -70° to 150° | $111.5^{\pm}0.4$ | $0.247 \pm 0.003$ | $13.9° \pm 0.2°$ |
| 1.3mm | NW | -250° to -35° | $250.2^{+2.3}_{-2.5}$ | $0.229^{+0.003}_{-0.004}$ | $12.9° \pm 0.2°$ |
| | SE | -61° to 135° | $115.5^{+0.8}_{-0.9}$ | $0.234 \pm 0.007$ | $13.2° \pm 0.4°$ |
| 3.3mm | NW | -260° to -23° | $249.9^{+3.9}_{-3.8}$ | $0.229 \pm 0.005$ | $12.9° \pm 0.3°$ |
| | SE | -50° to 140° | $113.6^{+1.0}_{-1.1}$ | $0.231 \pm 0.010$ | $13.0° \pm 0.6°$ |

sufficient to assure convergence of the walkers to a parameter space, avoiding local likelihood maxima and finding the optimum parameter values for the model. From the posterior values, corresponding to the parameter values sampled by the walkers after convergence, we may obtain an estimate of the best-fit parameters by calculating the median value. The errors on the model are usually estimated taking into account the 16th and 84th percentile values of the posteriors. In our likelihood function for the parametric model of the spiral arms, we weigh each data point by the astrometric error (Equation 3.1) in this way our model will be dominated by the data points of higher SNR.

The top panel of Figure 3.4 shows the traced maxima along each spiral from the substracted images. In the middle panels are the deprojected radial locations of each maxima, measured from the center, as a function of azimuthal angle. The azimuthal angle is measured from the North, towards the East (left). Grey lines show logarithmic spiral models, derived from 300 draws of the posterior values after convergence of the MCMC chains used to find the best-fit parameters of each arm. The horizontal line at 148au marks the location where we observe a break in the spiral arm, at all wavelengths, clearest in the South-East spiral, however also subtly present in the North-West spiral. The bottom panel (Fig. 3.4) shows the polar deprojection of the subtracted data, with a vertical line marking the dust gap location from Huang et al. (2018c) at 69au. The red/blue lines show the best-fit model for the logarithmic spirals. The median value for the parameters of the logarithmic spiral model, for each spiral and wavelength, are shown in Table 3.1, along with the 16th and 84th percentile uncertainties derived from the posteriors. We note that the pitch angle values retrieved here, $\sim 12.9°$ and $\sim 13.5°$, for NW and SE spiral respectively (similar between wavelengths, see Table 3.1), are different than the recovered pitch angles from Huang et al. (2018c) (15.7° and 16.4°, for NW and SE spiral). When applying our method to the high-resolution dataset presented in Huang et al. (2018c), we retrieve the same results as in their work, therefore the pitch angle difference between this work and theirs is probably due to beam smearing effects, given the angular resolution difference of a factor of 4-5 between both datasets.

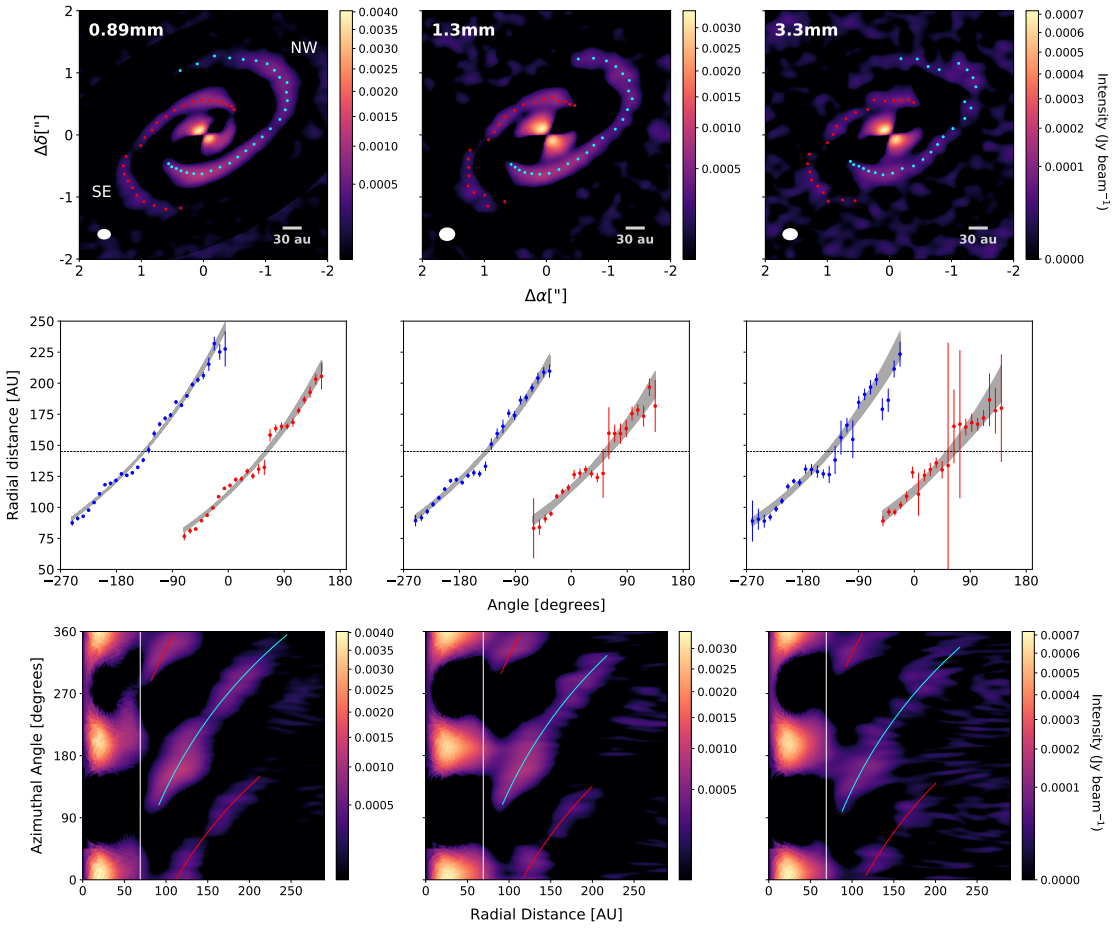


Figure 3.4: The spiral morphology of Elias 2-27 at multiple wavelengths. Panels from left to right correspond to data from the 0.89mm, 1.3mm and 3.3mm observations. North-West spiral is traced in blue, South-East spiral is traced in red. Top panels: Dust continuum maps from which the azimuthally averaged radial profile has been subtracted to highlight spiral location, red and blue points trace the maxima of emission along the spiral arms. Middle panels: Deprojected radial location of the previously found emission maxima, as a function of angle measured from the North and to the East. Error bars correspond to the astrometric error of each data point and grey lines show the posterior distribution of the logarithmic spiral with constant pitch angle fit. Bottom panels: Deprojection of the subtracted dust continuum observations from the top panels. The vertical line marks the dust gap location from Huang et al. (2018c), and colored lines show the best-fit logarithmic spiral model.

## 3.3. Contrast variations along the Spiral

The observations of each wavelength $\lambda$ will be sensitive to particle sizes of a $\sim \lambda/(2\pi)$ (Boehler et al., 2013). Assuming optically thin emission, we can consider that the mass (M) in a certain sector of the disk will be proportional to the flux, so sectors of larger flux concentrate a larger density of grains than sectors of less flux. This is relevant because tracing the relative difference in flux between sectors of a disk will give us a measure of where the particles are more densely concentrated, this relative measurement is the contrast. In the case of Elias 2-27, we are interested in testing the contrast at comparable locations over different wavelengths, for this may provide evidence of dust trapping. If indeed there is dust growth being excited within the spiral arm or large particles are trapped at this location, then at longer wavelengths we could expect to observe higher contrast. The latter is due to larger particles being more densely packed in the spiral arm region than in the inter-arm region, an effect has been shown to occur in the case of dust-trapping vortex studies (Cazzoletti et al., 2018a).

We compute how the contrast varies radially along each spiral arm, with respect to a fixed "inter-arm" region, which is expected to be a location were we can be sure there is no emission from the spiral arms. Considering the symmetry between the spirals, the inter-arm region of each spiral is assumed to follow the same shape of the corresponding spiral arm, but rotated by 90 degrees clockwise from the spiral location, given that they are defined as trailing (Pérez et al., 2016; Huang et al., 2018c) (if they had been symmetric leading spirals we would have defined the inter-arm region by rotating the spiral location anticlockwise 90 degrees). The top panels of Figure 3.5 shows a polar projection of the dust continuum, overlayed are the best-fit model of the spirals for each wavelength in continuous line and this same model, shifted 90 degrees clockwise, tracing the inter-arm region, in dashes. From this figure it is clear that the interarm region effectively traces zones of lower emission, compared to the spiral arm location.

The contrast is calculated, from the original images, as the ratio between the emission at the spiral and the inter-arm region, at each radius and for both spiral arms. We use the previously derived parameters and calculate the contrast along the best-fit spiral model for each wavelength, binning the data azimuthally every 15° and associating the standard deviation, within the bin, as the error of each averaged flux measurement, both for the interarm and spiral region. The error of each measurement is then propagated accordingly in the contrast calculation. The contrast curves for each wavelength are shown in the bottom panels of Figure 3.5. The NW spiral remains the strongest spiral at all wavelengths with an average contrast value 25-33 % higher than the SE spiral. Both spirals maintain a similar contrast throughout their radial extent, deviating in the 0.89mm and 1.3mm observations only ∼11 % from the average contrast value in the case of the SE spiral and ∼17 % in the case of the NW spiral. In the 3.3mm data the contrast variation increases and deviations from the average value increase to ∼16 % in the SE spiral and ∼24 % in the NW. For the 0.89mm, 1.3mm and 3.3mm emission, the radial distance of the maximum contrast value is, respectively for (NW, SE) spirals, (∼125au, ∼117au), (∼129au, ∼127au) and (∼129au, ∼126au). For the minimum contrast location, in the same order, the radial distances are (∼155au, ∼149au), (∼161au, ∼147au) and (∼150au, ∼142au). We observe in our contrast curves that the radial

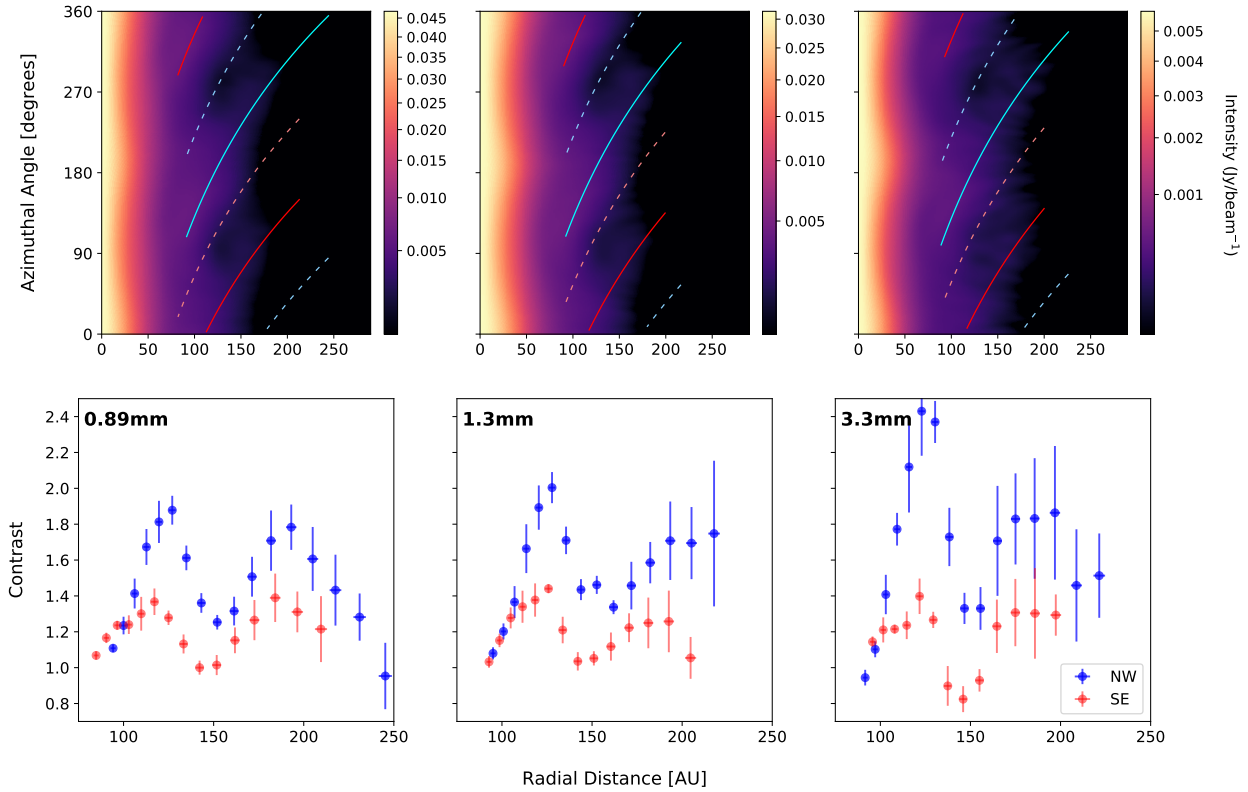


Figure 3.5: All panels from Left to Right correspond to data from the 0.89mm, 1.3mm and 3.3mm observations. Top: Polar Deprojection of the dust continuum, the azimuthal angle is measured from the North and to the East. North-West spiral is traced in blue, South-East spiral is traced in red following the best-fit parameters. Dashed lines trace the inter-arm region, following the same best-fit parametric model, but minus 90 degrees from the spiral. Bottom: Calculated contrast values along each spiral.

location of the maximum contrast slightly shifts outwards with wavelength, no global shifts are detected in the minimum contrast distances, however the minimum contrast of the SE spiral appears to shift inwards at longer wavelength. Overall our values are within agreement with previous measurements of Huang et al. (2018c) where the peak contrast is located at ∼123au and low contrast at ∼147au (measured from higher angular resolution 1.3mm data). While the form of the contrast curve in the 1.3mm emission agrees also with the previous studies (Pérez et al., 2016; Huang et al., 2018c), at larger radial distances we observe a decrease in the contrast of both spirals in the 0.89mm emission and also in the SE spiral in 3.3mm, contrary to the apparent growing contrast at larger radial distance observed in the 1.3mm emission.

If we follow the peak contrast of both spirals, located at ∼125 au, we see a slight variation in the contrast value, which grows larger with longer wavelength. The peak contrast value of the NW spiral increases 11 % from the 0.89mm to the 1.3mm emission and 8 % between the 1.3mm and 3.3mm emission. The SE spiral increases its peak contrast value 5 % initially and in the 3.3mm data decreases the peak contrast by 2 % with respect to the 1.3mm emission. Low

contrast values shift, but do not show any correlation with varying wavelength. We note that previous studies on this source measured the contrast differently, using the ratio between the spiral flux and the minimum flux at the same radial location (Huang et al., 2018c; Pérez et al., 2016). We do not follow this technique, because the minimum flux at a determined radial distance is found at different azimuthal angles between different wavelenghts. Therefore, the contrast calculated using the minimum radial flux will not sample comparable locations between different wavelengths, something critical in order to try to detect possible signatures of dust growth at a given location, which we achieve by using the interarm region.

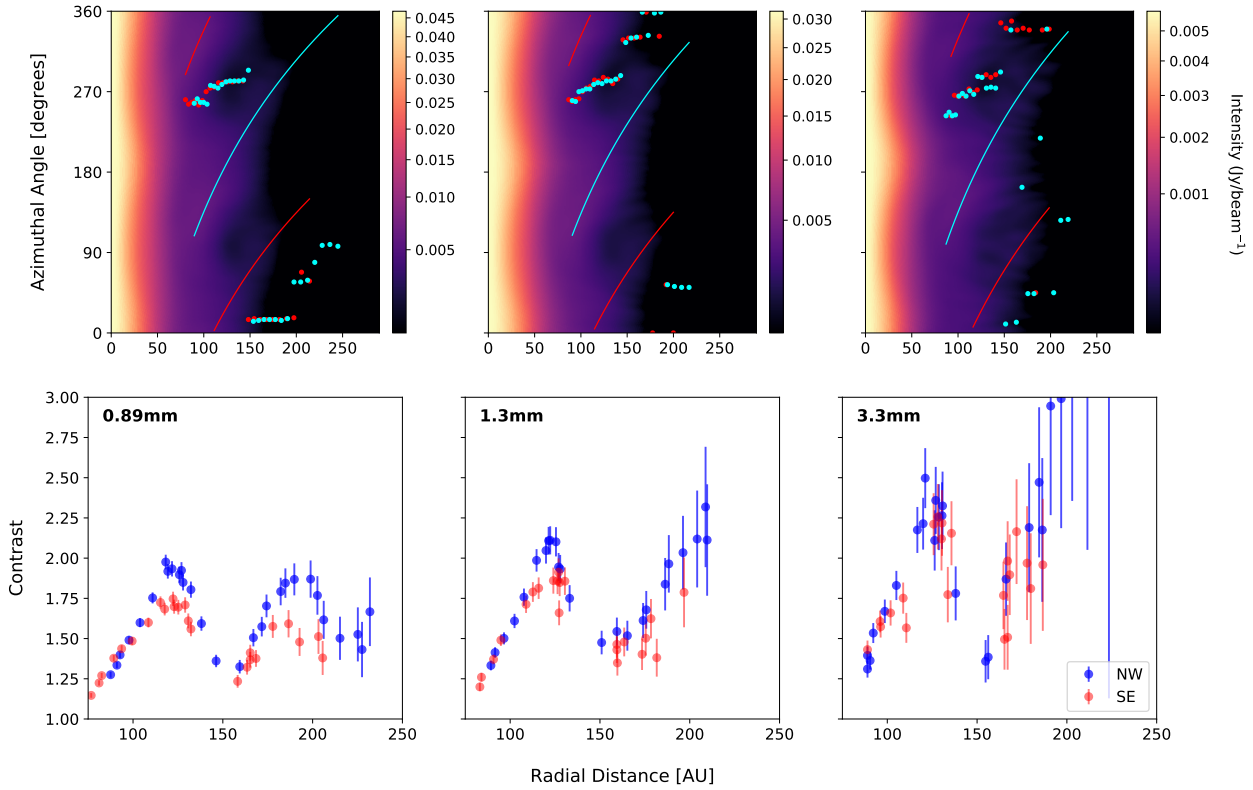


Figure 3.6: Contrast calculation following minimum flux method. Panels show same information as in Figure 3.5, but Top row shows location of minimum flux (filled dots) instead of inter-arm region.

For completeness, we test our results using the minimum flux method used in the other studies, sampling the spiral arms at the same location as the retrieved maximas for the parametric model. The resulting curves are shown in Figure 3.6, these contrast curves also showed increasing contrast at longer wavelengths, more strongly than with our method and also showed similar radial positions for maximum and minimum contrast. From Figure 3.6 we can see that the azimuthal locations of the minimum flux are not comparable between wavelengths, for they are not in the same location. We conclude that to effectively trace comparable contrast variations between different wavelength we must use a constrained interarm region. However, an interesting conclusion we can derive from using the minimum flux location is how the contrast of the spirals within a same wavelength compare, with respect to a similar location, we can't do this with the interarm region because it varies between both spirals, for a same wavelength. Figure 3.6 shows that compared to a roughly same location (the minimum flux), both spirals have very similar contrast between them at all

radii, varying only 4-13 % between them, with the highest difference at 0.89mm and the most similar contrast at 3.3mm (NW remains the brightest spiral at all wavelengths).

## 3.4. Spectral Index Analysis

The presence of dust growth throughout the disk can be inferred using the multi-wavelength dust continuum observations to compute the disk spectral index. In the Rayleigh-Jeans regime, the spectral index ($\alpha$) of the spectral energy distribution follows $I_\nu \propto \nu^\alpha$, where $I_\nu$ corresponds to the measured intensity, from the image plane, at frequency $\nu$. If $\alpha$ has values between 2-2.5 it can be an indicator towards the presence of large, up to cm-sized, grains and hence dust growth at the location of such values (e.g., Testi et al., 2014; Pinilla et al., 2017; Cazzoletti et al., 2018a; Macías et al., 2019). We initially calculate $\alpha$ as the best-fit slope of a linear model applied in the logarithmic space ($\alpha \propto lnI_\nu/ln\nu$), using all wavelengths available in this study. The $\alpha$ values we obtained were much lower than expected in an optically thin regime (presumed to be the case at large radii for Elias 2-27, Pérez et al., 2016; Huang et al., 2018b) were $\alpha$ should not be lower than 2, however, in this case, we retrieve a disk average $\alpha$ value of 2.0±0.2, with lower values in the inner ∼85au, as shown in Figure 3.7.

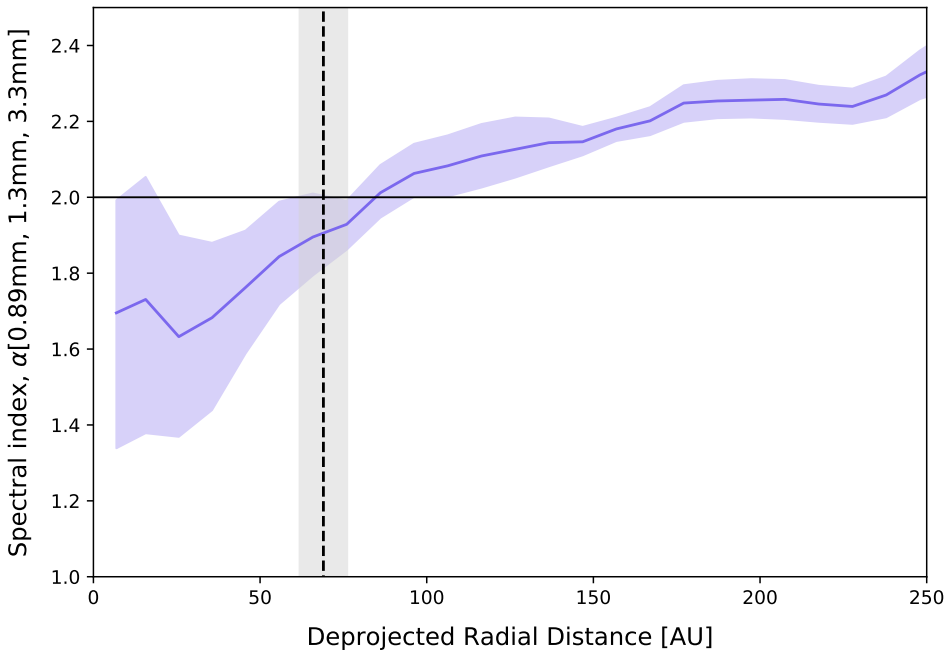


Figure 3.7: Spectral index radial profile calculated using all available wavelengths (0.89mm, 1.3mm, 3.3mm). Vertical dashed line marks dust gap location (69au), shaded area shows the width as determined in Huang et al. (2018b)

To search for the origin of these low $\alpha$ values, we compute the spectral index between two wavelengths at a time, using the azimuthally averaged intensity profiles (same beam for all wavelengths). The azimuthally averaged intensity and $\alpha$ radial profiles are shown in the top panels of Figure 3.8 calculated following;

$$\alpha_{\nu_1,\nu_2} = \frac{lnI_{\nu_1} - lnI_{\nu_2}}{ln\nu_1 - ln\nu_2} \tag{3.2}$$

From these $\alpha$ radial profiles, a clear deviation from the expected overall $\alpha \gtrsim 2$ values can be seen when computing the spectral index including the 0.89mm emission, especially when combining it with the 1.3mm data. We apply the same techniques described in Huang et al. (2018b) to calculate the optical depth at our various wavelengths. The main assumption relies on approximating the midplane temperature profile ($T_{mid}$), assuming a passively heated, flared disk in radiative equilibrium (e.g., Chiang and Goldreich, 1997) and considering that the millimeter emmission follows this temperature profile, if it traces the midplane. From the temperature profile, we compute the expected blackbody emission ($B_\nu$), using Planck's law, and relate it to the measured intensity ($I_\nu$) through $\tau_\nu$, following $I_\nu(r) = B_\nu(T_{mid}(r))(1 - exp(-\tau_\nu(r)))$. $T_{mid}$ will depend on the assumed flaring of the disk and the stellar luminosity (we use the DSHARP values for flaring and stellar luminosity of $\varphi = 0.02$ and $logL_* =$ -0.04 $\pm$ 0.23 $L_\odot$, Andrews et al., 2018a). The computed optical depth profiles are shown in the bottom panel of Figure 3.8, these also show an anomalous behaviour for $\tau_{0.89mm}$, which should display higher optical depth than the other wavelengths at all radial distances, but instead is located between $\tau_{1.3mm}$ and $\tau_{3.3mm}$ inwards of $\sim$ 175au. These constraints in $\alpha$ and $\tau_\nu$ indicate that the 0.89mm emission is likely to be more optically thick than what we assume, and possibly traces a different layer of emission all together with a different temperature value. The latter is why, when assuming the 0.89mm emission comes from a layer with the same temperature as the other wavelengths, it displays $\tau$ values between the other wavelengths. We check if these discrepancies may be explained by absolute flux scale errors in the 0.89mm data, but to obtain reasonable $\alpha$ and $\tau$ values, a $\sim$70 % higher intensity is required. For the flux calibrators observed at 0.89mm, we only recover a $\sim$4 % flux difference between pipeline and catalogue flux density values in the short baseline observations, while in long baseline observations there is no discrepancy. Thus, an error in the absolute flux scale is unlikely, and more likely, the continuum emission observed at 0.89mm is highly optically thick, comes from a higher layer than the midplane, and the dust particles at this higher layer have lower temperature than the $T_{mid}$ calculated before.

Considering the latter analysis, we compute a 2D $\alpha$ map only using the 1.3 and 3.3 mm datasets. For the 2D maps, the error on each pixel intensity measurement is the rms ($\sigma$) of the corresponding image and we consider only emission over 5$\sigma$. In order to accurately compute $\alpha$ we smooth both images to the same spatial resolution (0.26" x 0.26", $\sim$31au) and center them to their peak brightness. The maps showing the spectral index values and its associated uncertainty over the whole disk are presented in Figure 3.9. We note that, even when considering these two wavelengths, there are also $\alpha$ values below 2.0 in the inner radii (<50au), this will be discussed in section 7.1 and is probably related to optically thick emission when considering self-scattering at long wavelengths.

If the spiral arms where trapping dust, Dipierro et al. (2015) predicted that a spiral shape should be apparent in the spectral index map, with larger grains expected along the spiral arms creating lower $\alpha$ values at that location. In the $\alpha$ map, the best-fit spiral model from the 1.3mm dust emission is overlaid for reference, along with the dust gap location (69au), we also show the contour lines for $\alpha$ values of [2.0, 2.4, 2.6], in the error map we contour $\alpha$

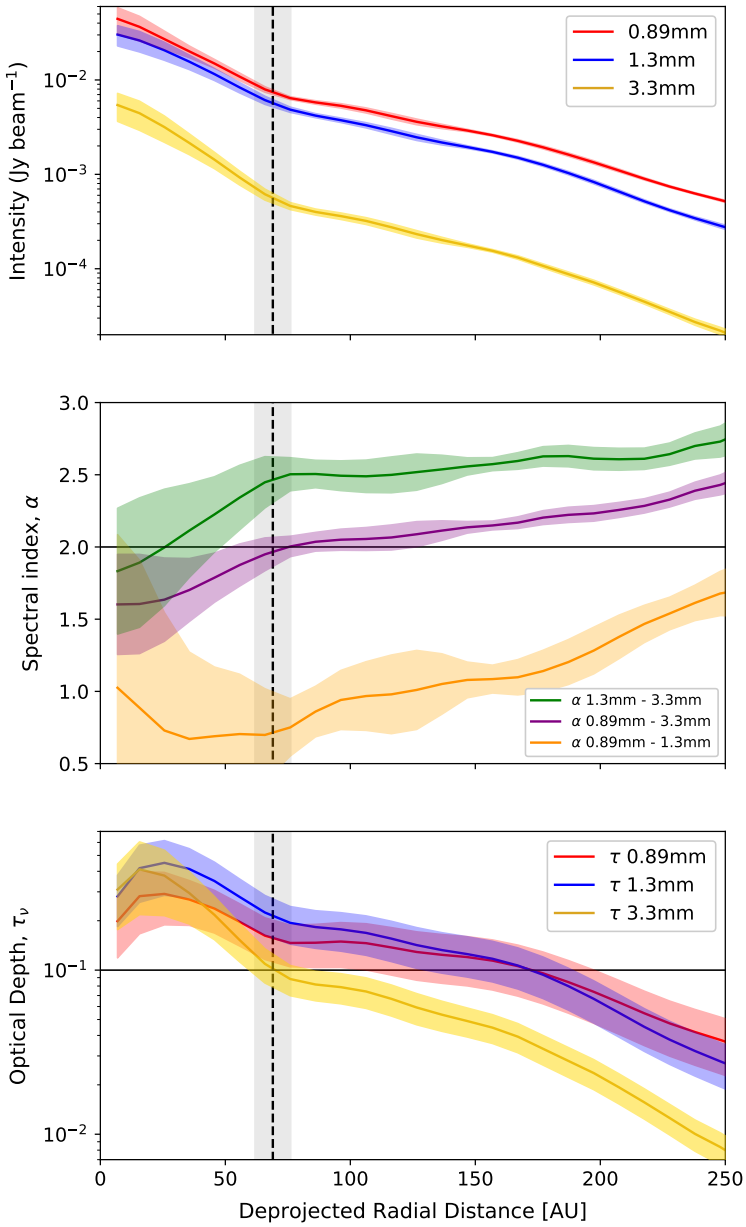


Figure 3.8: Top Panel: Azimuthally averaged intensity radial profiles for each wavelength emission, shaded area shows the $1\sigma$ scatter at each radial bin divided by the beams spanning the angles over which the intensities are measured. Middle Panel: Spectral index radial profile for each pair of wavelengths, shaded area shows $1\sigma$ errors from assuming the intensity error from the azimuthally averaged intensity profile. Lower Panel: Optical Depth radial profile for each wavelength, shaded area shows $1\sigma$ errors considering the $1\sigma$ errors on the stellar luminosity value and from the azimuthally averaged intensity profile. Vertical dashed line marks dust gap location (69au), shaded area shows the width as determined in Huang et al. (2018b).

uncertainties at the level of [0.01, 0.05, 0.1, 0.2].

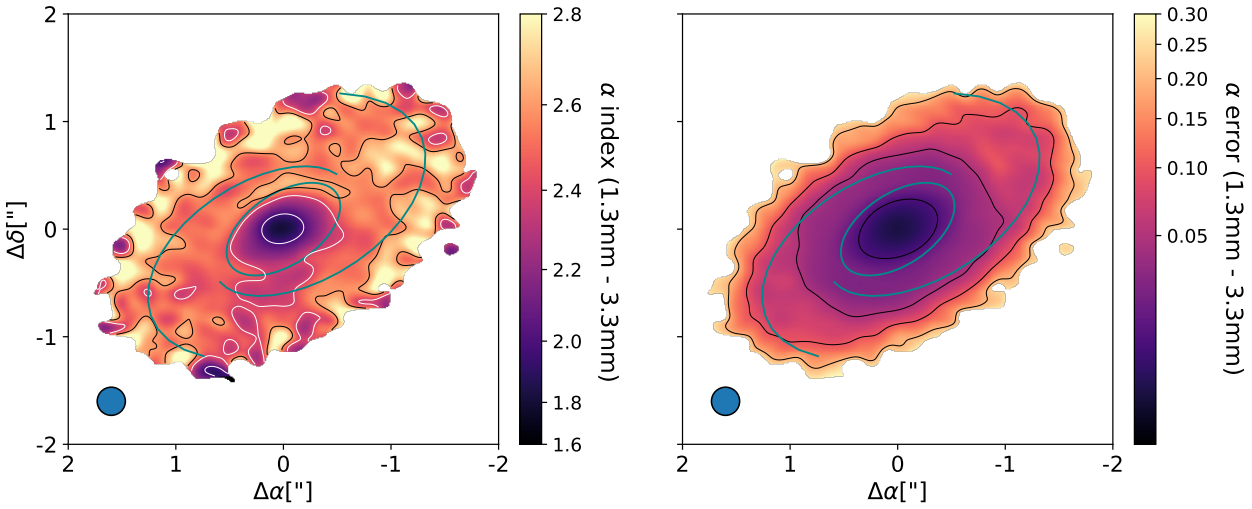


Figure 3.9: Left: Spectral index map calculated using 1.3mm and 3.3mm emission, only emission over $5\sigma$ in the image plane is considered. Blue lines show the location of the dust gap at 69au and the derived best-fit parametric model for the spiral arms of 1.3mm emission. White lines trace contours for $\alpha$ values 2.0, 2.4 and black lines indicate 2.6 level contour. Right: Spectral index error map, obtained from the image rms and intensity value of each pixel. Blue lines trace the dust features and black lines the contours at 0.01, 0.05, 0.1 and 0.2.

We observe that while there is no clear spiral shape, the $\alpha$ variations aren't perfectly radial either. In the outer disk, uncertainties in $\alpha$ are $\sim 0.1$, while $\alpha$ varies by less than 0.1 between the spiral and the inter-arm region, so we cannot ascertain significant variations there. In the inner disk, close to where the spirals start in the spiral model, the uncertainties in $\alpha$ are $\sim 0.03$, while $\alpha$ varies by $\sim$0.15 between the location of the spiral and the gap location, for both the SE and NW spirals. Although this gives a hint of spectral index variations of the spirals as compared to its surroundings, they are not fully spatially resolved by our beam (shown in blue in the lower left corner of each map). Overall, we do not observe clear and resolved variations in $\alpha$ co-located with the spiral features. At the gap location no particular behaviour is observed, except for a decrease in $\alpha$ values inwards from the gap location.

Another indicator of dust growth is that smaller grains, with lower Stokes number and traced by shorter wavelengths, will be less concentrated than larger grains observed at longer wavelengths. This will translate in a width difference along the dust-trapping structure, such that smaller grains will be more widely spread than larger grains within a dust-trap. Such behaviour has been constrained in different sources with vortex-like structures, likely tracing dust traps (Casassus et al., 2015; van der Marel et al., 2015; Cazzoletti et al., 2018a; Casassus et al., 2019). As the spirals of Elias 2-27 are faint, it is hard to distinguish them in the azimuthally averaged intensity profile (see Andrews et al., 2009; Huang et al., 2018b), which is why it is necessary to use subtraction techniques to enhance them, such as those used in this work and previous publications (Pérez et al., 2016; Huang et al., 2018c). The measurement of the width variation can't be done using a subtracted image or an azimuthally averaged profile, both options would introduce artifacts or remove relevant emission, therefore, we must use

the original image. We decide to trace variations along a single azimuthal cut, choosing the angle were the highest spiral contrast is observed, which is located at ∼125au corresponding to ∼224°.

Figure 3.10 shows the normalized intensity along the azimuthal angle of maximum spiral contrast (224°) for all three wavelengths, the spirals can be localized as a bump in the intensity curve between 100au-150au in the top panel. The middle panel zooms in on the spiral structure emission, to compare the morphology between wavelengths the normalized intensity of the 3.3mm emission was multiplied by two in this panel. From this it can be seen that the shape of the intensity curve is similar at all three wavelengths, with no noticeable width differences. The bottom panel shows the spectral index distribution along the azimuthal cut, calculated directly from the top panel intensity profile, as previously done for the spectral index map, using only the 1.3mm and 3.3mm emission. In this $\alpha$ profile we see that the East side (negative radial distance) shows a decrease in the spectral index value at the spiral location, while the West spiral does not show significant $\alpha$ variations; we note that the spatial extent of the variation is resolved by our beam size (0.26", ∼31au). We test with other azimuthal cuts, around the location of the maximum contrast and the East side consistently shows lower $\alpha$ values at the SE spiral location, these panels are shown in Appendix A.

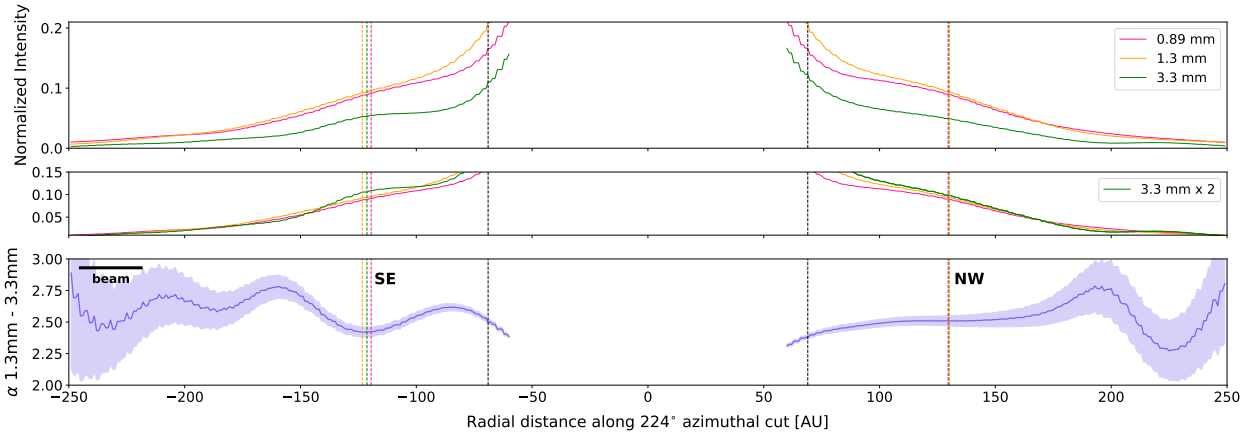


Figure 3.10: Top and Middle panels show the normalized intensity curves for 0.89 mm, 1.3 mm and 3 mm emission along the azimuthal angle of maximum spiral contrast (224°), measured radially from 60au to 250au. Positive radial values are measured from the center of the disk and to the West, negative values indicate distance to the East. Vertical coloured dashed lines indicate the location of the spiral arm according to the best-fit parametric model at each wavelength, black line indicates the location of the dust gap. In the middle panel the normalized 3mm emission has been scaled, multiplied by two. Bottom panel shows the spectral index along the azimuthal cut, calculated from the 1.3mm and 3.3mm emission.

# Chapter 4

# Gas distribution as traced by CO isotopologues in Elias 2-27

*The analysis presented in this chapter is part of a paper titled "Spiral arms and a massive dust disk with non-Keplerian kinematics: Possible evidence for gravitational instability in Elias 2-27" by Paneque-Carreño et al. 2020 (in preparation).*

## 4.1. Previous analysis of CO isotopologues in Elias 2-27

Analysis of kinematic tracers in Elias 2-27 has been challenging due to the considerable cloud absorption that affects the system, especially in the East side (Andrews et al., 2009; Pérez et al., 2016; Andrews et al., 2018a). Even with this consideration, observations of $^{12}$CO, $^{13}$CO and C$^{18}$O have been published, in $J = 2 - 1$ transition (Pérez et al., 2016; Andrews et al., 2018a). Figure 4.1 shows the channel maps for the $^{12}$CO and C$^{18}$O emission, as presented in (Pérez et al., 2016), where the $^{12}$CO was used to estimate the stellar mass through the position-velocity diagram of the emission, obtaining $0.5\pm0.2 M_{\odot}$. Andrews et al. (2018a) also obtained $^{12}$CO data, in the same transition, but at the higher angular resolution of their survey ($\sim$0.1", compared to $\sim$0.4" in Pérez et al., 2016). Through the high angular resolution $^{12}$CO data, Huang et al. (2018c) determined the disk geometry from kinematical constraints, through analysis of the brighter front side of the disk (emitting layer in front of the midplane as viewed by the observer) with respect to the back side (emitting layer behind the midplane as viewed by the observer). The infered geometry and source rotation motion is shown in Figure 4.2.

More recently Pinte et al. (2020) searched for deviations from expected Keplerian motion in the high angular resolution channel maps and suggested that there was a planetary companion perturbing the gas, located within the dust continuum gap location. Figure 4.3 shows the selected channel maps for this analysis and the proposed location of the planetary companion. The coarse spectral resolution does not allow for a precise measurements on the spatial and velocity extent of the detected perturbations.

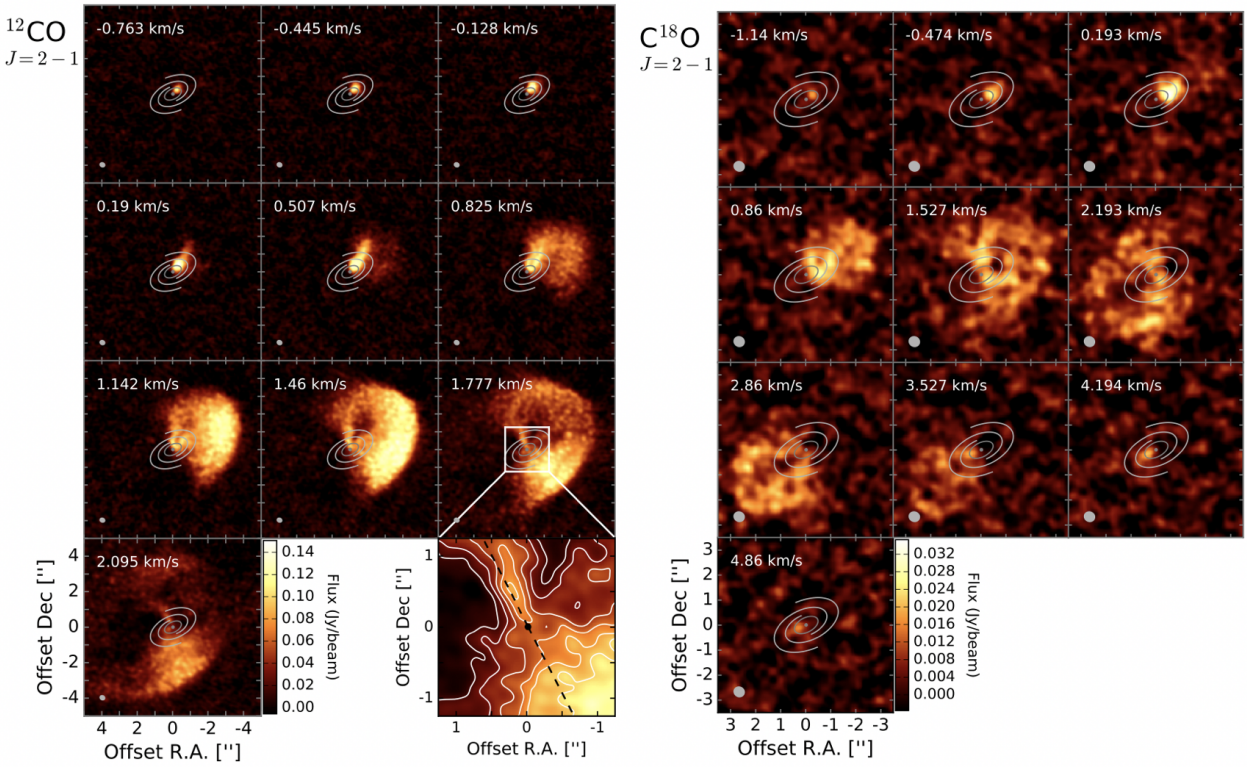


Figure 4.1: $^{12}$CO and C$^{18}$O channel maps from Pérez et al. (2016), overlayed is the best-fit spiral model as derived from their work.

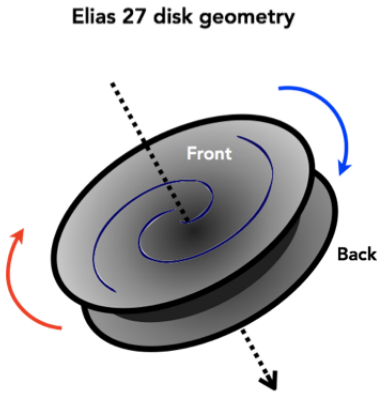


Figure 4.2: Schematic of disk orientation and rotation direction as shown in Huang et al. (2018c). Colored arrows show the directions of redshifted and blueshifted emission. Spirals are shown for reference, but are not scaled or correspond to a best-fit model.

## 4.2. Channel and moment maps

We analyze the emission from the two observed CO isotopologues in three different ways: 1) studying the presence of structures in the integrated emission and in channel maps, including large-scale emission in the entire field-of-view (FOV), 2) detecting velocity perturbations

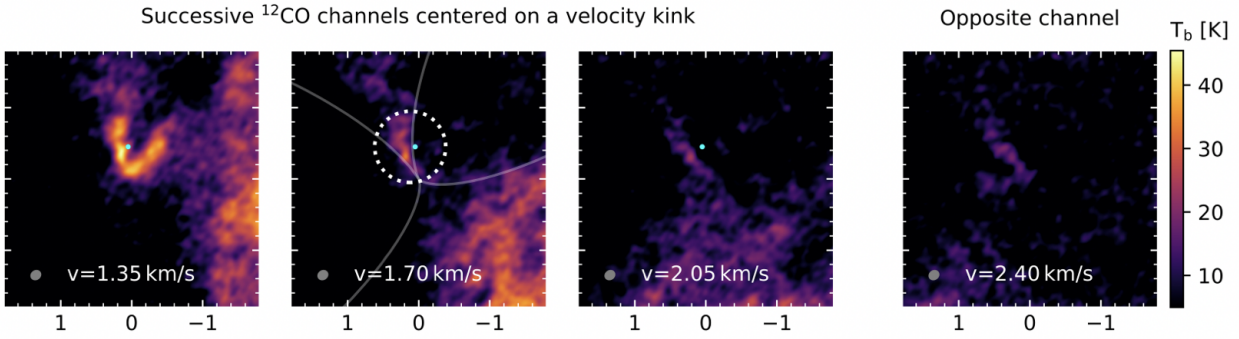


Figure 4.3: Candidate velocity kinks detected in the DSHARP data by Pinte et al. (2020). Dashed circle indicates the velocity kink, and the cyan dot the location of the planet assuming it is in the disk midplane.

in channel and velocity maps, 3) constraining the vertical location of the $^{13}$CO and C$^{18}$O emitting layer, and analyzing the kinematics of these isotopologues.

The channel maps for both $^{13}$CO and C$^{18}$O, are shown in Figures 4.4 and 4.5, respectively. The known cloud absorption (Pérez et al., 2016; Huang et al., 2018c) affects the East side of the disk and blocks all $^{13}$CO emission from $v \geq 2.88$ km s$^{-1}$, while for C$^{18}$O some cloud absorption is present near $v = 2.55 - 2.66$ km s$^{-1}$. We note that the South part of the disk is the brightest and the systemic velocity is determined to be 1.95 km s$^{-1}$ based on the C$^{18}$O channel map analysis at the highest imaged spectral resolution (0.05km s$^{-1}$) and the kinematic modelling using the EDDY package (Teague, 2019).

First, the channel maps that includes all spatial scales probed by these observations (Figures 4.6 and 4.7 for $^{13}$CO and C$^{18}$O, respectively) indicate that extended emission appears in both isotopologues around Elias 2-27. As $^{13}$CO is the most abundant isotopologue of the two observed, this large-scale emission appears more strongly and along a larger range of velocities than in C$^{18}$O (extended emission is clearly identified between $v = 2.55 - 4.88$ km s$^{-1}$ for $^{13}$CO, and between $v = 2.66 - 4.21$ km s$^{-1}$ for C$^{18}$O). This large-scale emission appears to have a striping pattern probably due to the lack of compact baselines in our existing observations (the shortest baseline is 15m, which projected in the sky for the observed frequencies should recover emission from $\lesssim$15" scales, however, the detected emission may extend beyond our $\sim$20" field of view).

From the channel maps we can build an integrated intensity profile as a function of the channel velocity for each molecule, as shown in Figure 4.8. We compare the intensity profile from channels considering only disk emission and channel maps with the large-scale emission. In Figure 4.8 the vertical line marks the systemic velocity (1.95km/s), higher velocities are related with the East side, were the effect of the large-scale emission is evident. Both isotopologues show a peak of excess emission at $\sim$2.5 km/s in the $^{13}$CO data and $\sim$2.7 km/s in the C$^{18}$O data. This peak emission comes from the large-scale emission, when only considering the disk emission the intensity profile is more symmetric. If we consider only the disk emission, the cloud absorption is evident, in the $^{13}$CO amplitude we see a sharp fall in the emission, in comparison, we see that the C$^{18}$O intensity is more symmetric, though it also has a decrease in emission in the higher velocity channels.

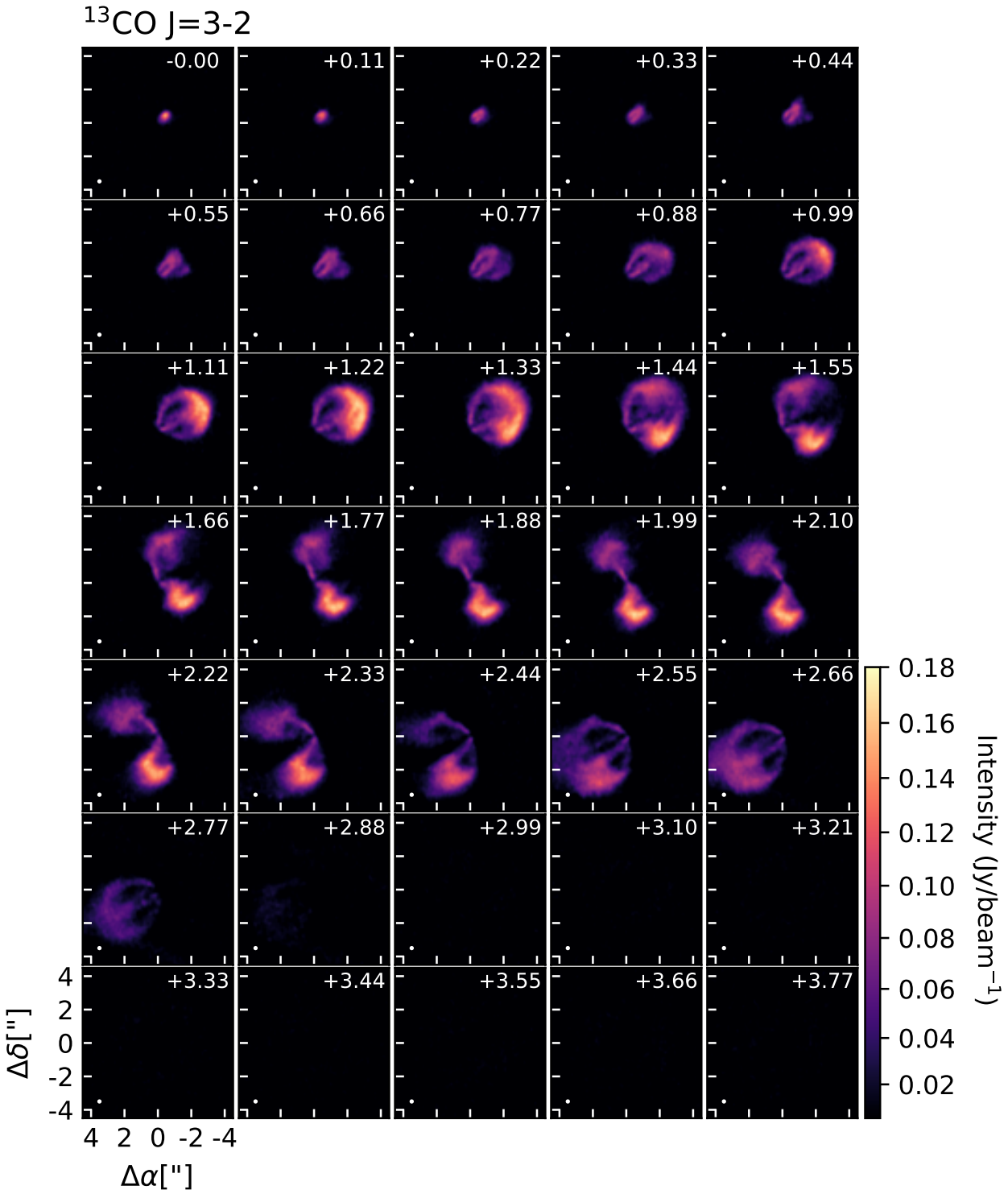


Figure 4.4: Individual emission of each channel for $^{13}$CO isotopologue, corresponding velocities are written in the top right of each panel.

For the data considering the large-scale emission contribution, Figure 4.9 shows the integrated emission and mean velocity maps, only including emission above $4\sigma$. Despite our lack of uv-coverage at short spacings, we see that large-scale emission appears on the East of the disk for the tracer of denser material (C$^{18}$O) and in $^{13}$CO the extended emission shares

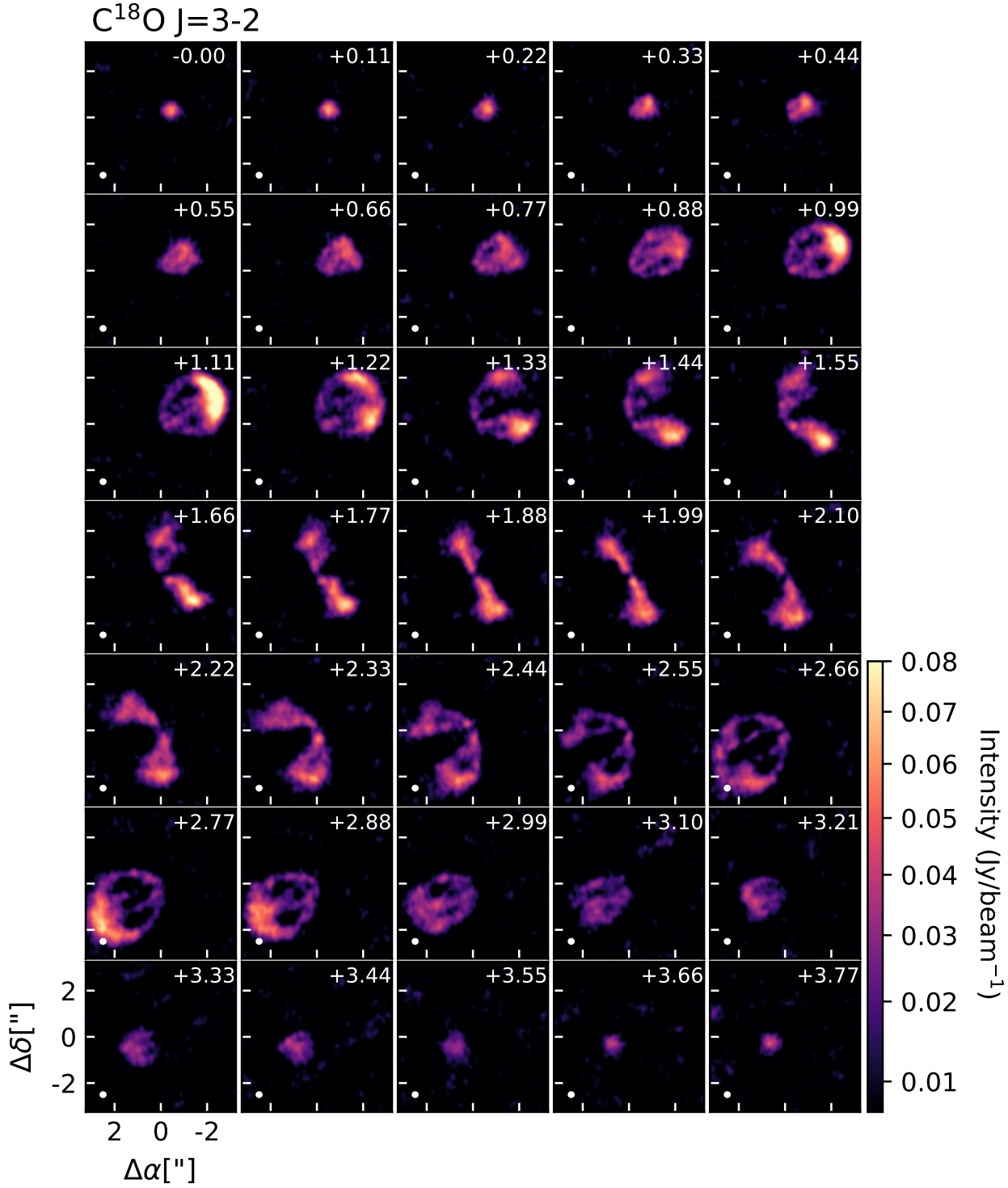


Figure 4.5: Individual emission of each channel for $C^{18}O$ isotopologue, corresponding velocities are written in the top right of each panel.

similar velocities as the disk on the East side. There is no clear velocity gradient between the large-scale emission and the disk in either isotopologue.

From here on, we focus on the channel maps that trace the disk rather than large-scale

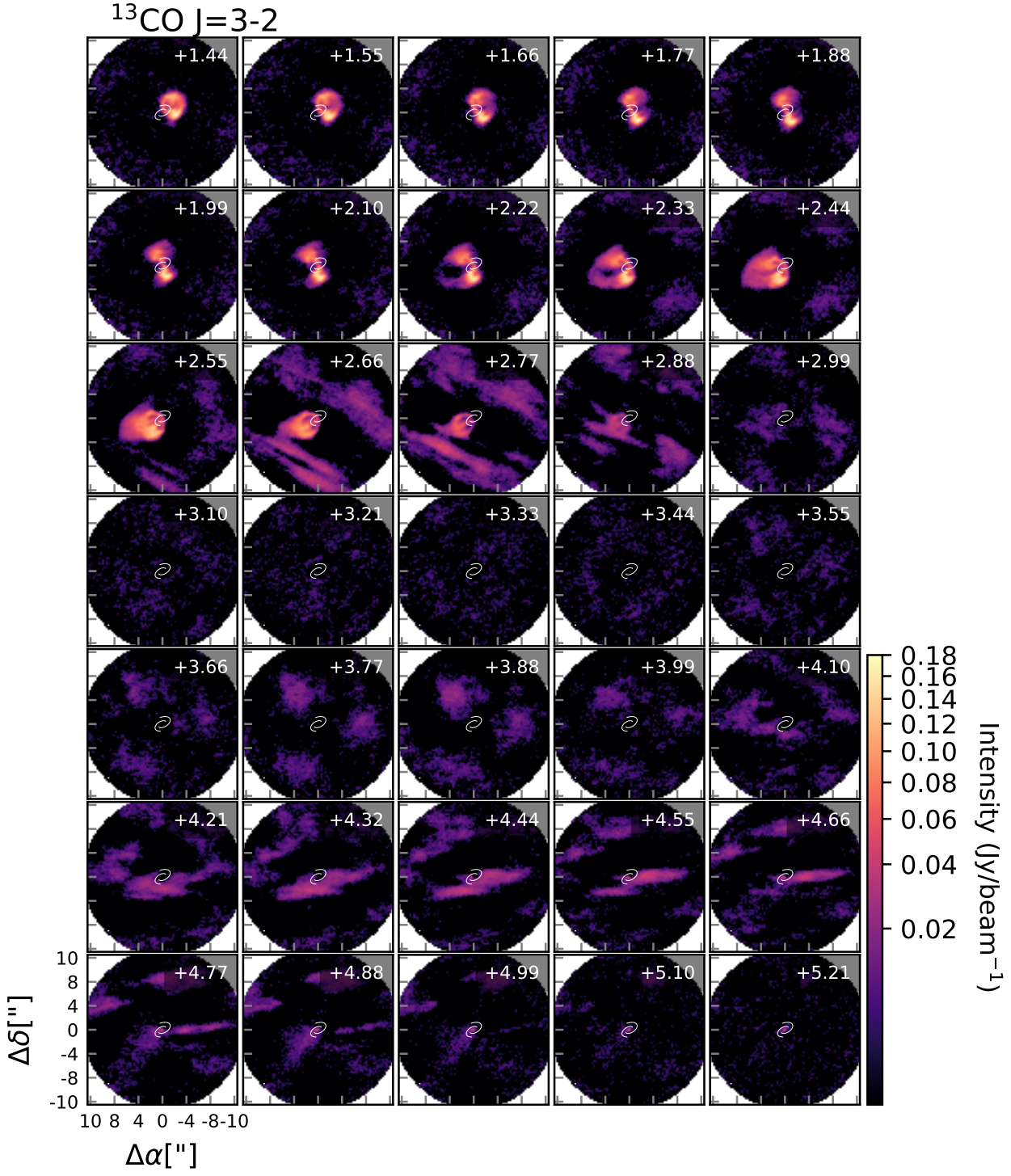


Figure 4.6: Individual emission of each channel for $^{13}$CO isotopologue, corresponding velocities are written in the top right of each panel. Channels correspond to velocities were large-scale emission is observed. Imaging enhances large-scale structure, parametric model of the spiral arms is plotted for reference.

emission or cloud contamination, which were obtained using uv-tapering and filtering of the short baselines as described in Chapter 2. Fig. 4.10 shows the integrated emission (moment

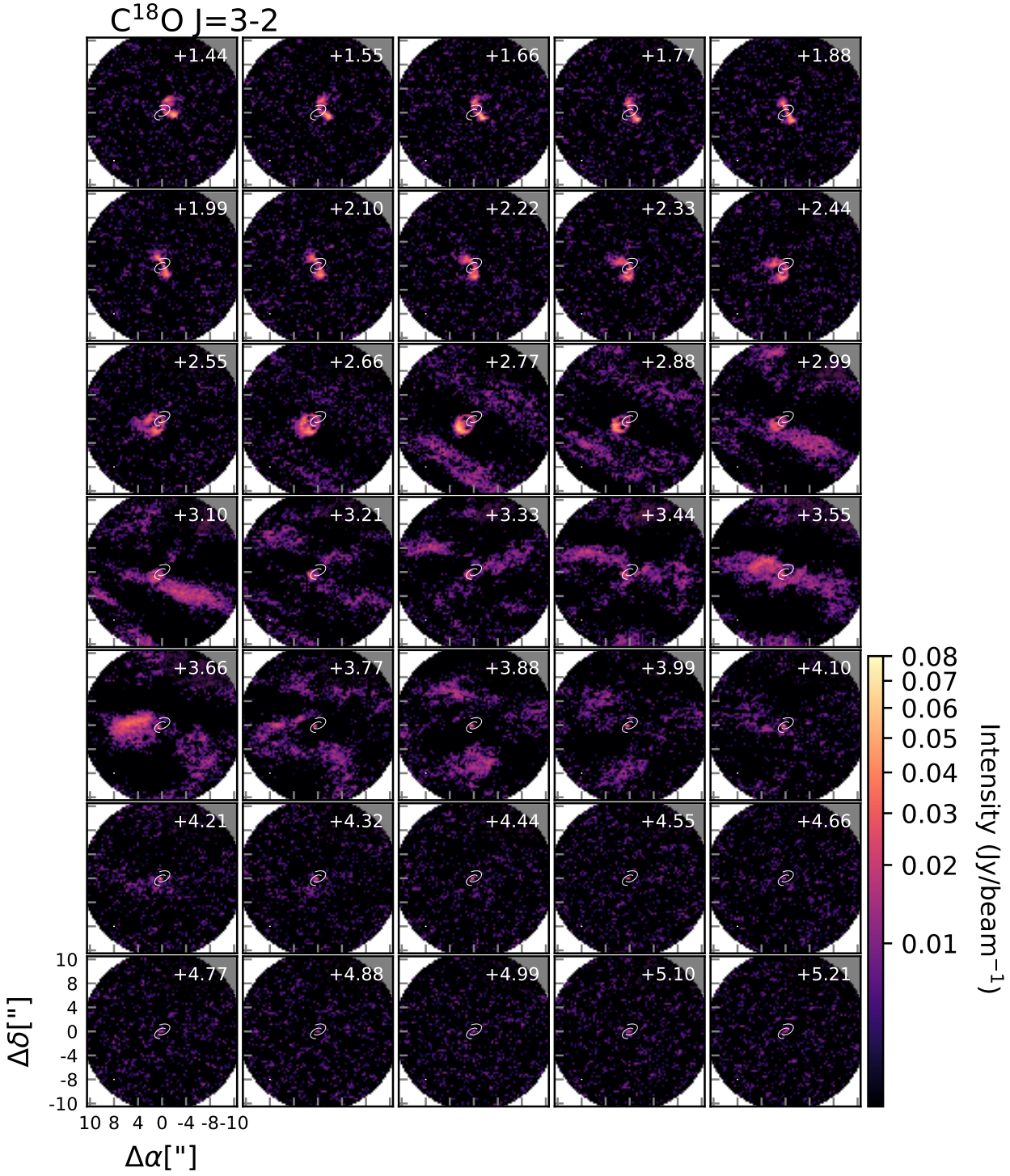


Figure 4.7: Individual emission of each channel for $C^{18}O$ isotopologue, corresponding velocities are written in the top right of each panel. Channels correspond to velocities were large-scale emission is observed. Imaging enhances large-scale structure, parametric model of the spiral arms is plotted for reference.

0) of both CO molecules, where foreground absorption in $^{13}CO$ is clear in the East side of the disk. Overlaying the continuum contours for the 0.89 mm emission and measuring along

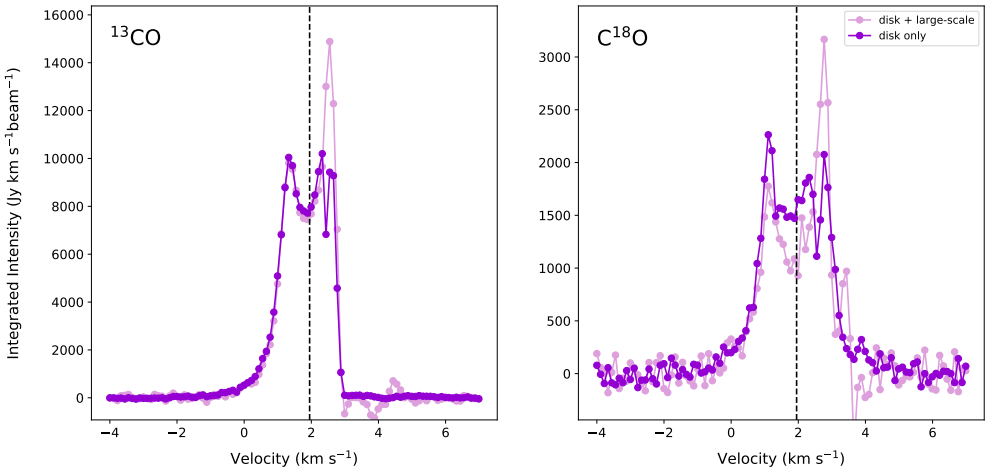


Figure 4.8: Integrated intensity at each imaged channel for C$^{18}$O and $^{13}$CO, with and without large-scale emission. Vertical line indicates systemic velocity (1.95km/s). Note difference between integrated emission scales.

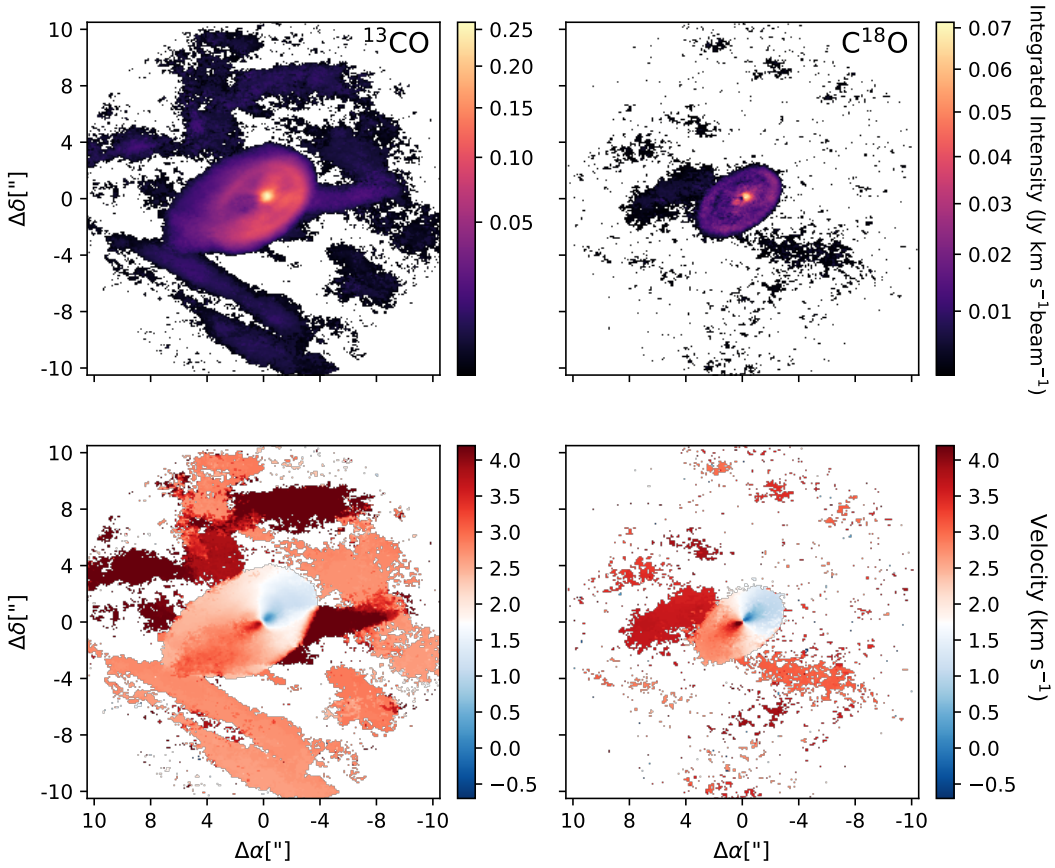


Figure 4.9: Left column shows $^{13}$CO emission maps, Right row C$^{18}$O emission maps. Top Row: Integrated emission maps considering all emission over $4\sigma$. Lower Row: Mean velocity maps.

the major axis, the East side of the disk appears to have a larger extent than the West side in the gas. Figure 4.10 shows that the size difference is roughly 0.5" between East and West sides of the disk, in both CO tracers. At the source distance, the size difference corresponds to 58au between the emission extent of each side.

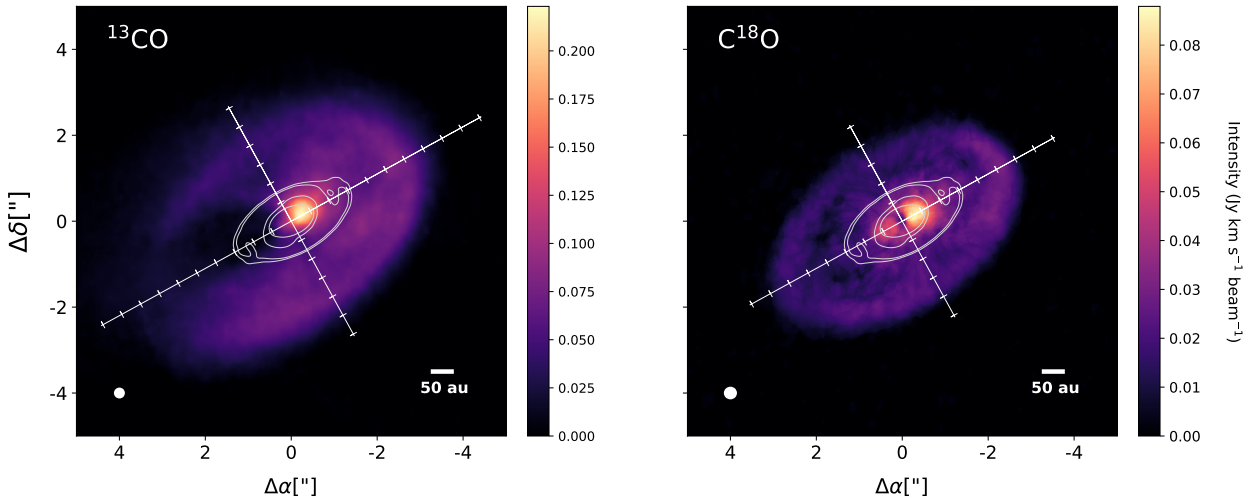


Figure 4.10: Integrated emission (moment 0) maps for $^{13}$CO (left) and C$^{18}$O (right) gas emission. Contours of 0.89mm continuum emission are overlaid on top. White grid marks the minor and major axis of the disk, as determined by the continuum emission position angle, ticks on these axis indicate 0.5" (∼58au) intervals.

To measure the East/West size differences observed, we trace the edge of the emission in the C$^{18}$O moment 0 map, down to the radius that encompasses 98 % of the integrated emission at each sampled azimuthal angle (red points on the top panel of Figure 4.11). We define the center based on the emission peak from the Band 7 continuum data and deproject accordingly, assuming the inclination and position angle of the dust continuum. The resulting deprojected radial distance as a function of azimuthal angle are shown in the middle panel of Figure 4.11, errors correspond to the astrometric error calculated as described in section 3.2. We see that the edge of the disk is not well described by a circle or an ellipse, it is perturbed and shows two local maxima and two local minima. The global minimum distance is located along the major axis on the West, but the global maximum distance is shifted with respect to the East major axis. The locations of maximum and minimum border extents are not colocated with the continuum spiral features, or their extension. Another recognizable feature in the moment 0 map is the presence of a "gap" of emission at large disk radii in C$^{18}$O. To estimate its location, we trace the radial positions of emission minima sampling every 9°, between 185-300au (this range is determined by analysis of the intensity profile). Using the mean value and standard deviation of the minima radial locations (yellow points in top panel of Fig. 4.11), we estimate the gap position at 241 ± 24 au.

We locate the strongest foreground absorption in the $^{13}$CO integrated intensity map between ∼25°-155° (angle is measured North towards East). Excluding this azimuthal area, we may find a subtle decrease in emission, considering an azimuthal range between −205°-20°, at radial distances between ∼90au-250au, the analysis is shown in Figure 4.12. If we plot the minimum emission location and the dust spirals, as described by the best-fit parametric

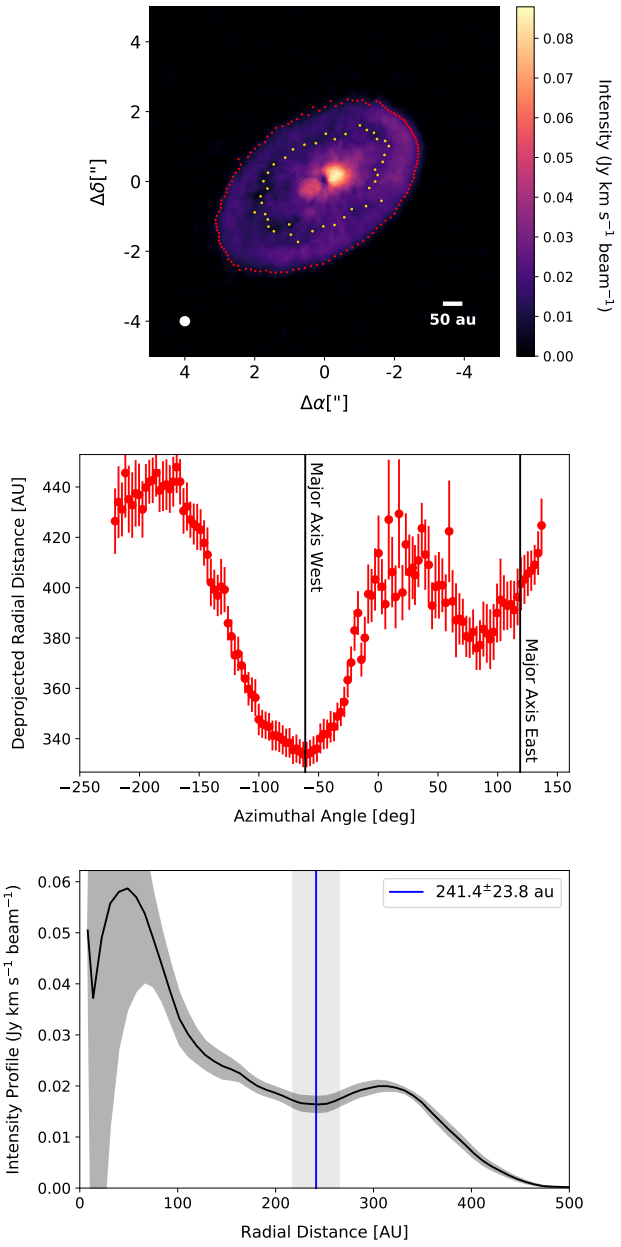


Figure 4.11: Top Panel: Integrated emission map of the $C^{18}O$ gas emission, yellow dots trace local minimum of emission, red circles trace the disk radial extent as the location at which 98 % of the total azimuthal emission is included. Middle Panel: Radial distance from the center of the points tracing the border, azimuthal angle is measured from the North, to the East (left). Bottom Panel: Azimuthally averaged intensity profile of the $C^{18}O$ emission, shaded area shows the $1\sigma$ scatter at each radial bin divided by the beams spanning the angles over which the intensities are measured, vertical blue line marks the average radial location of the minimum of emission and the deviation of the data is indicated by the vertical grey region.

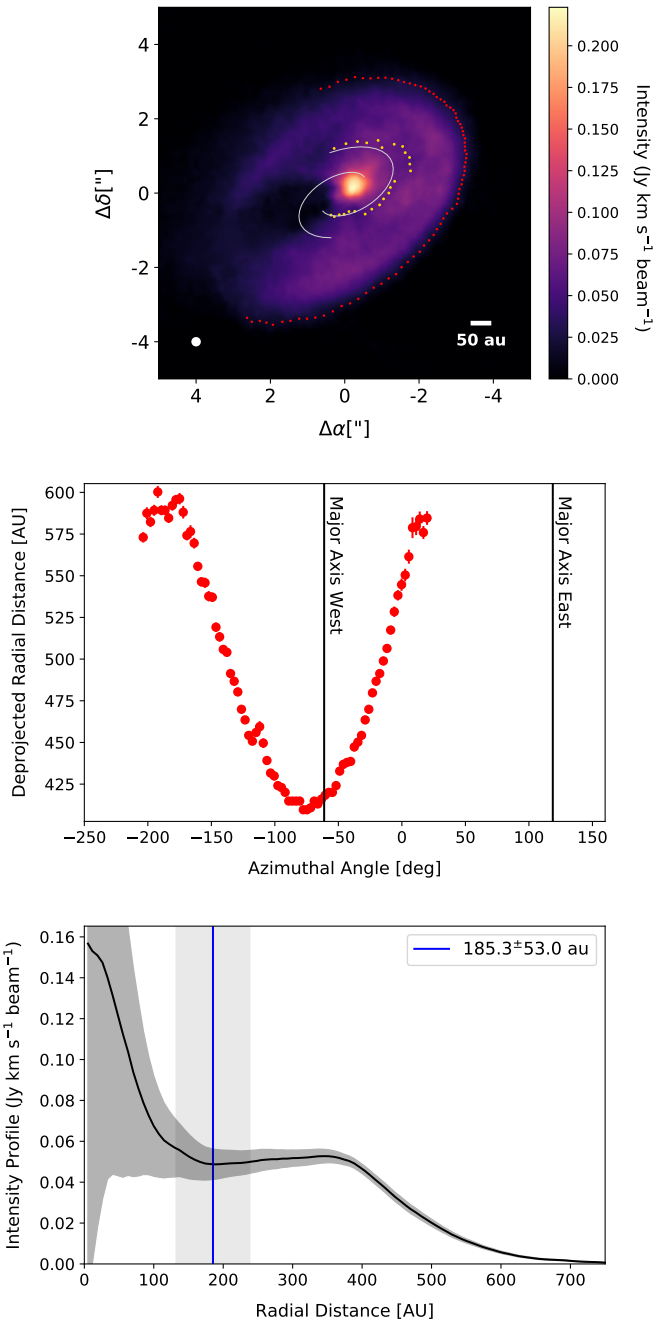


Figure 4.12: Same as Figure 4.11, for the $^{13}$CO gas emission. Emission is only considered between −205°-20° (angle is measured North towards East). Spirals in top panel show best-fit parametric model from 0.89mm dust emission, for reference.

model derived previously, we find relative agreement between the NW spiral and the minimum location data points. Furthermore, the deprojection of the radial distances of the found minimum emission locations confirm that we are not tracing an ellipsoidal shape, as in the case of C$^{18}$O. For reference, even though the emission does not trace an ellipse and is not characterized as a gap, the mean location of the emission minima and the standard deviation of the distances are shown in the azimuthally averaged intensity profile, obtained considering

only the sampled azimuthal range. If we trace the emission border following the 98 % integrated emission criteria, same as with the $C^{18}O$ data, we recover a similar emission border curve. We note that for azimuthal angles larger than 0° the $C^{18}O$ border shows variations from which we measure the secondary maxima and minima, at ∼17° and ∼82° respectively (Figure 4.11), however the $^{13}CO$ emission can only accurately have its border traced up to ∼20° and in the sampled azimuthal range displays only one recognizable minima (roughly colocated with the global minimum radial distance in $C^{18}O$, along West major axis).

## 4.3. Tracing the emitting layer in $^{13}CO$ and $C^{18}O$

To analyze the size difference observed in the integrated emission maps and study the overall gas distribution, we use the method detailed in Pinte et al. (2018a), which recovers the height and velocity of the emitting gas layers by directly tracing the emission from the channel maps and applying geometrical relationships. This method consists in tracing the emission maxima of each channel, which should indicate the isovelocity curve, along the rotated "top" layer (rotated so that the mayor axis is horizontal, aligned with the x axis, in the image plane). Assuming a symmetric distribution with respect to the semi major axis, we may consider that each side, "far" and "near", of the "top" layer is related point by point with position ellipses that fall on the gas emission layer, this is diagramed in Figure 4.13. The assumption of axi-symmetry is a fundamental argument for this approach, as we assume that the emission from symmetric positions with respect to the semi-major axis come from a same emmiting height (see Figure 4.13).

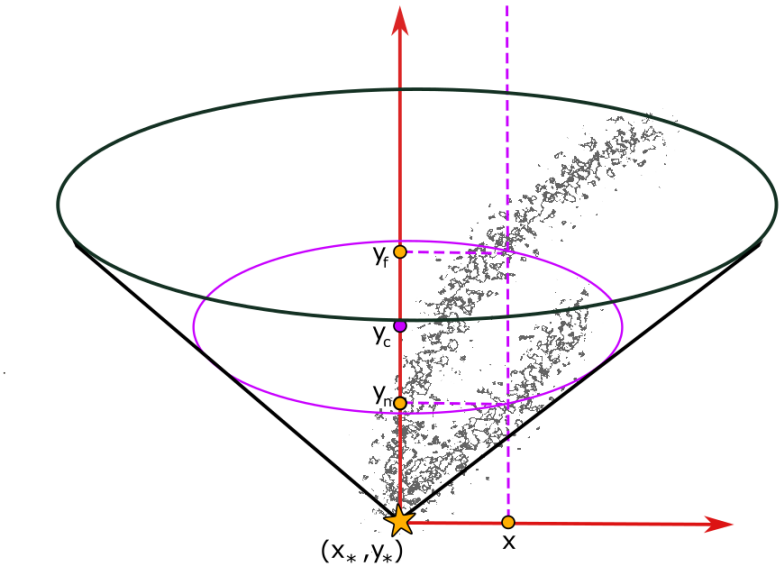


Figure 4.13: Schematic to illustrate the geometrical relations done to derive and trace the gas location.

The key coordinates in this method are $(x_*, y_*)$, which correspond to the star coordinates,

determined by the peak of the continuum map and $(x_f, y_f)$, $(x_n, y_n)$ corresponding to the maxima emission coordinates of the near and far sides of the top layer, respectively. To recover the height of the emission from the continuum midplane, each maxima position is compared to its respective pair on the other side at the same $x$ position, so that $x = x_f = x_n$. As the gas is vertically pressure supported at any point in the disc, we may consider that it is rotating on a circular orbit parallel to the disk midplane. The relation between the coordinates of the isovelocity curve, in near and far sides, with the coordinates of the the centre of the projected circular orbit passing through those two points, $(x_c, y_c)$, is $x_c = x_*$ and $y_c = (y_f + y_n)/2$. The radius $r$ and altitude $h$ of this orbit can be calculated based on the previously obtained coordinates and the disk inclination angle $i$, as follows:

$$r = \sqrt{(x - x_c)^2 + \left(\frac{y_f - y_c}{cos(i)}\right)^2} \tag{4.1}$$

$$h = \frac{y_c - y_*}{sin(i)} \tag{4.2}$$

From all available channels, we select those in which the top layer of gas emission can be clearly identified, so that we are able to trace the maxima along this layer for the analysis. For $C^{18}O$ we select channels corresponding to velocities +0.77 to +1.55 km s$^{-1}$ and +2.44 to +3.21 km s$^{-1}$. For $^{13}CO$ we select channels +0.66 to +1.66 km s$^{-1}$ and +2.33 to +2.77 km s$^{-1}$. The top layer is only traced at the locations were it is clearly differentiated from the rest of the emission, Figures 4.14 and 4.15 show the traced emission for $^{13}CO$ and $C^{18}O$, respectively. The data points do not trace very close to the center or to the outermost emission.

The recovered height profile from the midplane of the emission layer for both gas isotopologues is shown in Figure 4.16. Measurements obtained from channels that trace emission from the East sides of the disk (with respect to the semi-minor axis) are colored red, while those from the West are colored blue. The $C^{18}O$ and $^{13}CO$ gas emission layer we constrain follows the expected distribution for these isotopologues in a disk: $^{13}CO$ traces a higher layer from the mid-plane than $C^{18}O$, in both East and West sides at all radii. The continuum and $C^{18}O$ gas gap location are highlighted in Fig. 4.16, together with the width for the dust gap (as reported in Huang et al., 2018b) and the uncertainty region found for the gas gap. No clear feature is recovered in the gas height profile at the gap locations, however we note that the scale height in the West channels begins to decrease close to the gap.

The height distribution is modelled using the equations for a complex flared surface presented in the EDDY package (Teague, 2019), where the altitude of the emitting layer follows a double power-law:

$$z(r) = z_0 \left(\frac{r}{r_0}\right)^{\psi} + z_1 \left(\frac{r}{r_0}\right)^{\varphi}, \tag{4.3}$$

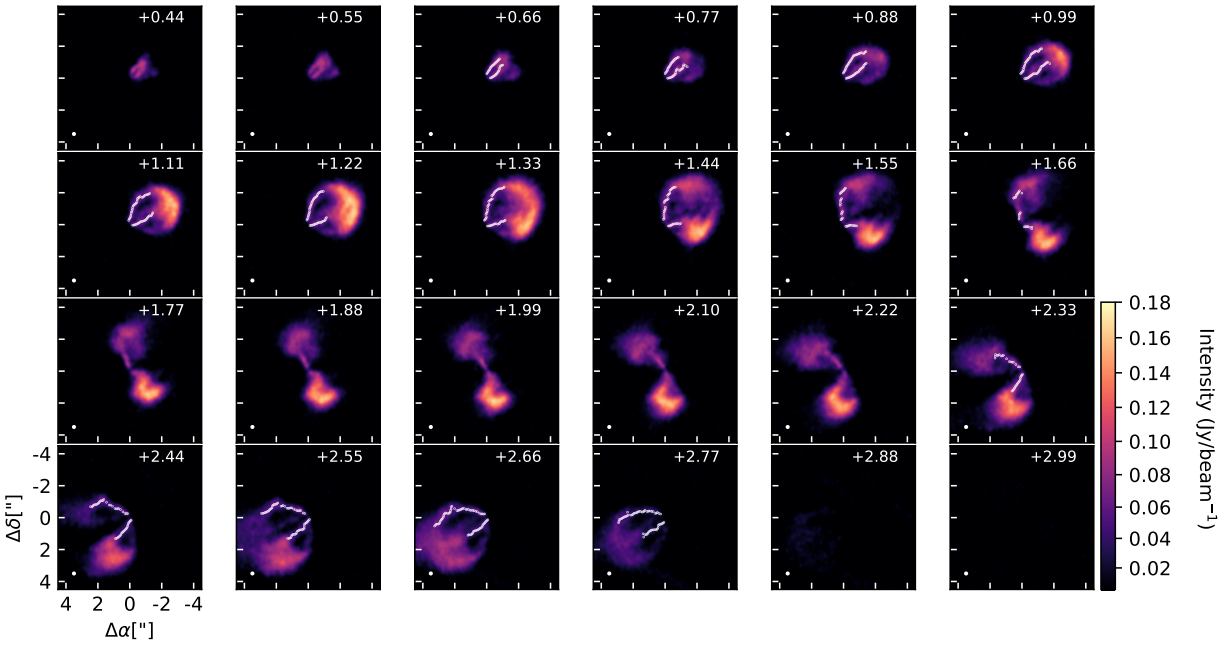


Figure 4.14: $^{13}$CO channel maps showing the selected channels for tracing the emitting surface. White marks correspond to the traced upper layer of the emitting surface.

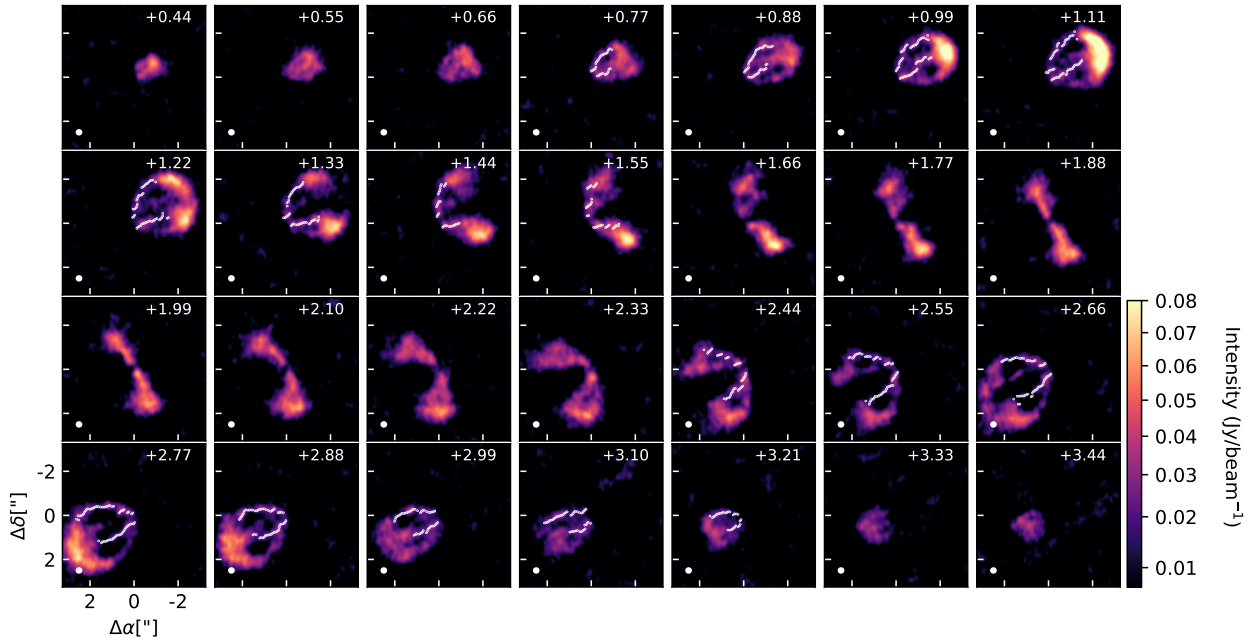


Figure 4.15: C$^{18}$O channel maps showing the selected channels for tracing the emitting surface. White marks correspond to the traced upper layer of the emitting surface.

where $r$ is the radial distance from the star, as measured in cylindrical coordinates (in the azimuth plane), and the characteristic radius $r_0$ is fixed at 1", corresponding to 115.88au for our system. The second power-law is aimed to be a correction on the first term, therefore we

first find the best set of parameters for the emission layer characterized with a single power-law and then optimize close to those parameters, to include the second power-law. The best fit parameters of the model are assumed to be the median value from the posteriors of the MCMC chains and are shown with their uncertainties (16th and 84th percentile uncertainties derived from the posteriors) in Table 4.1.

Table 4.1: Height model parameters from Channel analysis

| Param. | $^{13}$CO − W | $^{13}$CO − E | C$^{18}$O − W | C$^{18}$O − E |
|---|---|---|---|---|
| $z_0$ [au] | $56.6^{+1.9}_{-3.0}$ | $38.3^{+5.4}_{-9.5}$ | $36.2 \pm 0.9$ | $26.8^{+6.4}_{-10.8}$ |
| $\psi$ | $1.64^{+0.02}_{-0.08}$ | $0.87^{+0.28}_{-0.04}$ | $1.96^{+0.03}_{-0.04}$ | $1.20^{+0.8}_{-0.1}$ |
| $z_1$ [au] | $-17.1^{+2.9}_{-1.8}$ | $-9.0^{+8.9}_{-5.4}$ | $-4.2 \pm 0.7$ | $25.1^{+9.8}_{-6.3}$ |
| $\varphi$ | $2.55^{+0.08}_{-0.05}$ | $0.27^{+4.7}_{-0.20}$ | $4.25^{+0.16}_{-0.13}$ | $1.04^{+4.1}_{-0.2}$ |

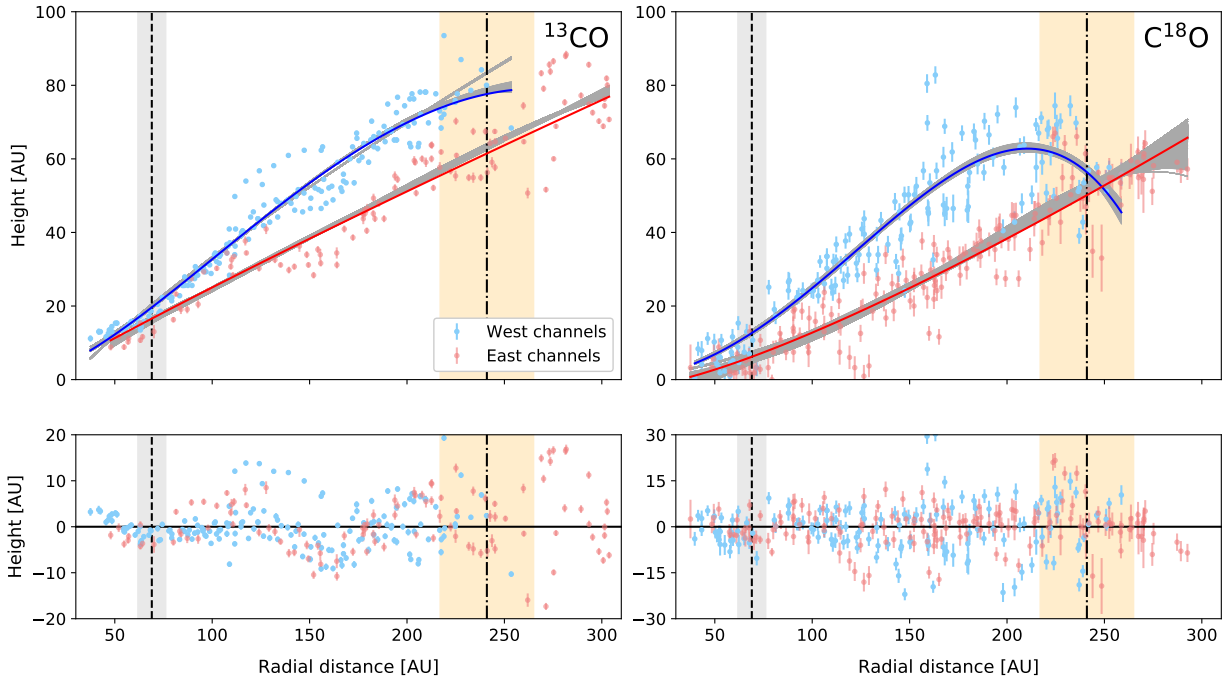


Figure 4.16: Top panels show the emission layer height as a function of radial distance to the star constrained from the C$^{18}$O (left) and $^{13}$CO (right) data. Blue points correspond to measurements coming from the West side of the disk, red points come from the East side, colored line corresponds to the best-fit double power law height profile for the data, grey profiles show the posterior distribution of the double power law fit. Vertical dashed line indicates the location of the gap reported in the continuum, dot-dashed line correspond to the gap location in the C$^{18}$O integrated intensity map. Grey area indicates the width of the dust gap (obtained from Huang et al. (2018b)), orange area indicates the gas gap's location uncertainty. Bottom panels show the residuals of each isotopologue after subtracting the best-fit model to the data.

Our modelled emission surface presents several perturbations with a consistent difference in the elevation and form between the East and West sides of the disk. These emission profiles have a quasi-linear form in the East channels, mostly tracing lower scale height values than the West channels, however, at larger radii (>200 au), the West channels show a clear decrease in the scale height. Residuals obtained from subtracting the model to the observations are shown in the bottom panels of Figure 4.16, from here we can see that the largest residual scatter is found between both gap locations, which roughly coincides with the radial extent of the dust spiral arms (80-250au). The residuals from the $^{13}$CO emission show a clear "curved" pattern in both sides, indicating a more complex emitting surface, this is not detected in the C$^{18}$O. The amplitude of the residuals is larger in the C$^{18}$O emission and we note that in both isotopologues the residuals at the dust gap location are negative, indicating a possible decrease in the emitting surface at this radii, however this is unresolved with our spatial resolution.

## 4.4. Tracing the kinematics in $^{13}$CO and C$^{18}$O

Besides tracing the height location of the emitting layer, Pinte et al.'s method allows us to determine the velocity of the traced gas emission layer. In a given velocity channel, we know the projected radial velocity, $v_{obs}$, together with the systemic velocity for the source, $v_{syst}$. Using the inclination angle $i$ and the polar azimuthal angle $\theta$, we can relate both velocities through $v_{obs} = v_{syst} + vcos(\theta)sin(i)$. Here it is assumed that the velocity component is purely azimuthal and $v$ is the actual azimuthal velocity around the star. Noting that $cos(\theta) = (x - x_*)/r$, with $r$ previously obtained (eq. 4.1), the actual gas velocity around the star, at the height location, may be calculated as:

$$v = (v_{obs} - v_{syst})\frac{r}{(x - x_*)sin(i)} \tag{4.4}$$

Measuring the velocity profile will allow us to obtain a mass estimate for the central star and also test for super-Keplerian velocities at large radial distances, which is a characteristic expected in disks undergoing GI (Bertin and Lodato, 1999; Lodato, 2007). Assuming a systemic velocity $v_{sys} = 1.95$km s$^{-1}$, consistent with our channel maps observations and previous estimates (Pérez et al., 2016; Huang et al., 2018c), we constrain the velocity profile of the emitting gas for both $^{13}$CO and C$^{18}$O, shown in Fig. 4.17. An overall velocity difference is observed between both sides of the disk, with measurements from the East side having a higher velocity. From our previous results (Fig. 4.16) we know that the East side corresponds to the side apparently closest to the midplane. The difference in the velocity profile is in agreement with the height profile variations between sides, as being closer to the midplane would result in larger velocities. We do not observe any peculiar velocity behavior at the location of dust and gas gaps.

We model the velocity profiles with a keplerian model to constrain the mass of the central star, which has been reported to be $\sim$0.49M$_\odot$ (Andrews et al., 2009, 2018a; Pérez et al., 2016). To do this, we incorporate the height distribution of each molecule, using the best fit

double power-law model found previously (see Table 4.1). The modelled velocity at radial distance $r$ from the star will follow equation 4.5, where $G$ is the gravitational constant, $M_*$ is the central star mass, and $h$ is the height of the gas at radius $r$:

$$\frac{v^2}{r} = \frac{GM_* r}{(r^2 + h^2)^{\frac{3}{2}}} \tag{4.5}$$

We note that equation 4.5 does not include the effects of the radial pressure gradient and the disk's self-gravity (Rosenfeld et al., 2013). As both the gas temperature and density tend to decrease with radial distance, the negative pressure gradient causes the gas to slow down and orbit at sub-Keplerian velocities, on the other hand, the mass contributed by the disk should increase the gas velocity to super-Keplerian speeds at large radii (Rosenfeld et al., 2013).

We simultaneously fit the model to the data points from both East and West sides of the disk in each isotopologue, using MCMC chains and taking into account their different height profiles (Fig. 4.16). Figure 4.17 shows the velocity of the emission layer for each isotopologue, as measured for the East and West sides of the disk, with best-fit curves of their expected Keplerian motion given the best-fit stellar mass and its $1\sigma$ uncertainty range. The final masses and errors are computed from the median value and 16th and 84th percentile uncertainties derived from the posteriors. From the $^{13}$CO measurements we constrain a stellar mass of $M_* = 0.5^{+0.05}_{-0.04}$ M$_\odot$, while from the C$^{18}$O measurements we constrain $M_* = 0.49^{+0.15}_{-0.17}$ M$_\odot$. Both values are in agreement between them and with previous estimates.

Compared to the expected Keplerian velocity profile, the West channels show a consistently sub-Keplerian velocity, pronounced near 100 au in $^{13}$CO and over the whole radial extent in C$^{18}$O, where seemingly super-Keplerian velocities from the East channels are observed, pronounced near 100 au in C$^{18}$O. These sub- and super-Keplerian velocities could be explained if the emission layer height difference between the East and West sides was actually higher than what was constrained from the analysis of Figure 4.16. The lack of residuals indicating super-Keplerian velocities at large radii, where we would expect deviations in the order of 20-30 %, given the large estimated disk-to-star mass ratio, is contrary to the predictions for a GI disk (Bertin and Lodato, 1999; Lodato, 2007), this will be further analyzed in the Chapter 7.

Finally, we use the constrained emission surface of each side of the disk, and a stellar mass value of 0.49M$_\odot$, to build a model of the expected mean velocity maps of each isotopologue and compare it to the observations. Our model velocity map considers only the Keplerian motion of the upper layer of the emission surface, however, in the case of Elias 2-27, the disk is inclined such that emission from the lower layer appears in the southern part of the disk (Huang et al., 2018c), which may be cause for larger residuals at across this location. Additionally, our constrains on the shape of the emission surface do not cover the whole radial extent of emission, and are extracted from the data retrieved at radial distances between ∼40-300au (∼0.35" - 3.59") from the central star (see Fig. 4.16). Therefore, we should also expect to have larger residuals in the inner and outer regions where the emitting surface is not directly constrained by our method describe above.

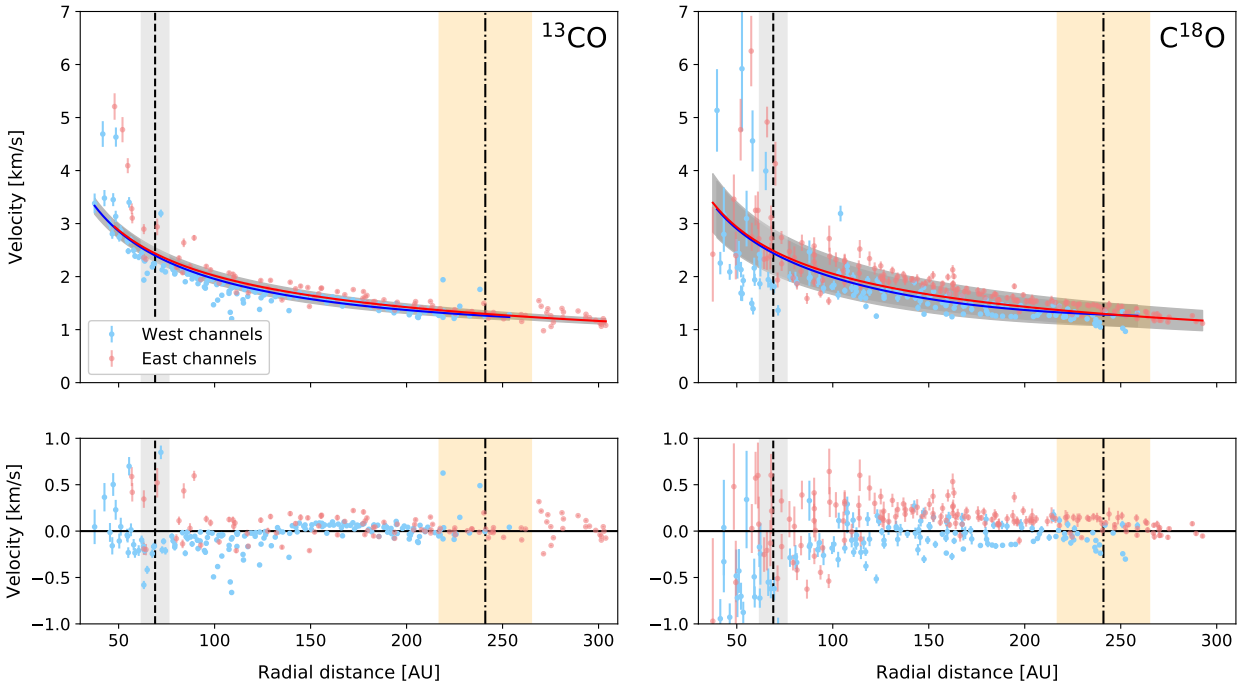


Figure 4.17: Top panels show the data tracing the velocity of the gas emission, as a function of radial distance to the star, from the C$^{18}$O (left) and $^{13}$CO (right) isotopologues. Blue points correspond to measurements coming from the West side of the disk, red points come from the East side, plotted curves correspond to the best-fit Keplerian rotation profile and shaded area corresponds to the stellar mass uncertainty as indicated by the 16th and 84th percentiles of the posteriors. Vertical dashed line indicates the location of the gap reported in the continuum, dot-dashed line correspond to the gap location in the C$^{18}$O integrated intensity map. Grey area indicates the width of the dust gap (obtained from Huang et al. (2018b)), orange area indicates the gas gap's location uncertainty. Bottom panels show the residuals of each isotopologue after subtracting the best-fit model to the data.

Figure 4.18 shows the $^{13}$CO and C$^{18}$O velocity maps in top and bottom rows, with observations, model, and residual velocity maps in left, middle, and right columns. The integrated velocity maps are computed using the BETTERMOMENTS package (Teague and Foreman-Mackey, 2019), to accurately constrain the line of sight velocity from the channel maps with 0.111km s$^{-1}$ spectral resolution. Initial analysis of the observations allows us to identify marked perturbations throughout the disk, especially along the South and the West, where a distinct "wavy" pattern is observed in the outer disk. Along the major axis the C$^{18}$O data also displays "wavy" perturbations in a seemingly perpendicular form with respect to the azimuthal Southern "wavy" pattern. In the model maps, which are calculated using the functions from EDDY (Teague, 2019), with the input of our constrained emission surface for each side, we see that the West side of the disk is able to reproduce to some extent the "wavy" pattern along the South of the disk in both isotopologues, thanks to the change in scale height for the West in the outer disk. We do not see this pattern in the East side of the model map, as the emitting surface retrieved, for the sampled radial distances, does not present large

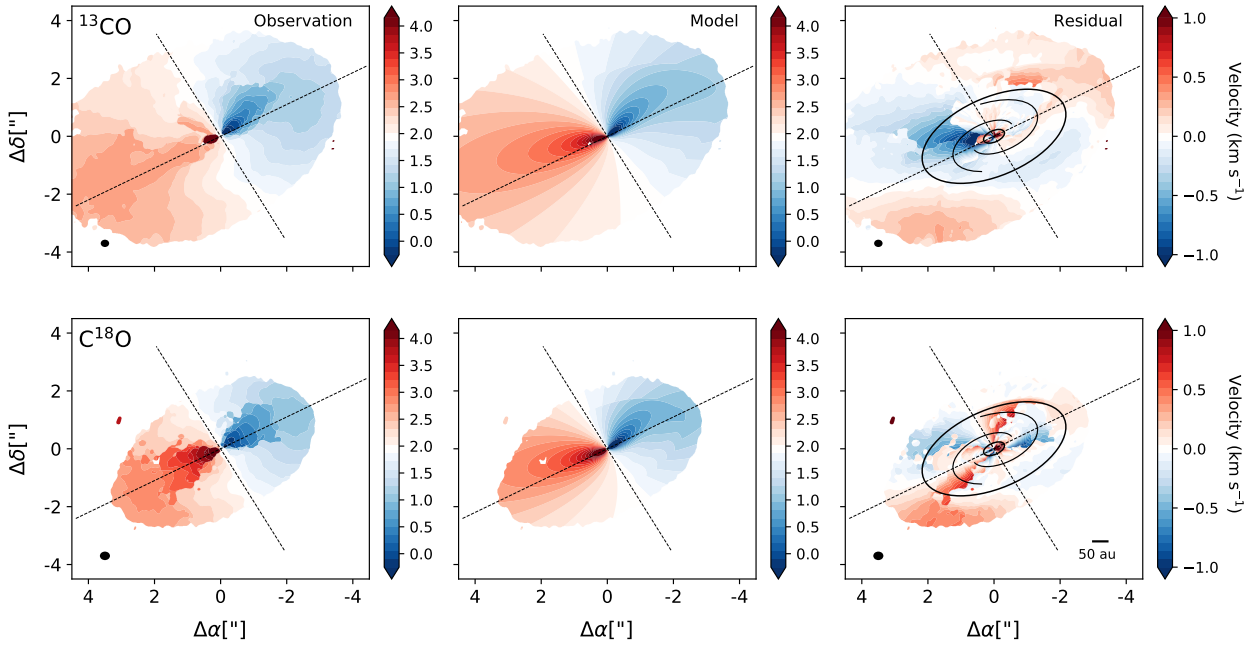


Figure 4.18: Top row shows $^{13}$CO emission , Bottom row corresponds to C$^{18}$O emission. In each row, the first column shows the integrated emission velocity map (moment 1) from the observational data. Second column shows the velocity map model, computed using the constrains found for the emission surface and stellar mass. Third row shows the residuals calculated by substracting the model map to the observations, spiral arms show best fit parametric model from the 0.89mm dust emission, inner and outer ellipses indicate radial limits for the data used to derive the geometrical constrains on the emission surface geometry and stellar mass values.

deviations from a linear model.

In the residuals, the radial extent that was used for determining the emission layer model is marked as two ellipses to define inner and outer radial bounds (40-275au). It is apparent that, for larger radial distances than what was sampled, the residuals in the West side of the disk are close to zero and much lower than the residuals from the East side, in both isotopologues. The latter means that the modelled West side emission layer with a "dip" in the scale height at larger distances from the star is valid when extending the model to larger radii. Indeed, if we try to model the emitting surface with a cone-like or single power law emission model (so the scale height will continue to grow at large radii) the West side displays residuals with the same colour pattern as the East side, but inverted between North and South side (positive in the North, negative in the South). This is a possible indicator that the East side of the disk also presents a decrease in the scale-height at larger radial distances, but given our small range of sampled radial distances, we may not have been sensitive to this "turning point" in the East. Within our sampled radii, marked by the ellipses, we observe negative residuals in the North-East quadrant of the $^{13}$CO emission, which roughly coincide with the location of the most prominent cloud absorption (see Figure 4.10), so we associate these residuals with the absorption. The C$^{18}$O residuals within the ellipses are much stronger

and display a rough "X" shape across the center, with marked positive residuals close to minor and major axis' in North-West and South-East quadrants, respectively. As was noted, the radial distances within the ellipses coincide with the radial extension of the dust spiral arms, while the "X" shape does not have a clear co-location with the spiral structure, the largest positive residuals coincide with the location where a spiral starts and the other ends. This "X" shaped residual probably traces perturbations arising from the mid-plane, as it is not observed in $^{13}$CO and the C$^{18}$O emission traces a lower height layer.

We also attempt to directly reconstruct the emission layer from the observed velocity map, using the EDDY package (Teague, 2019) and fitting a symmetric 3D emission surface to the velocity map, from a parametric model. When trying to recover the emission layer of $^{13}$CO and C$^{18}$O from the velocity maps presented in Fig. 4.18, the results from EDDY prefer a geometrically thin disk rather than a cone-like or flared emission surface. However, such a flat disk leaves larger residuals, than those in Figure 4.18, and it cannot reproduce the elevated emission surface in both isotopologues that we clearly distinguish across many channels (see Figures 4.5 and 4.4). Approaches using the EDDY functions but separating between sides and using our constrains on the emission surface as initial guesses for the optimization lead to a drop in the emission surface at larger radial distances in the East side, as expected from our previous analysis.

## 4.5. Features in the channel maps of C$^{18}$O and $^{13}$CO

In the CO channel maps (see Figures 4.5 and 4.4) we observe several perturbations, which don't follow the expected Keplerian velocity field and which we refer to as "kinks". In the following figures, we overlay several previously characterized features of Elias 2-27 to use as reference: the continuum spirals and their extension, the location of the dust continuum and C$^{18}$O gaps, as well as the expected iso-velocity curves (following the derived emission layer in section 4.3) for those channel maps where we highlight deviations from Keplerian motion. We observe two types of perturbations: inner kinks at roughly the location of the spiral arms (but outside the dust gap at $\sim$ 70 au), and outer kinks, beyond the extent of the continuum emission at $\sim$ 250 au.

Perturbations are strongly present in the central velocity channels of both CO tracers, as shown in Figure 4.19. We observe an inner kink (marked with a yellow arrow, Fig. 4.19) close to the spiral in the south side of the disk and along several channels, it appears strongest at channels +1.77 to +1.55 km s$^{-1}$. This feature is co-located with the NW spiral. A large outer "C" shape (marked with a green arrow, Fig. 4.19) can be seen beyond the gas gap in the south where the emission is brightest. This "C" shape feature is strongest in $^{13}$CO, along channels 1.55-2.33 km s$^{-1}$, but in channels 1.66-1.88 km s$^{-1}$ of C$^{18}$O we can also recognize it in the southern part of the disk. We suggest that the "C" is not a deviation from keplerian motion, but rather is the projected emission from the upper and lower sides of the disk in these channels.

Besides these features located near the disk systemic velocity, we see more subtle deviations in high velocity channels, for both East and West sides of the disk in the C$^{18}$O channel maps.

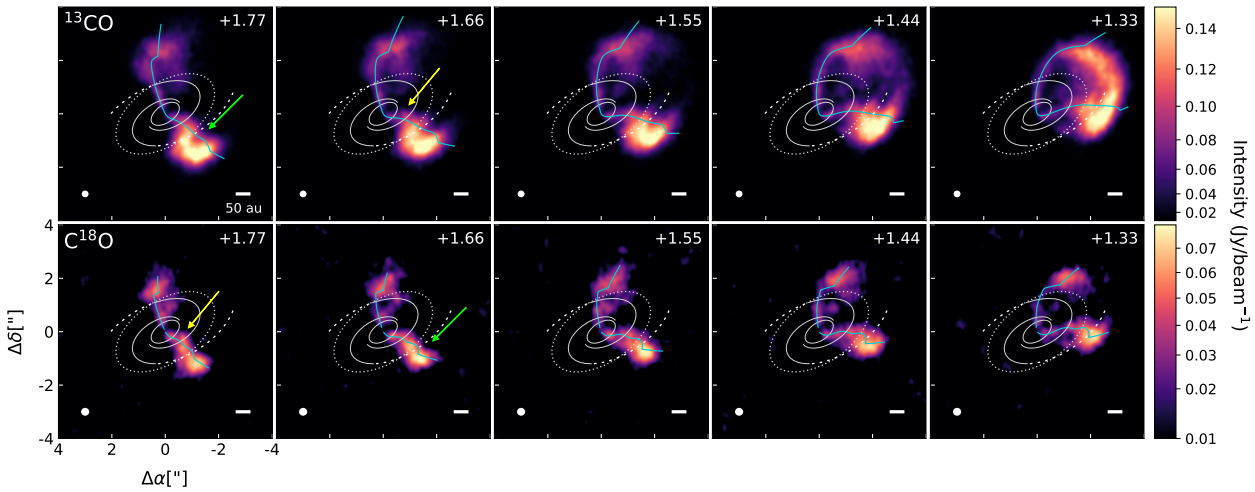


Figure 4.19: Selected central channels of $C^{18}O$ (top) and $^{13}CO$ emission (bottom). White continuous line shows the dust features: inner gap at 69au and the spirals as traced from the 0.89 continuum emission. Dotted white line traces the $C^{18}O$ gas gap location at 241au. Dashed lines show how the spirals traced in the dust would extend further outside of the continuum emission. Blue curve traces the expected isovelocity curve of each channel, following the constrained emission layer geometry of the top layer. The velocity of each channel map is indicated in top-right corner of each panel, the beam size is in the bottom-left corner. Green arrows mark the outer perturbation, yellow arrows mark the inner perturbation.

To highlight these perturbations, we show the expected isovelocity curves for these high velocity channels, along with the dust spirals in Figure 4.20. The top and bottom panels of Figure 4.20 show the West and East $C^{18}O$ emission, imaged with finer spectral resolution that is available only for the $C^{18}O$ data. The deviations are most visible at 0.95-1.0 km s$^{-1}$ in the West, where the top layer of the disk emission does not precisely follow the iso-velocity curve (blue line) and appears perturbed at the spiral arm location. In the East side, at 2.95-2.90 km s$^{-1}$, similar deviations are apparent in the top emission layer of the disk, roughly co-located with the SE spiral. These subtle kinks are not clearly observed in the $^{13}CO$ maps, however it is expected that perturbations due to the spirals should be more apparent in $C^{18}O$ than in $^{13}CO$, as the $C^{18}O$ traces a layer closer to the midplane, were the spirals reside. The deviations are better discerned in the West channels, possibly due to the lack of cloud absorption at these velocities, but also because, if the kinks are caused by the spiral arms, the highest-contrast spiral is in the West side of the disk.

We measure the velocity deviation by selecting the channel where we see the largest perturbation in both isotopologues and comparing the expected isovelocity curve to velocity variations that reach the location of the perturbations. We select channel corresponding to velocity +1.77 km/s in the channel maps, however we will analyze the Keplerian motion, therefore we are interested in the absolute Keplerian velocity which is -0.18km/s (system velocity is 1.95km/s). The expected isovelocity curve is overlayed on the channel emission and we determine that to trace the inner kink, a deviation from the isovelocity curve of

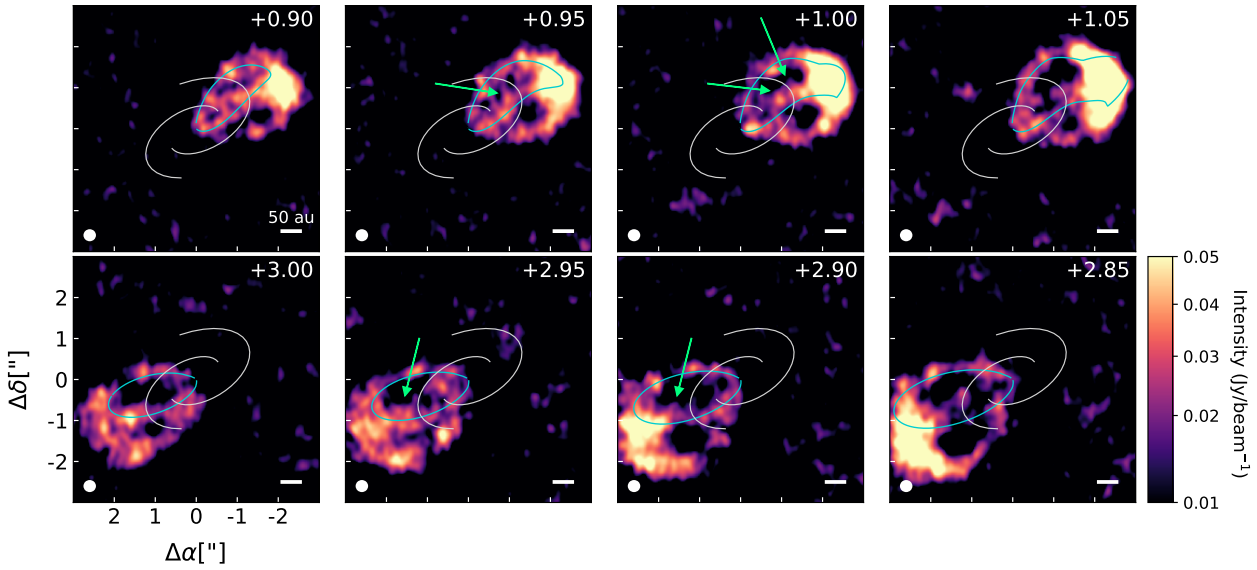


Figure 4.20: Selected high-velocity channels of $C^{18}O$ emission. White lines trace the spirals detected in the 0.89mm continuum emission, blue lines indicate the isovelocity curves expected at each channel velocity, indicated in top right corner of each panel, following the constrained emission layer geometry of the top layer. Arrows indicate were deviations from expected isovelocity curves ("kinks") are observed.

60 % and 80 % is required for $^{13}CO$ and $C^{18}O$ emissions, respectively. If treated as a kink, the "C" shape is stronger in the $^{13}CO$, where the deviation is 90 % from expected Keplerian motion, while in $C^{18}O$ the deviation is 70 %. The analysis is shown in Figure 4.21. The percentual estimations are rough visual estimates, not absolute values, but they indicate the expected magnitude of the perturbations. We note that the width of individual channel maps is 0.11km/s and our deviations range between 0.11-0.14 km/s.

As previously discussed, Pinte et al. (2020) reported the presence of a kink in the Northern side of Elias 2-27, at the location of the dust gap, which was signaled as possible indicator of a planetary companion (see figure 4.3). We do not recover this feature given our lower spatial resolution: DSHARP data has 4-5 times better angular resolution than this work, and is sensitive to spatial scales down to ∼6 au in this system. Nevertheless, we have higher spectral resolution (3-6 times better) and are less contaminated by cloud absorption than previously published studies in the $J = 2 - 1$ transition, which makes us sensitive to the subtler perturbations reported in this work. To corroborate we show in Figure 4.22 the reported location of their planet, together with the comparable channels, at out spectral and angular resolution. We do not see any deviations at the location of the reported candidate planet in either isotopologue.

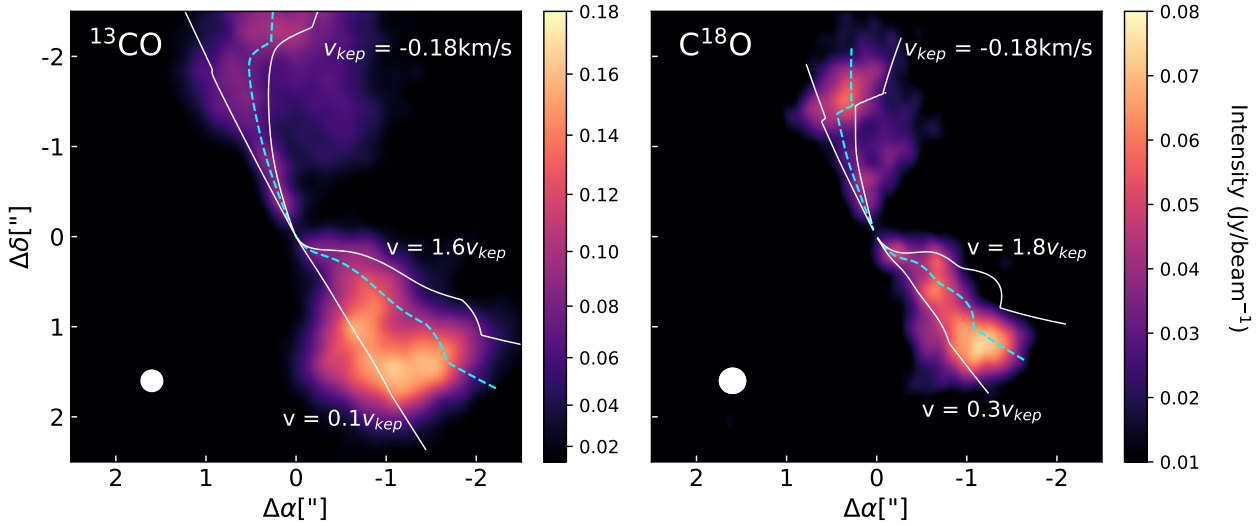


Figure 4.21: Channel emission at 1.77km/s system velocity, corresponding to Keplerian velocity of -0.18km/s in the disk. Blue dashed curve traces isovelocity position, using our constrained emission layer. White curves trace percentual deviations from the isovelocity curves according to values indicated on the figure. Left panel shows $^{13}$CO emission and Right panel C$^{18}$O emission, respective beams and scaling map are shown in each panel.

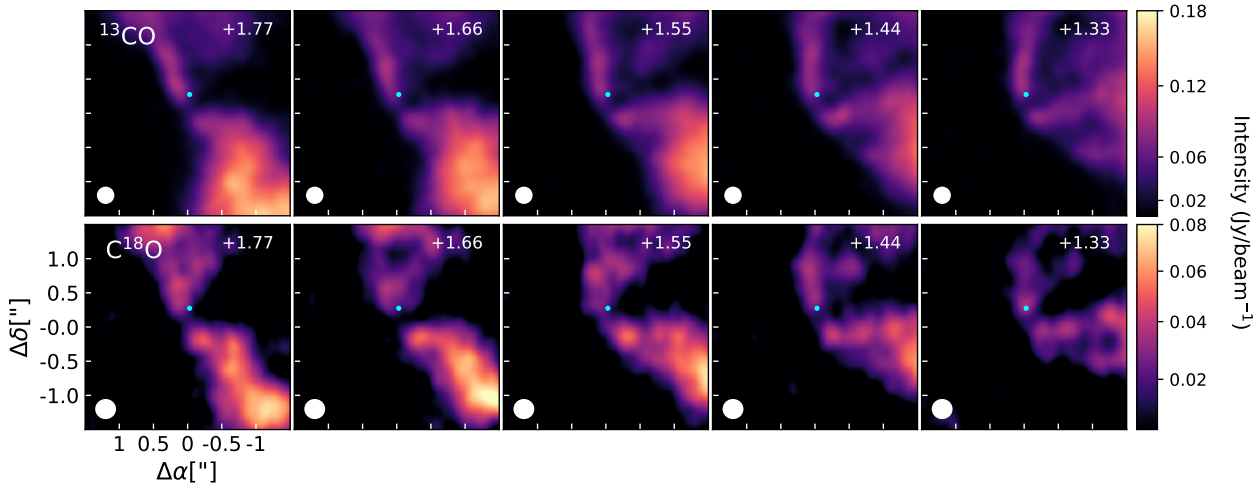


Figure 4.22: Channel maps for $^{13}$CO (top) and C$^{18}$O (bottom) showing location of candidate planet reported for Elias 2-27 through the analysis of local kinematic deviations Pinte et al. (2020).

# Chapter 5

# Tracing CN emission in Elias 2-27

## 5.1. CN as tracer of spiral shocks

As GI originated spiral waves evolve, they may heat the disk material locally through the shocks they produce (Ilee et al., 2011). This heating enhances the rates of chemical reactions, which may significantly affect the chemical composition of discs. The CN molecule is generally used to trace the upper, warm layers of a protoplanetary disk, as it is sensitive to UV radiation, given that its formation requires photodissociation of HCN or HNC (Evans et al., 2015; Cazzoletti et al., 2018b; Chapillon et al., 2012). However, CN may be found in lower layers, closer to the midplane, if: large grain sizes allow UV radiation to penetrate to lower heights (Chapillon et al., 2012), or the desorption temperature that will release CN coupled to dust grains is achieved. For CN the desorption temperature is around 120K (Evans et al., 2015), which is a temperature reached in the spiral arms formed through GI according to hydrodynamical and chemical modelling (Ilee et al., 2011). However, for higher temperatures, CN will be destroyed through its interaction with $NH_3$ (Evans et al., 2015). This resolves in chemical models of GI shocks predicting a large inner cavity depleted of CN, for innermost radii, and CN being a good tracer of the spiral structure at large radial distances (Ilee et al., 2017; Evans et al., 2015), where more moderate temperatures ($\sim$ 120K) are reached (Ilee et al., 2011).

In the CN molecule, each rotational energy level (labeled with quantum number N) splits into a doublet by the spin-rotation interaction (quantum number J), forming three fine structure transitions (Cazzoletti et al., 2018b). Each of the two sub-levels is in turn split by interactions of the nuclei with internally generated electric and magnetic fields (quantum number F) (Ziurys et al., 1982), giving rise to hyperfine structure transitions (Chapillon et al., 2012; Punzi et al., 2015).

## 5.2. CN Emission Analysis

We image emission from different spin-rotational states of CN v=0, N=3-2. Figure 5.1 shows the channel maps for CN v=0, N=3-2, J=7/2-5/2, F=7/2-5/2, at a rest frequency of 340.348 GHz. Figure 5.2 shows CN v=0, N=3-2 J=5/2-3/2 with hyperfine components F=3/2-1/2 and F=7/2-5/2. The rest frequencies for each hyperfine component are 340.035 GHz and 340.031 GHz, respectively (we use 340.035GHz as rest frequency for the system). We note that the observation setup for the spectral window where we observed the hyperfine structure was originally centered to observe the hyperfine component F=3/2-3/2 at a frequency of 340.014GHz, however we only recover emission from the edge channels, at the displayed frequency.

From the channel maps of the single CN transition and the CN with hyperfine structure, we see similar emission features. We can identify top and bottom layers of the emitting surface, however in most channels we don't recover emmission from the far side (North) of the disk. This means we can't apply the previous method used in the CO isotopologues to reconstruct the emitting layer.

Figure 5.3 shows the integrated intensity from the imaged channel maps, at each velocity. We mark our derived system velocity for Elias 2-27 (1.95km/s) and in the case where we observe hyperfine structure we mark in orange 5.3km/s as the velocity where we see "zero" in the channel maps for the second CN transition. As in the case for the CO isotopologues, the higher velocity channels have diminished integrated intensity than their symmetric channel, with respect to the system velocity, due to the absorption that affects the East side of the disk. Though not shown in this work, having hyperfine structure in the intensity measurements of the emission, as a function of velocity (or frequency) can be useful to accurately model the optical depth of the source and determine the excitation temperature of the molecule (Punzi et al., 2015).

From the channel maps we construct integrated emission maps, shown in the upper left corner of Figures 5.4 and 5.5 for the single transition and hyperfine structure CN, respectively. In the case of the observations with hyperfine structure, all frequencies were considered. We observe that the emission comes mainly from the south side of the disk. Previously, in the CO isotopologue's measurements, there was also an asymmetry in the intensity between North and South, however both sides where noticeable even in the outer disk, here the North emission does not go beyond the NW spiral extension ($\sim$250au), as shown when overlaying the continuum spiral contours (Top right panel of figures 5.4 and 5.5) .

The visible emission in the outer disk extends, azimuthally, roughly between 140°-290°, measured from North to East, and at two radial locations the emission seems to decrease. We trace the emission minima as previously with the CO isotopologues, using the azimuthally averaged intensity profile and then sampling azimuthally between a radial range. The deprojected radial distances of the found minimum intensity locations show that there is a considerable scatter between the data points, especially in the "gap" closer in to the central star ($\sim$146au and $\sim$126au for each CN tracer). If the spirals are originated from GI, we expect the CN emission to trace the spiral structure, however, when overlaying the best-fit spiral model and the minima location it appears that the inner decrease in flux is co-located with

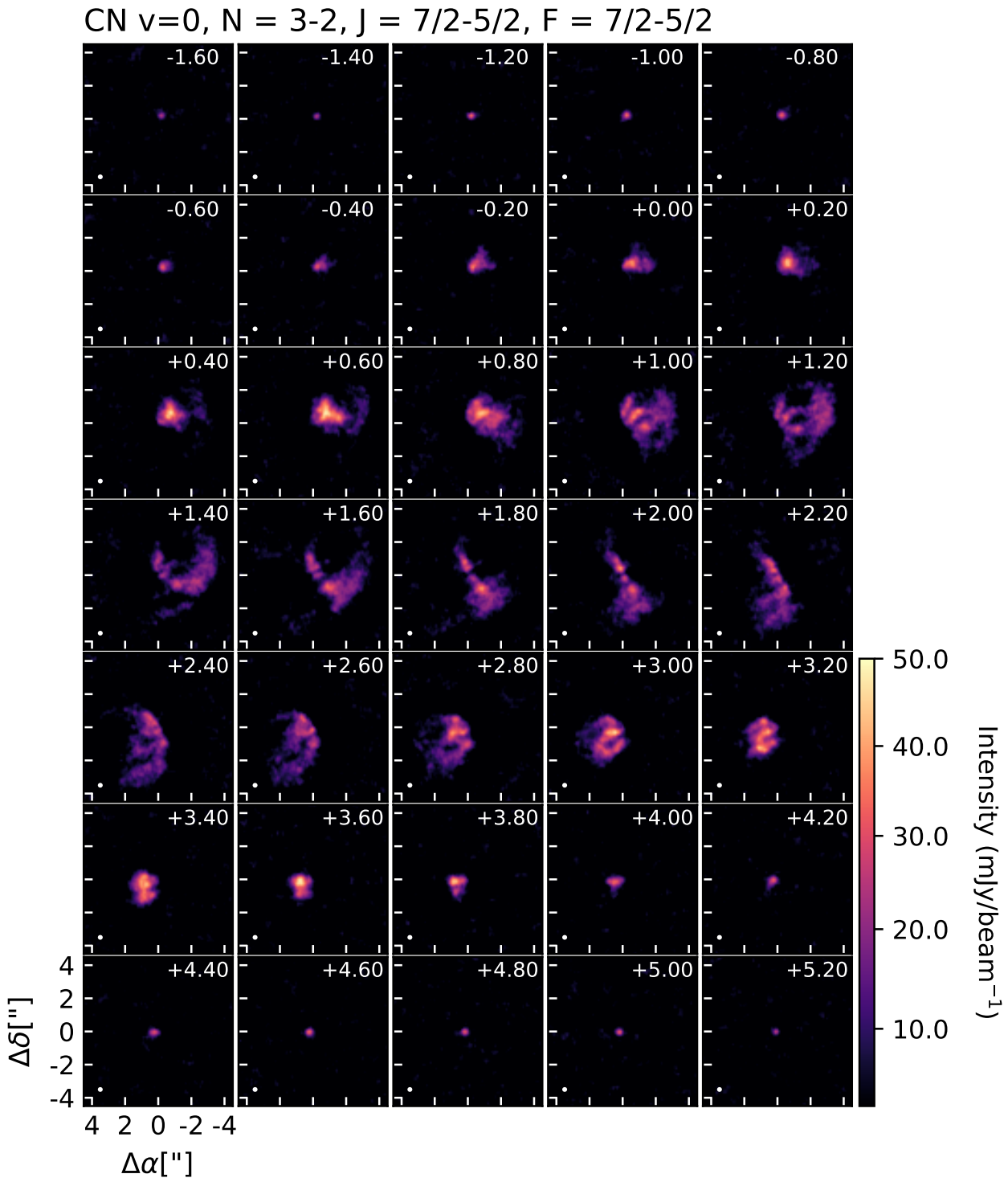


Figure 5.1: Individual emission of each channel for CN v=0, N=3-2, J=7/2-5/2, F=7/2-5/2 emission, corresponding velocities are written in the top right of each panel.

the dust spiral structure, along the NW spiral and outer radii of the SE spiral. On the other hand, the emission between both minimum intensity location may tentatively trace the SE spiral and its extension (dashed line in figures 5.4 and 5.5). However, from the channel maps

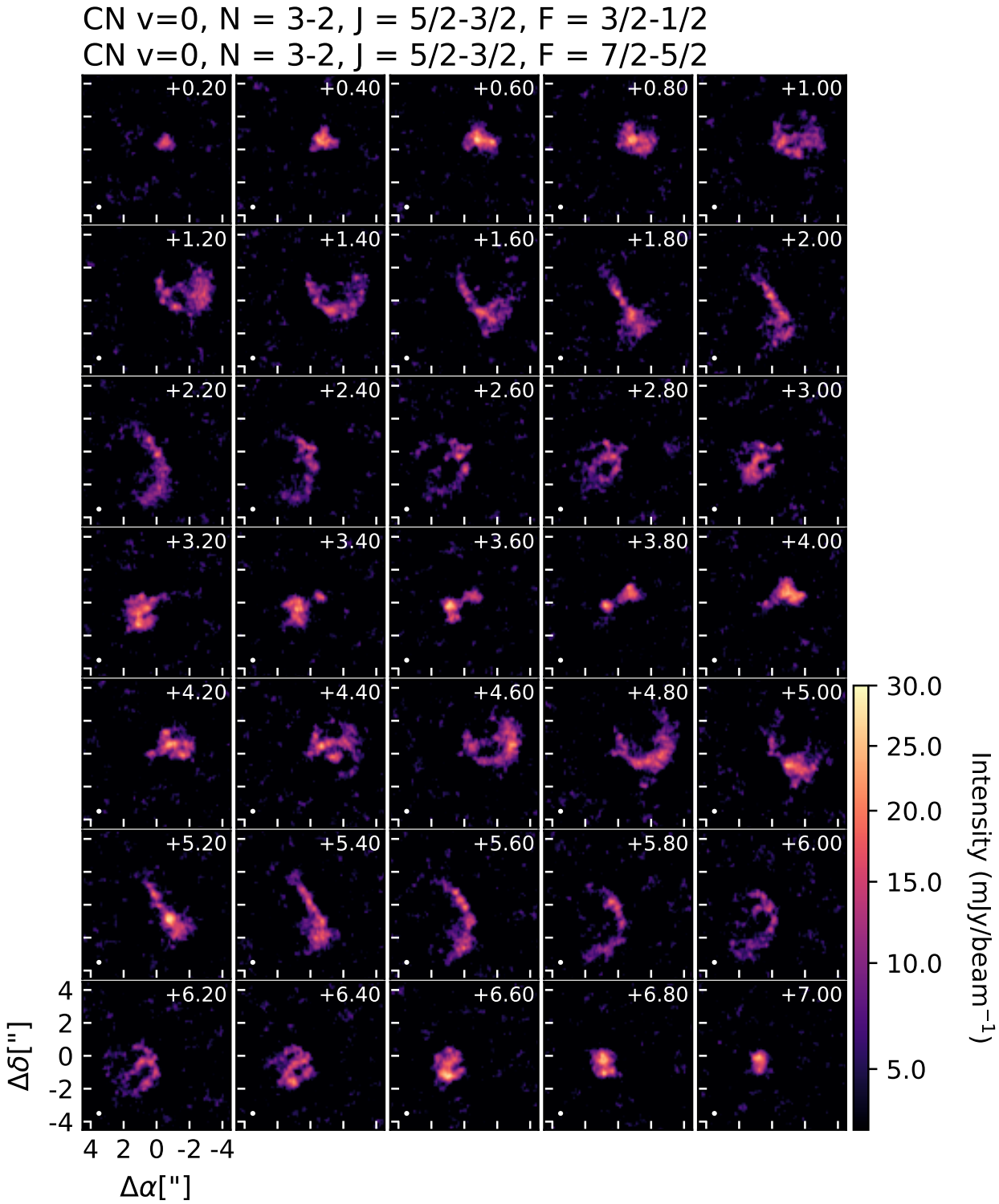


Figure 5.2: Individual emission of each channel for CN v=0, N=3-2, J=5/2-3/2 emission for hyperfine component F=3/2-1/2 and F=7/2-5/2, corresponding velocities are written in the top right of each panel.

we note that the emission does not arise from the midplane, as an elevated emission surface is apparent (we can distinguish top and bottom layers). In Chapter 7 we discuss the impli-

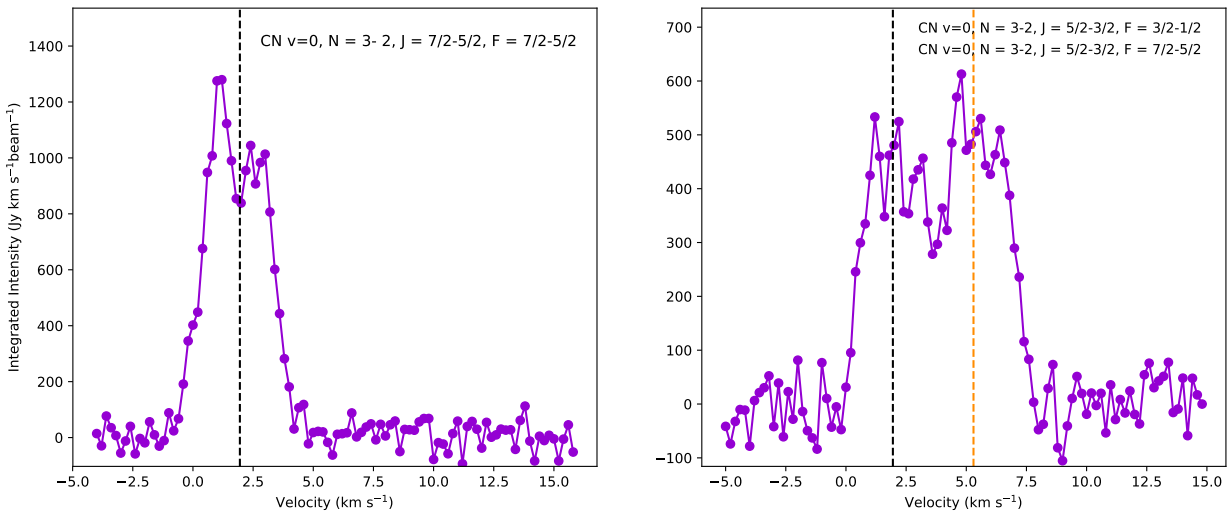


Figure 5.3: Integrated intensity at each imaged channel for both CN transitions, vertical black line indicates systemic velocity (1.95km/s), vertical orange line indicates the "zero" velocity of the second hyperfine transition of J= 5/2-3/2 (5.3km/s) . Note difference between integrated emission scales.

cations of the observed features if they are not arising from the midplane, in which case the co-location of minimum/maximum emission with the dust spirals could be a coincidence due to projection effects. Regarding the outer "gap", it is not co-located with any dust structure, or the extension of the spiral arms (plotted in dashed lines) and the radial location does not coincide with either of the found "gaps" in the CO isotopologues.

We obtain the mean velocity maps for each transition, shown in Figures 5.6 and 5.7. In the case of the CN emission that shows only one transition in the channel maps, the velocity map (figure 5.6) does not seem to show any particular deviations. For the imaging of the mean velocity map from the channels with hyperfine transition (figure 5.7), we roughly choose the channel maps were the main emission comes from each respective transition. For F=3/2-1/2 we use channels between velocities -1.4km/s - 3.6km/s, for F=7/2-5/2 we select emission at velocities 3.6km/s - 8.8km/s. Similar to the velocity maps of the CO isotopologues (figure 4.18) we notice that the velocity maps of the CN molecules simulate emission from a flat emitting surface, however the emission is clearly flared in the channel maps.

The analysis of the CN dataset will be presented in a later publication, following Paneque-Carreño et al. 2020 (in preparation).

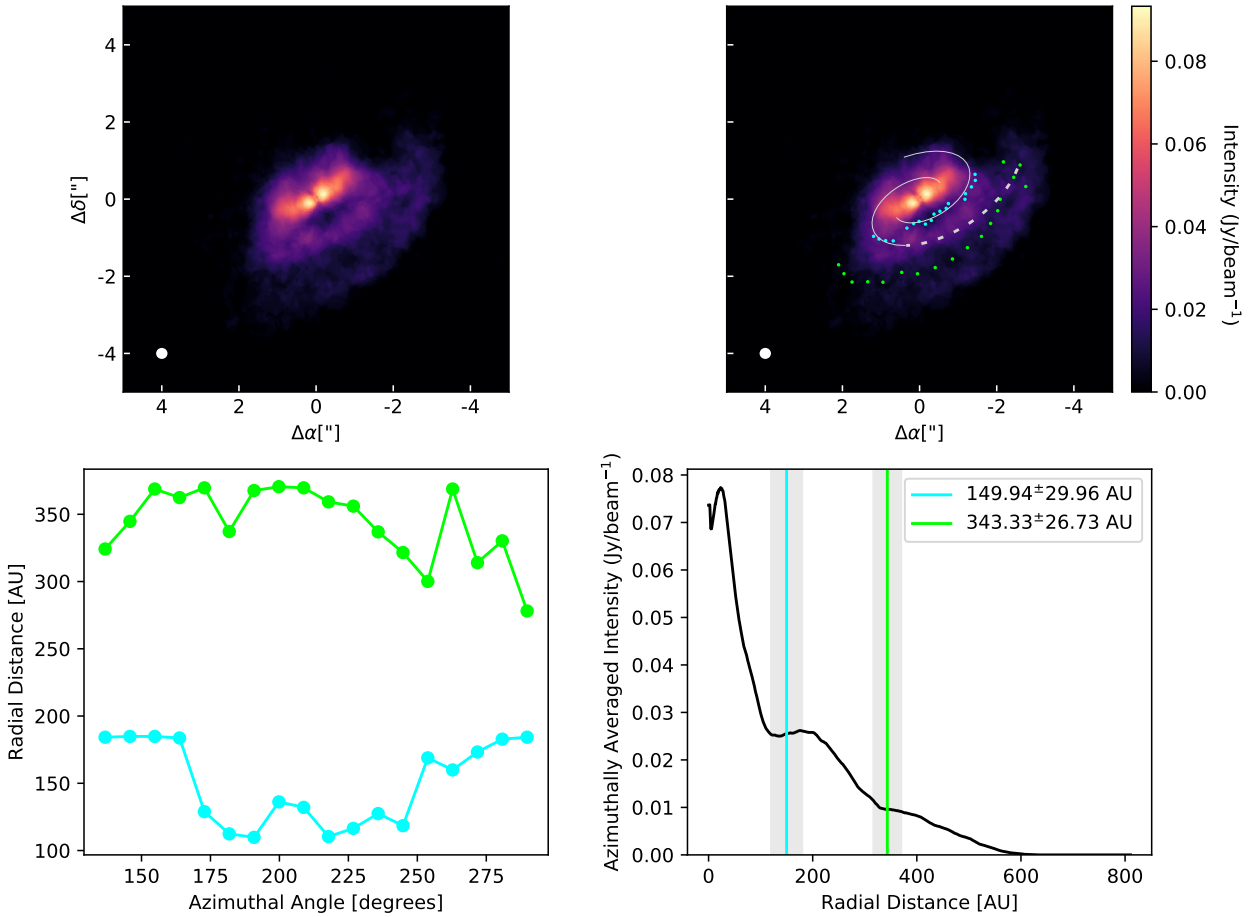


Figure 5.4: Top row: Left, Integrated emission map of CN J=7/2-5/2. Right, Integrated emission map of CN J=7/2-5/2 with minimum flux locations within an azimuthal range shown separated in two radial regions. Overlayed are the dust spirals and their extension. Bottom row: Left, deprojected radial distances of the minima locations. Right, azimuthally averaged profile constructed excluding absorption, vertical line marks average radial location of the minimum of emission and grey area the standard deviation of the locations.

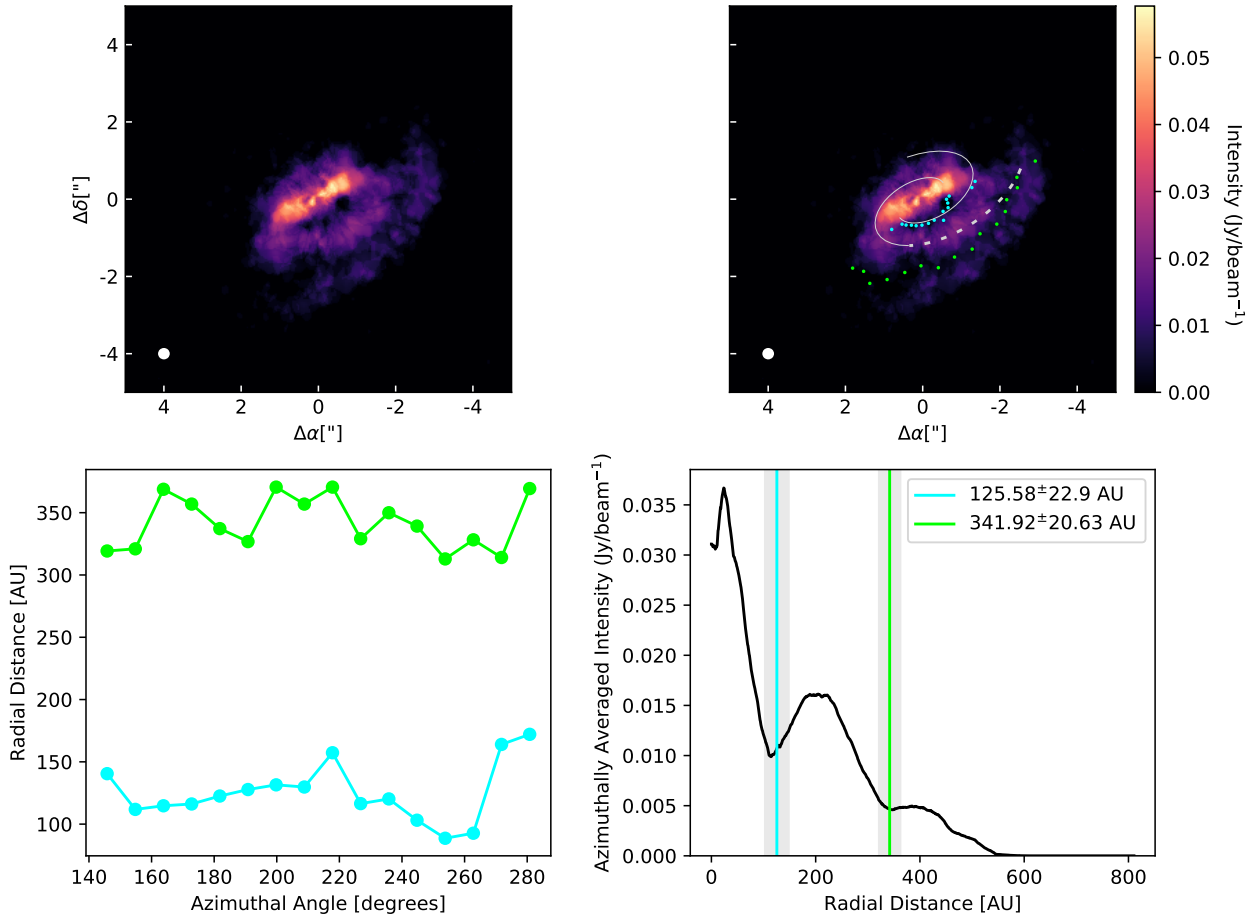


Figure 5.5: Same as Figure 5.4 with the emission of CN J=5/2-3/2. Total emission considers both hyperfine components F=3/2-1/2 and F=7/2-5/2

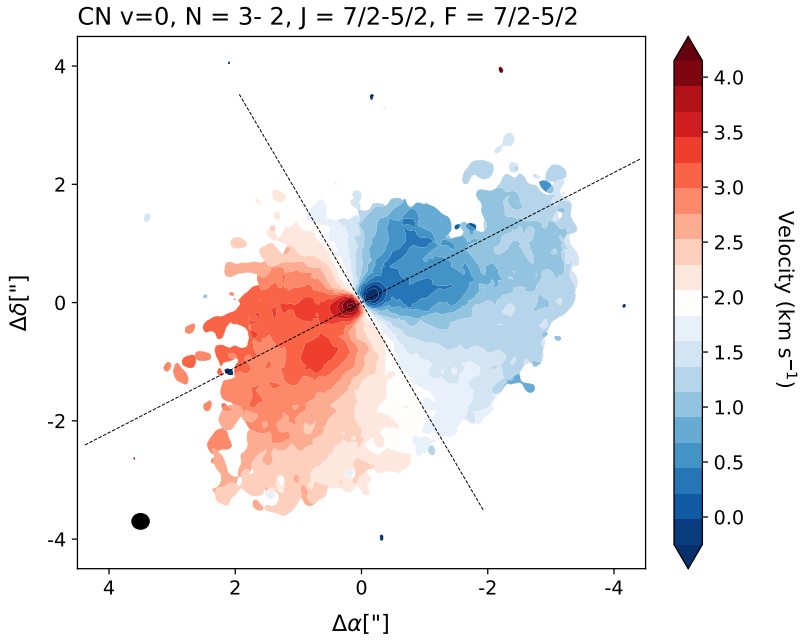


Figure 5.6: Mean velocity map for CN J=7/2-5/2 emission, overlayed are dust minor and major axis.

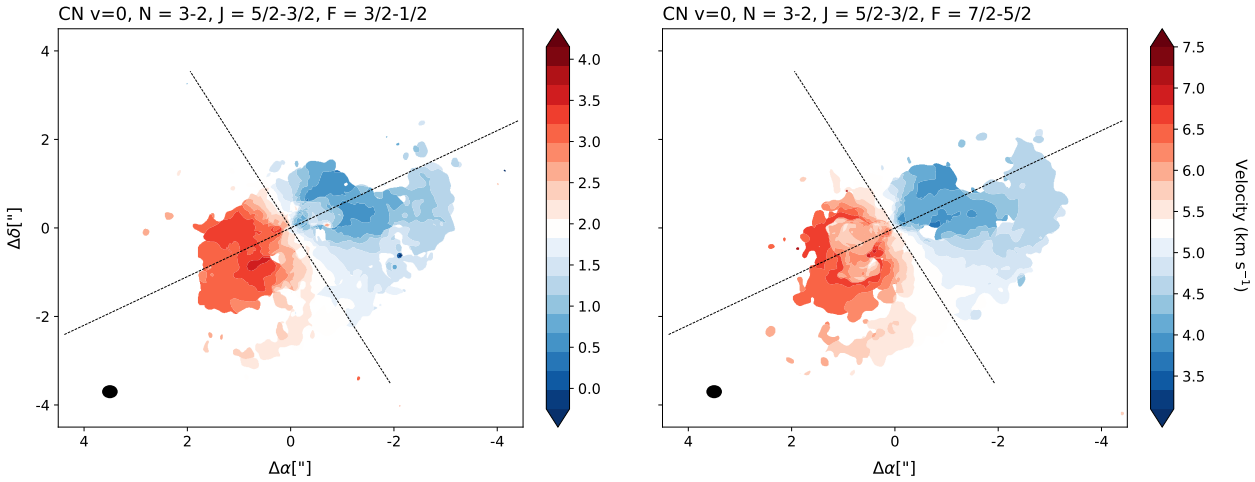


Figure 5.7: Mean velocity maps for CN J=5/2-3/2 emission, separated by hyperfine structure; Left F=3/2-1/2 , Right F=7/2-5/2. Overlayed are dust minor and major axis.

# Chapter 6

# Smooth-Particle Hydrodynamic Simulations of a Gravitationally Unstable Disk

*The analysis presented in this chapter is part of a paper titled "Spiral arms and a massive dust disk with non-Keplerian kinematics: Possible evidence for gravitational instability in Elias 2-27" by Paneque-Carreño et al. 2020 (in preparation).*

Elias 2-27 has been subject to different modelling approaches in order to explain the origin of the observed spiral substructure: Tomida et al. (2017); Meru et al. (2017); Hall et al. (2018); Forgan et al. (2018b); Bae and Zhu (2018b). Most of the modelling efforts have been oriented towards a gravitationally unstable disk as the disk-to-star mass ratio has been measured to have values around 0.2-0.3 (Andrews et al., 2009; Isella et al., 2009; Ricci et al., 2010; Pérez et al., 2016; Andrews et al., 2018a) and as previously discussed, gravitational instabilities are expected when disk-to-star mass ratios are $> 0.1$ (see Kratter and Lodato (2016) or Section 1.3.2). While gravitational instabilities are expected for disks with the disk-to-star mass ratio of Elias 2-27, the m=2 spiral mode observed in this disk is expected to be reproduced at higher disk-to-star mass ratios (m $\sim M_*/M_d$) and previous simulations have aimed at producing the m=2 spirals using higher disk mass estimates ($M_d/M_* \sim 0.5$)than those derived from the observations (Tomida et al., 2017; Meru et al., 2017; Hall et al., 2018; Forgan et al., 2018b).

The relationship m $\sim M_*/M_d$, can be derived from the dispersion relations and theoretical approximations for massive disks used in the theory of gravitationally instabilities (for a detailed overview see Section 3.2 of Kratter and Lodato (2016)). In order to derive this relation, approximations on the disk's features are made, such as having an infinitesimally thin and quasi-Keplerian disk (Kratter and Lodato, 2016; Lau and Bertin, 1978). If these assumptions aren't met, the relationship does not hold. Given these considerations, we attempt to model the system with a lower mass ratio, as constrained observationally, to test if we are able to recover the observed morphology. Even though with the observational value of $M_d/M_* \sim 0.2 - 0.3$ we would expect m=3-5 spirals in the disk, it has been shown that

when producing synthetic ALMA observations, the limited angular resolution will result in lower disk mass systems, with m>2 spirals appearing as systems with m=2 spirals (Dipierro et al., 2014).

## 6.1. Theoretical Considerations

Smoothed Particle Hydrodynamics (SPH) is a numerical method used for solving the equations of fluid dynamics, therefore it is widely used for solving astrophysical problems at all scales, from cosmology (Springel et al., 2001) to stellar (Wurster et al., 2016), planetary (de Val-Borro et al., 2006) and Galactic (Pettitt et al., 2014) astrophysics as well as accretion disks (Lodato and Price, 2010). SPH simulations are based on the idea of calculating a density from a distribution of point-mass particles, where the calculation is: independent of the absolute position of the particles (depend only on their relative separation), independent of arbitrary rotations of the particle distribution, and independent of time or the history of the particles (Price, 2012). The density in SPH is computed using a kernel weighted sum,

$$\rho_a = \sum_b m_b W(|\mathbf{r}_a - \mathbf{r}_b|, h_a) \tag{6.1}$$

where $a$ and $b$ are particle labels, $m$ is the mass of each corresponding particle, $W$ is the smoothing kernel, with weighting that decreases proportional to the radial distance from the measured position $|\mathbf{r}_a - \mathbf{r}_b|/h$, and $h$ is the smoothing length. This sum is performed over neighbouring particles, defined as those within $R_{kern}h$, where $R_{kern}$ is the dimensionless cutoff radius of the smoothing kernel. Through the density summation, the SPH method manages to discretise fluid quantities to single particles of fixed mass, $m$, that will have a certain fluid velocity. The method will follow mass rather than volume, so density will only rise given an increase in particle concentration at a certain location. The latter also results in mass being a conserved quantity, for the particles may not lose, gain or diffuse mass. A larger amount of particles in a simulation will allow for a better resolution and precision in the physical phenomena.

SPH solves the equations of hydrodynamics in Lagrangian form. The basic equations, common to all physics of this method are:

$$\frac{d\mathbf{r}}{dt} = \mathbf{v}, \tag{6.2}$$

$$\frac{d\rho}{dt} = -\rho(\nabla \cdot \mathbf{v}), \tag{6.3}$$

where $\mathbf{r}$ is the particle position, $\rho$ the density and $\mathbf{v}$ the fluid velocity. These equations make use of the Lagrangian time derivative $d/dt = \partial/\partial t + \mathbf{v} \cdot \nabla$, and indicate the Lagrangian update on the particle position and mass conservation.

The equations of compressible hydrodynamics are solved in the form:

$$\frac{d\mathbf{v}}{dt} = -\frac{\nabla P}{\rho} + \Pi_{shock} + \mathbf{a}_{ext}, \tag{6.4}$$

$$\frac{du}{dt} = -\frac{P}{\rho}(\nabla \cdot \mathbf{v}) + \Lambda_{shock} - \frac{\Lambda_{cool}}{\rho}, \tag{6.5}$$

$P$ is the pressure and $u$ the specific internal energy, $\mathbf{a}_{ext}$ represents accelerations from external forces, such as self-gravity. $\Pi_{shock}, \Lambda_{shock}$ are dissipation terms and $\Lambda_{cool}$ a cooling term (for further details refer to Price et al., 2018).

Our simulations use PHANTOM, a SPH code developed for public use, with a focus on the physics and processes that rule stellar, planetary and galactic astronomy as well as accretion disks (Price et al., 2018). The code allows to incorporate modules for physics using magnetohydrodynamics, different forms of dust-gas mixtures, self gravity, among others (Price et al., 2018). We select this code for the modelling of Elias 2-27, as it allows to model the behaviour of several dust sized particles mixed together with the gas and considering self gravity.

PHANTOM considers two approaches for modelling dust-gas mixtures, depending on the Stokes number (St) of the particles. Large particles (St $>$ 1), will not accurately follow the gas motion and in this case dust and gas components must be modelled as two separate types of particles (two-fluid). Small grains (St $<$ 1) will be well coupled to the gas and a single particle type will represent the combination of dust and gas (one-fluid). The implementation of each method follows different descriptions, Laibe and Price (2012a,b) for the one-fluid and Price and Laibe (2015) for two-fluid.

## 6.2. SPH Simulation Results

### 6.2.1. Hydrodynamical Model Setup

We performed a total of 10 three-dimensional, dusty, gaseous hydrodynamical simulations using the SPH code PHANTOM (Price et al., 2018). To accurately compare the simulations to our multiwavelength observations, we use the multigrain setup considering 5 different grain sizes, ranging from 1 micron to 1 cm in 5 logarithmically-spaced size bins, assuming a size distribution of $dn/da \propto a^{-3.5}$. Multiple grain sizes are necessary as, while the most efficient emission at wavelength $\lambda$ comes from dust grains of size $a \sim \lambda/2\pi$ (e.g. Draine, 2006), there is an overall contribution from all grains. The dust is modelled self-consistently with the gas, using the multigrain "one-fluid" approach, where we limit dust flux using the Ballabio switch (Ballabio et al., 2018). Since the disk is massive and self-gravitating, the dust remains in the strongly-coupled regime ($St \lesssim 1$) out to grain sizes of several cm, so we do not need to use the two-fluid approach. In this regime, the dust exerts a force back on the gas (back-reaction)

that has shown to be significant (Dipierro et al., 2018), so we include the effect of this on the gas.

In all 10 simulations we used 1 million SPH particles and assumed a central stellar mass of $0.5\mathrm{M}_{\odot}$, represented by a sink particle (Bate et al., 1995), with accretion radius set to 1 au. We set the initial inner and outer disk radii to 5 au and 300 au respectively. Different simulations vary in disk-to-star mass ratio and density profile. The total dust mass in the system is kept constant at 0.001 $\mathrm{M}_{\odot}$, since this is observationally constrained (Pérez et al., 2016). To obtain different disk-to-star mass ratios what varies is the dust-to-gas ratio ($\epsilon$), which corresponds to $\epsilon = 100, 151$ and 252 for $q = 0.2, 0.3$ and 0.5, respectively. The sound speed profile was set as $c_{\mathrm{s}} \propto R^{-0.25}$, and we used two surface density profiles: either a simple power-law,

$$\Sigma(R) = \Sigma_0 \left(\frac{R}{R_0}\right)^{-p} \tag{6.6}$$

where $\Sigma_0$ is the surface density at the inner edge of the disk, and $p$ either 1.3 or 1.5, or an exponentially-tapered power-law,

$$\Sigma(R) = \Sigma_c \left(\frac{R}{R_0}\right)^{p} \exp\left[-\left(\frac{R}{R_c}\right)^{2-p}\right] \tag{6.7}$$

where $R_c$ is the characteristic radius of the profile, which we set to $R_c = 200$au and $p$ either 0.7 or 1.0. In both surface density profiles $R_0$ is the reference radius and is set to $R_0 = 10$au.

We set a polytropic equation of state, and assumed that the disk cooled through the $\beta$ cooling prescription (Gammie, 2001), a simple cooling prescription where the cooling timescale, $t_{\mathrm{c}}$, is related to the dynamical timescale, such that $t_{\mathrm{c}} = \beta t_{\mathrm{dyn}}$. The dynamical timescale is the rotation period, $2\pi/\Omega$, and we set $\beta = 15$. Finally, each simulation is computed for 10 orbital periods at the outer radius (300 au), from which we receive outputs every 0.1 fraction of an orbital period. The detail of the model parameters are shown in Table 6.1.

Table 6.1: SPH Model Parameters

| Param. | Value |
|---|---|
| $M_*$ $[M_\odot]$ | 0.5 |
| $R_{in}$ [au] | 5 |
| $R_{out}$ [au] | 300 |
| $M_{dust}$ $[M_\odot]$ | 0.001 |
| gas-to-dust mass ratio | 100, 151, 252 |
| Min. Grain size [cm] | $1 * 10^{-4}$ |
| Max. Grain size [cm] | 1 |

### 6.2.2. Radiative Transfer Calculation and Simulated ALMA Observations

While SPH simulations potray the overall dynamic behaviour of a system, in order to accurately compare the model to an observation it is necessary to produce radiative transfer calculations of the SPH outputs, and then simulate mock observations using the same observing conditions (uv coverage) than the actual observations. Radiative transfer is necessary because it accounts for the multiwavelength emission the grains will have given the stellar characteristics and grain distribution. Sampling the radiative transfer output with the same observing configuration is crucial, for the antenna distribution and observation time will result in a given angular resolution and will form an image according to the sampled uv-coverage.

The Monte Carlo radiative transfer MCFOST code (Pinte et al., 2006, 2009) was used to compute the disk thermal structure and synthetic continuum emission maps at each observed wavelength (0.89mm, 1.3mm and 3.3mm). We assumed $T_{\rm gas} = T_{\rm dust}$, and used $10^7$ photon packets to calculate $T_{\rm dust}$. We set the parameters for the central star to match those of the Elias 2-27 system (Andrews et al., 2009; Pérez et al., 2016), with temperature $T = 3850$ K, $M = 0.5 {\rm M}_\odot$ and $R_* = 2.3$ ${\rm R}_\odot$.

To create the density structure as input into the MCFOST calculation, each SPH simulation underwent Voronoi tesselation such that each SPH particle corresponds to one MCFOST cell. We assumed the dust is a mixture of silicate and amorphous carbon (Draine and Lee, 1984) and optical properties were calculated using Mie theory. The grain population consists of 100 logarithmic bins ranging in size from 0.03 $\mu$m to 1 mm. The dust density of a grain size $a_i$ was obtained by interpolating from the SPH dust sizes in each cell in the model. We assume that grains smaller than half the smallest SPH grain size (0.5 $\mu$m) are perfectly coupled to the gas distribution. We normalised the dust size distribution by integrating over all grain sizes, where a power-law relation between grain size $a$ and number density of dust grains $n(a)$ was assumed such that ${\rm d}n(a) \propto a^{-3.5}\,{\rm d}a$.

The radiative transfer emission map of each wavelength was sampled with the same uv-coverage as the observations at each corresponding wavelength, using GALARIO (Tazzari et al., 2018) to create mock ALMA visibilities that were afterwards processed using the same deconvolution procedures as with the observations (described in Chapter 2) to obtain the final mock ALMA images.

### 6.2.3. Dust Simulations

For each simulation image we subtract its azimuthally-averaged radial profile of emission, following the same procedure previously described (Section 3.1) to trace the spiral morphology on the multi-wavelength observations. We find that most of our models are able to accurately reproduce the m=2 large-scale spiral morphology. To select the simulation that best resembles our observations, we measure the spiral's pitch angle and compare them to those constrained by observations. The pitch angles measured for each spiral and model setup are shown in Table

6.2. The comparison between the model pitch angle ($\phi_{model}$) and the observation pitch angle ($\phi_{obs}$) is done considering the difference between the values of each spiral and wavelength and weighting by the error of the observation pitch angle ($\sigma_{obs}$), following a likelihood parameter determined by:

$$\sum_{\lambda} \sqrt{\left[ \left( \frac{\phi^{NW}_{model} - \phi^{NW}_{obs}}{\sigma_{obsNW}} \right)^2 + \left( \frac{\phi^{SE}_{model} - \phi^{SE}_{obs}}{\sigma_{obsSE}} \right)^2 \right]_{\lambda}} \tag{6.8}$$

The simulation that best reproduces the observed pitch angle follows a dust density profile of an exponentially tapered power-law with index 1.0 and a disk-to-star mass ratio of 0.3, which are the set of model parameters close to the previously published observational constrains for this disk (Pérez et al., 2016), this simulation is shown in Figure 6.1. The parameters of this SPH simulation are able to reproduce the observed pitch angles and therefore the shape of the spirals, additionally, the radial extension of these features and their overall morphology in the simulation is similar to the observations.

We note that, even though there is a simulation that reproduces the observations better than the rest, the pitch angles of the different SPH simulations are in most cases comparable to those of the observations ($\sim 12.9°$ and $\sim 13.2°$, for NW and SE spiral respectively, with small variations between wavelengths), showing that it is possible to reproduce the grand-design spirals even at lower disk-to-star mass ratios than previously tested in this system (Hall et al., 2018; Meru et al., 2017), with stellar mass, disk dust mass and density profile values comparable to observational constrains. The likelihood value of the rejected models is shown in Table 6.2. Additionally, we see that not all GI spirals, recovered from the models and measured with our method (section 3.1), are perfectly symmetric (same pitch angle), which is a property that has been predicted in other works for GI excited spiral arms (Forgan et al., 2018b), this is specifically observed in the models with q=0.2. The rejected models and the deprojection of the spiral arm maximum intensity peaks, from the substracted images of each model, compared to the observational values, are shown in Appendix B (Figures B.2, B.4, B.6).

### 6.2.4. Gas Simulations

From the simulation that best reproduces the pitch angle of the spiral arms (q = 0.3, dust density profile with a tapered power-law of index 1.0), we compute the simulated channel maps. As with the dust simulations, we use MCFOST (Pinte et al., 2006, 2009), with the previous parameters, to compute the disc thermal structure and synthetic $^{13}$CO $J = 3 - 2$ and C$^{18}$O $J = 3 - 2$ line maps. The molecule abundances, relative to local $H_2$ are set to 7 x $10^7$ for $^{13}$CO (as done in Hall et al., 2020) and 2 x $10^7$ for C$^{18}$O (following the estimate from Frerking et al., 1982). The spectral resolution for the kinematic simulations is set to 0.111km/s to match the observations and we additionally compute C$^{18}$O channel maps with 0.05km/s resolution, to compare with the finer spectral resolution data.

While in the radiative output we observe the characteristic "GI-wiggle" shown by Hall

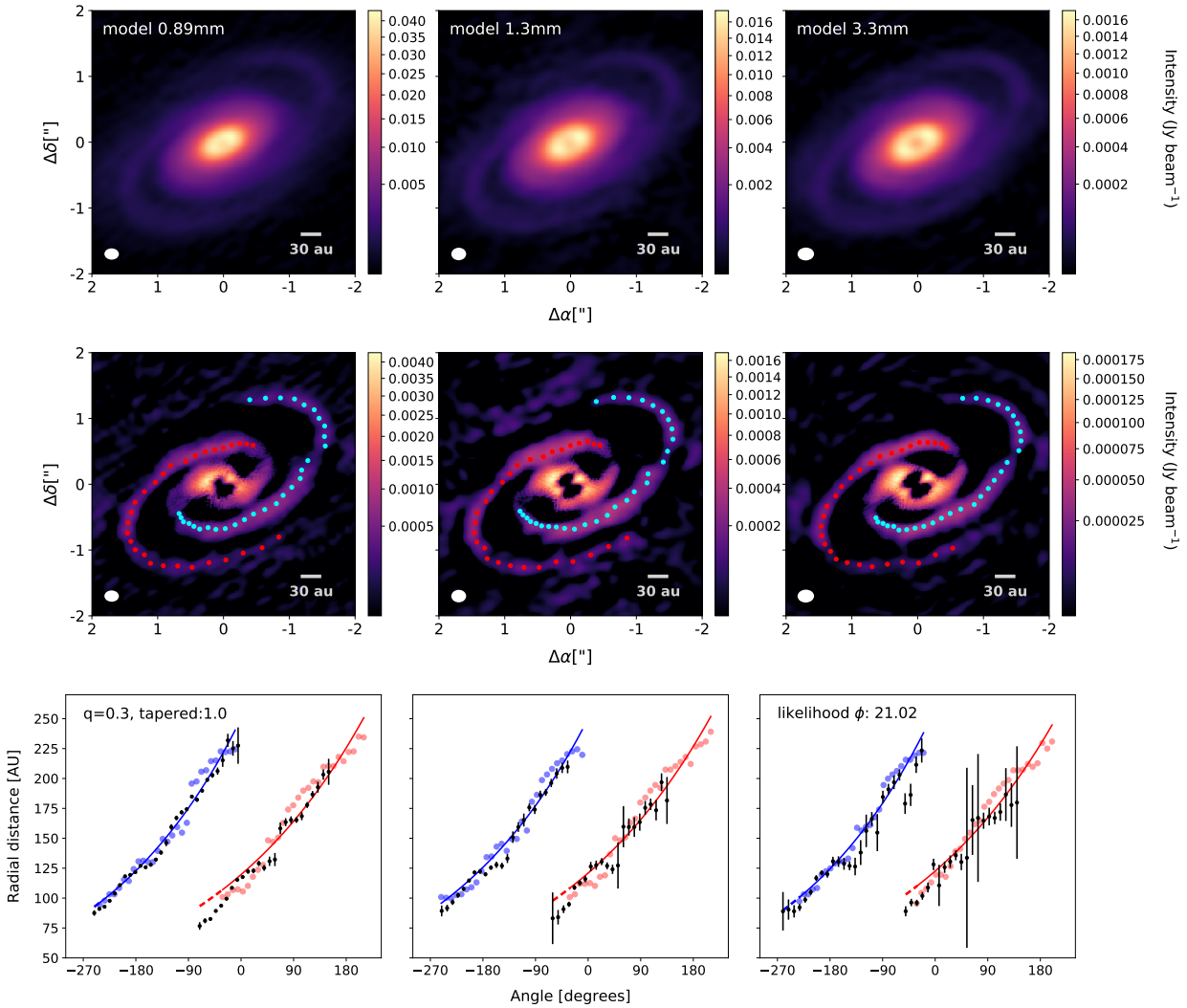


Figure 6.1: Panels from Left to Right correspond to data from the 0.87mm, 1.3mm and 3mm simulated observations for a exponentially tapered dust density profile with index 1.0 and disk-to-star mass ratio $q$=0.3. Top: Simulated emission. Middle: Substracted images of simulated emission, blue and red dots trace the maxima location along the spirals. Bottom: blue and red dots correspond to the deprojected radial location of the traced spirals and colored solid lines show the constant pitch angle logarithmic spiral fit, dashed colored lines extend the fit to lower radii. Black points are the deprojected radial location of the spirals from the observations (Section 3) and their astrometric error. Pitch angle likelihood parameter is shown in the top left corner of bottom row third panel.

et al. (2020) at the spiral arm's location, when sampling the data with the observation's uv-coverage the "GI-wiggle" is not visible in either isotopologue (shown in Figures 6.2, 6.3). In the work by Hall et al. (2020) the "GI-wiggle" remains visible even after convolving with a gaussian beam, however we note that our simulated ALMA images have a ∼4 times lower spectral resolution (0.111km/s compared with 0.03km/s) and ∼3 times lower angular

resolution (0.3" compared to 0.1"). While the higher spectral resolution $C^{18}O$ observations have a comparable channel width (0.05km/s) with the analysis of Hall et al. (2020), the angular resolution smears the "GI-wiggle" features (Figures 6.4, 6.5). We also note that no North/South brightness asymmetry is present in the simulated channel maps and additional channel maps computed with a 90° inclination do not show any significant vertical difference between East/West sides.

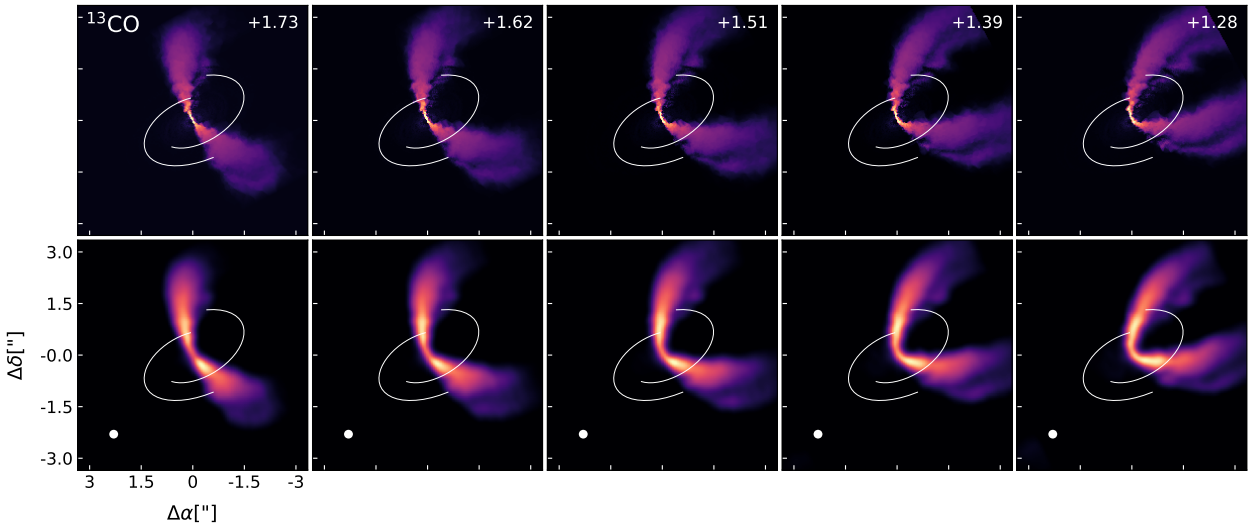


Figure 6.2: Simulated $^{13}$CO emission, channels selected for comparison with Figure 4.19. Top row shows MCFOST output, bottom row shows the emission after applying uv-coverage as in observations and processing with CASA. White lines trace the spirals from the best-fit simulation (q=0.3, exponentially tapered dust density profile index 0.7). The beam for the simulated ALMA images is shown in the bottom left of each bottom row panel.

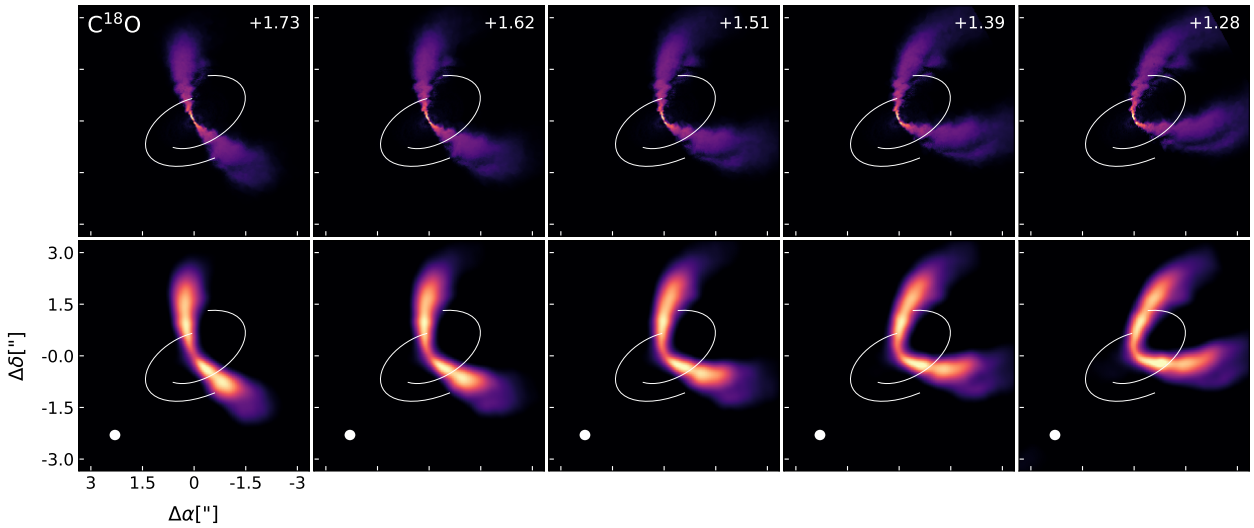


Figure 6.3: Same as Figure 6.2, for the simulated $C^{18}O$ emission.

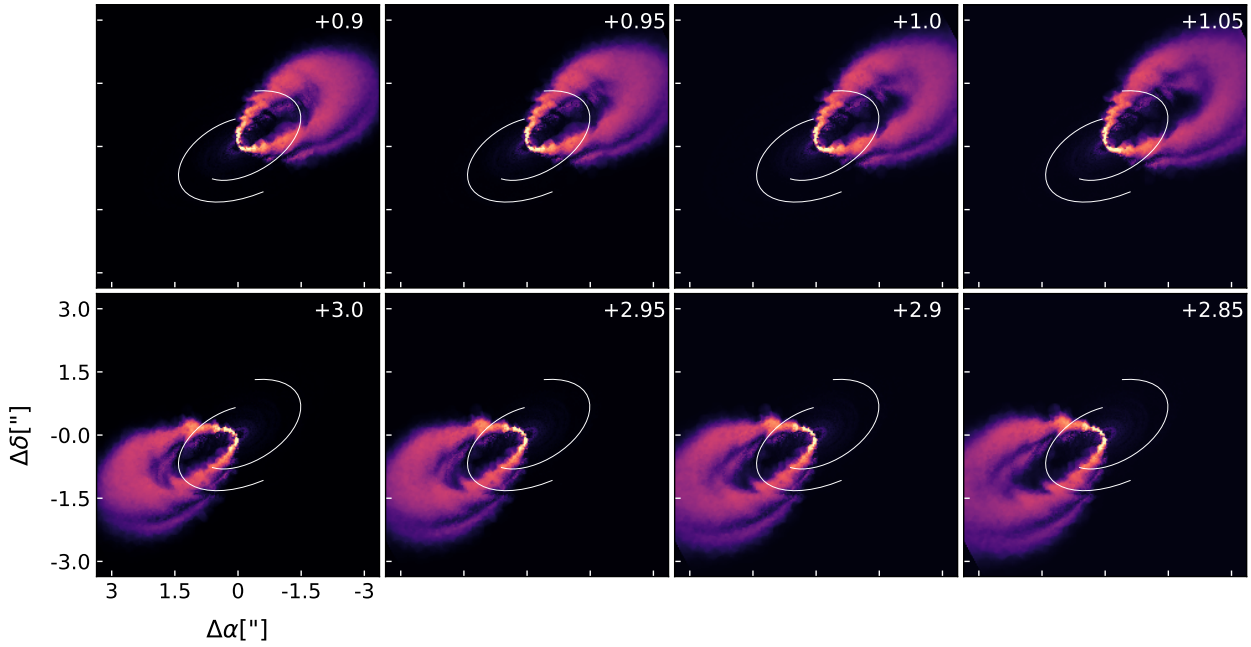


Figure 6.4: Simulated $C^{18}O$ emission from MCFOST output. Imaged at 0.05km/s spectral resolution and channels selected for comparison with Figuure 4.20. White lines trace the spirals from the best-fit simulation (q=0.3, exponentially tapered dust density profile index 0.7).

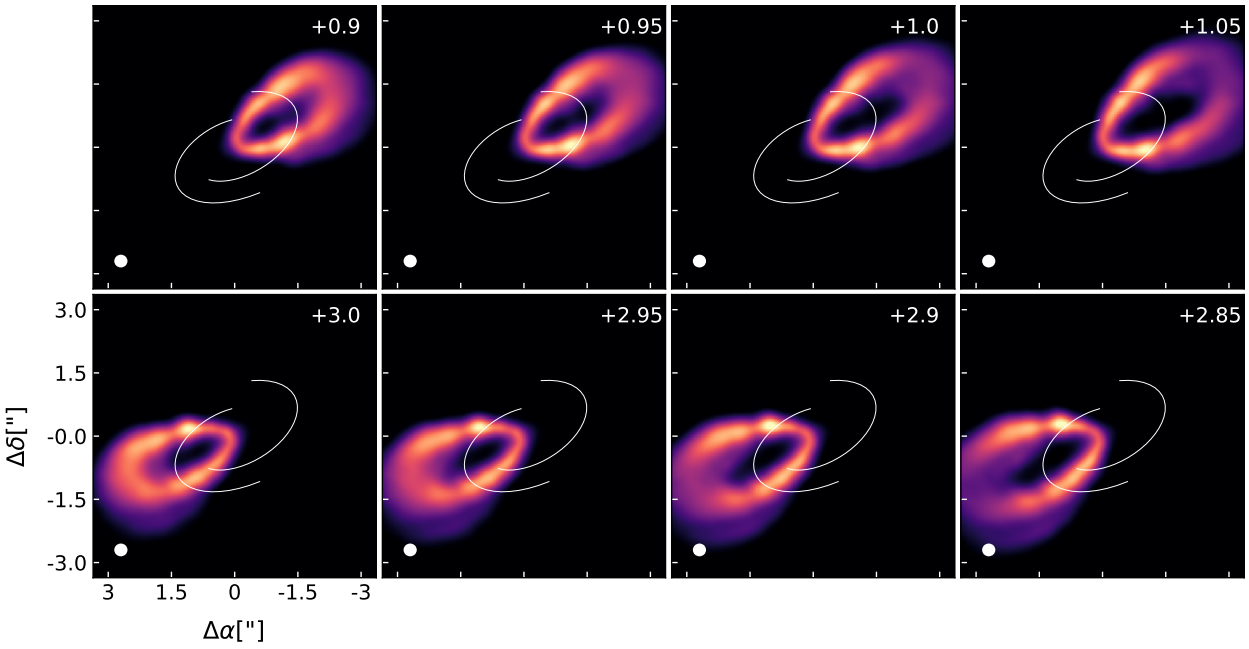


Figure 6.5: Simulated $C^{18}O$ emission after applying uv-coverage as in observations and processing with CASA. The beam is shown in the bottom left of each bottom row panel. White lines trace the spirals from the best-fit simulation (q=0.3, exponentially tapered dust density profile index 0.7).

Table 6.2: Pitch Angle values for Simulations

| Simulation | $NW_{0.87mm}$ | $SE_{0.87mm}$ | $NW_{1.3mm}$ | $SE_{1.3mm}$ | $NW_{3mm}$ | $SE_{3mm}$ | likelihood $\phi$ |
|---|---|---|---|---|---|---|---|
| tapered: 0.7 | | | | | | | |
| q = 0.2 | 13.46° ± 0.08° | 14.96° ± 0.08° | 10.86° ± 0.06° | 15.27° ± 0.08° | 9.85° ± 0.07° | 13.7° ± 0.1° | 29.31 |
| q = 0.3 | 12.52° ± 0.06° | 11.54° ± 0.06° | 12.24° ± 0.06° | 10.82° ± 0.05° | 12.09° ± 0.06° | 10.6° ± 0.06° | 24.04 |
| q = 0.5 | - | - | - | - | - | - | - |
| tapered: 1.0 | | | | | | | |
| q = 0.2 | - | - | - | - | - | - | - |
| q = 0.3 | 12.75° ± 0.06° | 11.42° ± 0.05° | 12.34° ± 0.06° | 11.33° ± 0.05° | 13.08° ± 0.06° | 11.19° ± 0.05° | 21.04 |
| q = 0.5 | - | - | - | - | - | - | |
| power law: 1.3 | | | | | | | |
| q = 0.2 | 13.9° ± 0.08° | 11.16° ± 0.11° | 14.75° ± 0.07° | 10.40° ± 0.08° | 14.82° ± 0.07° | 10.48° ± 0.11° | 36.19 |
| q = 0.3 | 14.88° ± 0.07° | 15.66° ± 0.07° | 15.53° ± 0.06° | 15.36° ± 0.07° | 15.34° ± 0.07° | 15.92° ± 0.06° | 45.32 |
| q = 0.5 | 14.86° ± 0.07° | 18.08° ± 0.07° | 14.47° ± 0.06° | 17.74° ± 0.08° | 14.2° ± 0.06° | 18.82° ± 0.07° | 53.08 |
| power law: 1.5 | | | | | | | |
| q = 0.2 | 10.94° ± 0.09° | 7.34° ± 0.06° | 12.38° ± 0.09° | 5.8° ± 0.07° | 11.49° ± 0.08° | 8.24° ± 0.07° | 66.08 |
| q = 0.3 | 12.03° ± 0.06° | 11.95° ± 0.07° | 11.55° ± 0.06° | 10.4° ± 0.06° | 11.94° ± 0.06° | 11.05° ± 0.07° | 27.36 |
| q = 0.5 | 11.04° ± 0.06° | 10.76° ± 0.05° | 10.62° ± 0.06° | 10.74° ± 0.05° | 10.42° ± 0.05° | 10.5° ± 0.05° | 46.58 |

# Chapter 7

# Discussion

## 7.1. Dust structure and multi-wavelength emission

The morphology of the dust spiral structure can be a key indicator towards the origin of the spirals. We measure symmetric spirals, present in all three wavelengths, with similar radial extension and pitch angles. Symmetric spirals with constant pitch angles are predicted in the case of GI (Forgan et al., 2018b), rather than for companion perturbations where asymmetric, variable-pitch angle spirals are expected (Bae and Zhu, 2018b). Additionally, we measure similar contrasts for both spirals ($\sim 30\,\%$ difference in contrast between NW and SE spirals), which is also consistent with GI predictions, as companion induced spirals are expected to show a clear primary spiral (Bae and Zhu, 2018b).

Another interesting aspect in the dust continuum emission of Elias 2-27 are its spectral index and optical depth measured under standard assumptions. Millimeter wavelengths are expected to trace optically thin emission toward the midplane of protoplanetary disks (Beckwith et al., 1990), however, mass estimates from various surveys have shown that the solid mass in protoplanetary disks is much lower than needed to be able to form several planets (Andrews et al., 2013; Ansdell et al., 2016; Cieza et al., 2019), opening the discussion to the possibility of some material being hidden in regions of high optical depth (Andrews et al., 2018b). To explain this "missing mass" and optical depth problem, several works have shown that when scattering from dust grains is considered, optically thick disks can display lower intensities and be categorized as optically thin disks (Zhu et al., 2019; Liu, 2019; Sierra and Lizano, 2020).

Optically thick emission in the presence of dust scattering can be recognized through multi-wavelength observations and its spectral index, since when scattering is not present and the emission is optically thin, then $\alpha$ cannot reach values below 2.0. When dust scattering is included, a region of high optical depth can have $\alpha < 2.5$ and even attain an spectral index below 2.0 if the albedo decreases with wavelength (Zhu et al., 2019; Sierra and Lizano, 2020), something observed in the innermost regions of TW Hya for example (Tsukagoshi et al., 2016; Huang et al., 2018a). Furthermore, while $\alpha$ also depends on other dust properties, such as the grain size distribution (e.g., Testi et al., 2014), values of $\alpha < 3$ are not expected when

the optical depth is low, and even in presence of cm-sized grains $\alpha$ should not attain values below $\sim 2.5$ (Zhu et al., 2019).

From our spectral index profiles $\alpha_{1-3mm} < 2.0$ in the inner $\sim$30au and $\alpha_{1-3mm} < 2.5$ inside $\sim$70au, outside this region $\alpha_{1-3mm} \sim 2.5$, reaching a maximum value of 2.7 in the outermost radii. This indicates that the outer disk is either optically thin with grains of 0.1-10cm, favouring a dust distribution $n(s) \propto s^{-2.5}$ or optically thick with maximum grain sizes $\sim$0.1cm (Zhu et al., 2019). While our results indicate that large grains are present in the outer disk, the 2D spectral index map (see Figure 3.9) does not show any spatial relation between the spiral features and the location of larger grains (lower $\alpha$ values), as expected for GI originated spirals (Dipierro et al., 2015). The non-detection of these features could, however, be due to our low spatial resolution, which barely resolves the spiral arm width.

Regarding the inner disk ($\lesssim$ 70au), where the spectral index reaches values of $\alpha_{1-3mm} < 2.5$ and even below 2.0, the emission is most likely optically thick and dust scattering is at work, even when the maximum optical depth we constrain is $\tau \sim 0.5$ at these wavelengths, decreasing down to $\tau \sim$0.1 at 70au. This suggests that scattering may be a relevant process in Elias 2-27, causing lower optical depths to be measured in the standard assumption of no scattering and only absorption opacity. It has been shown that the optical depths calculated for the DSHARP sample, which in most cases had $\tau \sim 0.6$ at 1.3mm in bright rings, can be obtained from optically thick regions with a scattering albedo of $\omega_\nu \sim$0.89 (Zhu et al., 2019). Specifically for Elias 2-27, we measure an average $\tau \sim 0.34$ at 1.3mm inside 70 au, which could be obtained with a scattering albedo of $\omega_\nu \sim 0.97$ (see equations 14 and 15 from Zhu et al. (2019)). This albedo value is sufficient to mask optically thick emission ($\tau_{real} \sim$1-5) in the inner disk, which we would be constraining as optically thin emission ($\tau_{obs} \sim 0.34$) in the standard assumption of only absorption opacity.

The scattering in Elias 2-27 also impacts its mass estimates, since underestimating optical depths when scattering is excluded leads to a significant underestimation of disk masses, heightened for inclined disks and when the emission area is compact (Zhu et al., 2019), just like for our source and particularly at the inner disk regions. In the case of Elias 2-27, which has extended emission (up to $\sim$250 au) most of the dust mass is expected to be at the outer disk, which is optically thin, so disk mass could be underestimated by a factor of $\sim$2 (Zhu et al., 2019). This results in a twice higher disk-to-star mass ratio than previously constrained, which was 0.1-0.3 considering a stellar mass of 0.49$M_\odot$ (Andrews et al., 2018a) and total disk mass of 0.04-0.14 $M_\odot$ (Andrews et al., 2009; Ricci et al., 2010, assuming a gas-to-dust ratio of 100), making gravitational instabilities a likely cause for the spiral structure.

## 7.2. Asymmetries and Perturbations in the Gas

The highly perturbed morphology constrained for the emitting gas layer in Elias 2-27 is a new characteristic for this system and offers new insight into the ongoing dynamic processes. The asymmetric structure of the $^{13}$CO and C$^{18}$O emitting layer, as well as the dust spiral arms present in Elias 2-27, could be in principle caused by a fly-by interaction (e.g., Cuello et al., 2019). But if this were the case, we should also expect a strong kinematical perturbation in

the integrated emission and velocity maps of Elias 2-27, such as those reported by Kurtovic et al. (2018) for disks with known external companions. Furthermore, observations in near-infrared of Elias 2-27 have not found any companion, at a resolution that allows for the detection of sub-stellar companions (30-50$M_{Jup}$) in other systems (Cieza et al., 2009; Zurlo et al., 2020).

With no outer perturbation, the scale height of the gas should follow hydrostatic equilibrium and depend on the gas temperature, from where we expect a cone-like or flared emission layer and scale height increasing with radial distance (Armitage, 2015; Williams and Cieza, 2011). We will discuss two possible origins for the observed asymmetries in the gas: ongoing infall of material from its surrounding cloud/envelope, or a warped inner disk causing azimuthal temperature variations.

Three-dimensional simulations of circumstellar disks with ongoing moderate accretion have shown that the vertical structure of the disk will become asymmetric, as the accreting gas may be shocking the disk from above or below, along the $z$ plane, as described by cylindrical coordinates (see Fig. 8 in Hennebelle et al., 2017). Furthermore, simulations for ongoing infall predict the appearance of spiral structures in the surface, generated by the infall process and shocks, both in 3D simulations (Hennebelle et al., 2017; Harsono et al., 2011) and 2D simulations (Lesur et al., 2015). From our observations, we have shown the presence of large-scale emission surrounding the disk (see Figures 4.6, 4.7 and 4.9), although this data lacks appropriate uv-coverage to accurately sample the whole FOV and look for velocity gradients connecting the large-scale emission to the disk emission. Nevertheless, it opens up the option for infall to be ongoing in Elias 2-27, while this is not expected for a Class II source, it has been proposed it could be a very young Class II disk (Tomida et al., 2017).

An azimuthal variation of the temperature in a disk could also explain an azimuthally varying scale height, which can be expected when a disk is warped. A warp will affect the disk illumination, depending on the position and characteristic angles of the warp itself (Nixon and Pringle, 2010), as these are generally detected through their shadowing effects in scattered light (Marino et al., 2015; Benisty et al., 2018) and their distinct kinematical signatures (Juhász and Facchini, 2017; Pérez et al., 2020; Walsh et al., 2017). Unfortunately, no scattered light observations are available for Elias 2-27 given its high extinction, and thus, we can only compare our observations to kinematic predictions for a warp.

In ALMA observations, a misaligned disk can be inferred through the kinematical signature in the velocity map: if a non-misaligned disk is modeled then positive and negative residuals appear, opposite with respect to a "symmetry" axis (e.g., as seen in the velocity field residuals for HD100546 or HD143006, Walsh et al., 2017; Pérez et al., 2018a). We do not observe such residuals in our data (see. Figure 4.18), rather we see an "X" shaped residual in the $C^{18}O$ emission. Other signatures related to warps are asymmetric illumination, deviations in line profiles, and twisted features in the channel and integrated emission maps (Juhász and Facchini, 2017; Facchini et al., 2018). The gas emission of Elias 2-27 is characterized by a strong illumination asymmetry between North-South sides of the disk, additionally, we have shown the presence of "curved" and "wavy" features and deviations in both the integrated velocity maps and velocity cube (see Figures 4.18 and 4.19 respectively). These features may

relate to an inclined disk, warped such that the disc bends perpendicular to the line of sight (see Case C in Juhász and Facchini (2017)). The latter configuration shows channel maps with curved structures and asymmetric illumination, such as observed in our data, while it also shows further structure in the integrated intensity map and asymmetric line profiles (Juhász and Facchini, 2017). We note that we do not expect to be sensitive to all these features given our moderate spatial resolution (simulations are done with resolution $\sim 0.1$", we have $\sim 0.3$") and the effects of cloud contamination in the system. On the other hand, if indeed there is a warp, we should be able to roughly trace its location through the temperature variations it will cause and therefore, the projected emission extension variations, consequence of varying scale height. While we do observe an elevation difference in the East and West sides of the disk, apparently separated by the semi-minor axis, we have discussed that this is probably by chance and that we can't determine an exact symmetry angle, for the method used assumes symmetry with respect to the semi-major axis and this biases our results. We also show that, when tracing the deprojected border of emission (see Figure 4.11) there are two local maxima and minima radial extensions, suggesting that there is not in fact a single symmetry axis (we would have expected only one minimum and maximum extent, roughly symmetrically opposed for the case of a warp, Juhász and Facchini, 2017) and more complex processes, or a combination of effects are occurring.

If indeed a warp is responsible for the kinematic effects, there is the question of its origin. On one hand, warps are thought to arise from close-in binary interactions or inclined planetary orbits (Nealon et al., 2018; Aly and Lodato, 2020), however, warps in very young systems, possibly produced by the infall of material, have been predicted (Bate et al., 2010) and also reported (Sakai et al., 2019). In the case of Elias 2-27 we have discussed that infall may be ocurring, given the detection of large-scale emission at velocities close to the disk velocities. It is possible that, if the disk is indeed warped, this effect is caused by either a planet in an inclined orbit or infall, something that requires further investigation.

Aided by the isovelocity curves, computed from the constrained emission surface of the disk, we detect multiple deviations from Keplerian motion in the velocity cube of $^{13}$CO and C$^{18}$O, co-located with the spiral structure. The isovelocity curves themselves show a perturbed nature, given the complex emission surface, the colocation of the perturbations with the spiral structures and the strong deviations could indicate a connection between the spirals and the emitting surface morphology. Previously reported deviations for planetary companions have been of around 15 % (Pinte et al., 2018b) with respect to the channel velocity, while the perturbations we observe are much larger, reaching up to 80 % of the channel velocity for some of the features in the central channel maps. Such large perturbations increase the likelihood that they relate to the spirals, rather than to a companion, as large deviations require a large perturber mass, and in that case we would expect to see its effect in the dust emission and we do not. Furthermore, we expect deviations caused by a planet to be spatially localized (Pinte et al., 2018b, 2020, 2019) and our observations show deviations on both East and West sides of the disk, present along several channels. The detected perturbations agree with the predictions of Hall et al. (2020) in that they are co-located with the spirals and the traced morphology of the kink is similar to what was predicted in their work. If indeed the disk is warped or suffering considerable infall of material, as previously discussed, the observed "kinks" could be the product of both kinematical deviations induced by a warp and perturbations due to the spirals.

On the other hand, from the velocity profile we expect super-Keplerian velocities at large radial distances if GI is the governing process (Bertin and Lodato, 1999; Lodato, 2007). The latter is not strongly detected in our analysis (see Fig. 4.17), this could be a strong indicator for GI not being present or it could be due to: the lack of sampling at larger radial distances, lack of resolution to detect slight super-Keplerian velocities and the effects of other processes, such as infall. We do note that the East channels, especially from the $C^{18}O$ emission do show super-Keplerian velocities, however in a massive disk we would expect to see this in the whole emission.

Finally, regarding the gap found in the integrated gas emission of $C^{18}O$, we note that a gap in the gas emission is not necessarily produced by effect of a physical perturber and may answer to chemical processes of the gas or optical depth effects (see discussion in Guzmán et al. (2018)). We also show that the gap does not appear to be colocated with any perturbation in the channel maps (see Figure 4.19), which we would expect if the gap origin was planetary (e.g. Pinte et al., 2018b; Teague et al., 2018a).

## 7.3. CN Emission Analysis

The analysis of the CN molecule was aimed towards tracing the main morphological features of the emission and determining if there was any correlation between the spiral location and the emission (as predicted in chemical models (Evans et al., 2015; Ilee et al., 2017)). From the integrated emission maps we observe various features, first regarding the overall emission: at large radial distances CN emission appears only from the southern side of the disk while for the inner disk CN emission is strong roughly throughout the dust continuum radial extension. Regarding the structure: we trace two locations of lower emission at innermost radii coinciding with the NW spiral and at ∼340au, the SE spiral coincides with CN emission, however no clear spiral shape can be traced. Additionally, from the channel maps, we can see that the emission is not coming from the midplane, for upper and lower layers can be identified, especially in the West side of the disk.

The latter means that the emission from CN is probably tracing the uppermost warm molecular layer of the disk, to accurately determine the location of the emitting layer, future work must measure the excitation temperature of the observed emission, which may be done through gaussian fits in the hyperfine transition (Punzi et al., 2015). Models and observations of CN emission from the upper layer shows that rings at large radii are an expected structure (Cazzoletti et al., 2018b; van Terwisga et al., 2019), however, the strong inner-disk emission found in Elias 2-27 and the asymmetry between north/south sides is not expected. As CN emission from the upper layers is expected to trace photodissociation regions (PDRs) (Walsh et al., 2010), then a possible explanation to the lack of emission in the Northen side is that this side of the disk is being shielded from direct high energy radiation (UV or X-ray). Small dust grains may effectively block high energy radiation (Chapillon et al., 2012), and grains from infalling material will have µm sizes. If infall was occurring and affecting mostly the North side of the disk, as possibly traced by the large scale emission observed in this system, then the $\mu$m-sized particles could be shielding the northern side from UV radiation and preventing CN from forming. A warp structure, as was discussed previously, could also shield

the Northern side from direct stellar radiation.

Overall, the CN observations seem to offer further insight into the asymmetric structure and dynamics of the upper layers of Elias 2-27. We do not associate the CN emission with the disk midplane, therefore the lack of spiral features is not relevant for the discussion on the origin of the dust spiral structure. Future, detailed chemical-physical models must be conducted to accurately constrain the location from where the emission is arising and determine the origin of the marked North/South emission asymmetry.

## 7.4. Comparison with SPH simulations

We find that gravitational instabilities can accurately reproduce the spiral morphology at multiple wavelengths, with parameters close to the observational constrains, as shown in Figure 6.1. However, this still does not explain the dust gap. If the dust gap was carved by a planet, estimates indicate at best a mass of $0.1 M_J$ (Zhang et al., 2018), which is much smaller than planets expected to be formed in a GI environment. Though not shown in this work, we did run further SPH simulations of an unstable disk with different planetary-mass companions, and in all cases after a few orbits the planet migrated onto the star. Not allowing migration could allow a gap to form (see Meru et al., 2017), however it would not be a realistic scenario, which was the goal of our simulations.

In our spectral line observations we recover perturbations that are colocated with the spirals and span several channels, sharing some similarities to those predicted by Hall et al. (2020), where GI spirals produce a distinct kinematical feature co-located with spirals arms and observed over a velocity range in the channel maps. However, our gas simulations from the best-fit GI parameters does not show the perturbation features from Hall et al. (2020) when sampled and imaged with the uv-coverage of our observations. This implies that the inner perturbation observed in the $^{13}$CO and C$^{18}$O channel maps is indeed very large, as it appears at our lower angular resolution. The perturbation is seen across several channels, unlike planetary perturbations which are localized (e.g. Pinte et al., 2018b), therefore, a GI origin is coherent. The fact that we don't see the perturbation in the channel maps from simulated emission could be due to the decisions regarding the chosen time-stamp for the simulation and the position angle. As we select a specific time-frame, it is possible that at other evolutionary stages, the strength of the gas perturbations is larger. Also, it has been shown by Hall et al. (2020) that the strength of the "GI-wiggle" will vary depending on the position angle of the emission. While the inclination of the simulation matches the value of the observations (56.2°), the position angle is determined by the value that allows a good visual comparison of the simulated emission with the observations. There could be a range of position angle values that allow a good comparison with the observations and that produce stronger kinematic perturbations, this is not tested in this work.

## 7.5. Spiral Structure Origin

The hypothesis for the origin of the spiral arms observed in the dust emission of Elias 2-27 has been either gravitational instabilities or the perturbation by a companion. From the observational constrains presented in this work there are some key features that may help us define which scenario fits best the Elias 2-27 disk. To begin, however, we must state that neither option can accurately predict, on its own, both the spirals and the dust gap, as in order to reproduce the spiral arms a planetary companion would have to be located beyond the spiral extent (Meru et al., 2017) and gaps are not expected features in a disk undergoing GI, given the fast migration even massive planets will have under these conditions (Baruteau et al., 2011). The possibility of the spirals being formed by a companion seems unlikely, as has been discussed in previous studies, given the contrast, symmetry, and extent of the spirals (Forgan et al., 2018b; Bae and Zhu, 2018b). Furthermore, the possibility of an external perturber, such as a stellar companion or a fly-by causing the spiral structure, is unlikely given the non-detection of such celestial body nearby (Cieza et al., 2009; Zurlo et al., 2020) and the lack of a clear kinematical signatures in the data, as previously discussed in the case of a fly-by.

Elias 2-27 has been shown to have a large disk-to-star mass ratio (Andrews et al., 2009; Ricci et al., 2010), in this work we additionally discuss the possibility of the disk mass being up to a factor of $\sim$2 higher, if scattering is a relevant process (Zhu et al., 2019). The values of disk-to-star mass are sufficient to excite gravitational instabilities and we can accurately reproduce the spiral morphology using SPH models of a self-gravitating disk. Additionally, we detect tentative dust trapping signatures in the continuum observations and also a strong kinematic perturbation co-located with the spirals over multiple channels. The high disk mass, together with the strong deviations from keplerian motion, consistent with the kinematical prediction for a GI disk (Hall et al., 2020), lead us to signal the origin of the spirals to be gravitational instabilities, rather than a companion.

Infall of material would explain the high disk-to-star mass ratio of the system and the excitation of spiral structures due to GI (Tsukamoto et al., 2017; Hennebelle et al., 2017). While infall mechanisms are expected to be present in younger Class 0/I systems than Elias 2-27, which is classified as a Class II disk (Andrews et al., 2009), it has been proposed that Elias 2-27 could be an extremely young Class II object to explain the spiral structure (Tomida et al., 2017). Though GI can explain the spiral structure traced in the dust, there is also a clear dust gap Huang et al. (2018b), which is not a feature predicted or explained by GI. On the other hand, infall may explain on its own the perturbed morphology of the gas emission layer, but there is also a marked brightness asymmetry, which can be related to the presence of a warp in the disk (Nixon and Pringle, 2010). If the disk is warped, due to infalling material breaking the disk, this could possibly explain the dust gap observed at high angular resolution by Huang et al. (2018b), if the separation between inner and outer misaligned disks were located at $\sim$70au from the central star. Certainly further observations on the source are required, to sample shorter baselines and adequately study the dynamics of the large-scale emission, searching for infall signatures, and also observations at higher spatial resolution, to analyze the origin of the dust gap and better constrain the kinematic perturbations in the system.

# Chapter 8

# Conclusion

We present and analyze multi-wavelength dust continuum observations of the protoplanetary disk around Elias 2-27, we also study the gas emission for two different CO isotopologues and CN, providing new observational constraints on this source, with the aim of understanding the origin of the prominent spiral structure observed in the dust.

The spiral substructure is present in dust observations at multiple wavelengths, from 0.89 to 3.3mm, and shows a higher contrast at longer wavelengths. These signs are possible indicators of grain growth and dust trapping at the spiral arm location. From the spectral index analysis we find that the 0.89mm emission is optically thick and traces a layer of emission higher in the disk than the emission observed at 1.3 or 3.3mm. The spectral index from 1.3 and 3.3 mm indicates the presence of large grains in the outer disk. Furthermore, the low values of the spectral index inwards of $\sim$ 70au can be explained if this region has high optical depth and high albedo in the presence of dust scattering. This implies that the solids mass estimated under standard assumptions is likely a lower limit, and more massive disk in solids, and thus in total mass, is expected in Elias 2-27. Considering the latter constrains, we compute simple SPH simulations of a gravitationally unstable disk with parameters as those in Elias 2-27, and are able to replicate the spiral morphology at the three different wavelengths we study.

Observations of the CO isotopologues show that the gas emission is not azimuthally symmetric in the vertical direction, i.e. the disk has a larger scale height in the West than in the East at most radial distances. Additionally, at larger radial distances, the kinematic data indicates that the scale height decreases. This is the first time an azimuthal scale height difference is observed in a protoplanetary disk, and it does not appear in predictions for either a GI disk or the presence of a planetary companion. Tracing the different heights of the $^{13}$CO and C$^{18}$O emission layers we show that $^{13}$CO comes from a higher layer than C$^{18}$O, with velocities consistent with Keplerian rotation. The stellar mass we constrain ($\sim$0.5 M$_\odot$), is in agreement with the literature value (0.49M$_\odot$). Gas emission depletion (a gap) is observed in the distribution of C$^{18}$O at a radius of $\sim$240au. This gap does not appear to be co-located with the main perturbations we recognize in the channel maps. We see "kinks" or perturbations in the channel maps of both CO tracers, outside and inside the dust continuum emission. The perturbations are not coincidental with the dust or gas gap and rather appear

co-located with the spiral features and the extension of these and range across many channels. Finally, our descriptive analysis of the CN emission determines that the molecule is likely tracing the uppermost warm molecular layer of the disk, excited by high-energy radiation. There is lack of emission at large radii in the North side of the disk, which we associate with either the presence of infalling small dust grains, or shadowing effects from a warp. Future detailed chemical models will be necessary to accurately explain the data.

Given the symmetric morphology of the spirals and the signs of large grains and dust trapping from the comparison of emission at multiple wavelengths, we propose that the mechanism originating the spiral structure is GI. The latter is supported by the lack of a spatially located kinematic signature that could have been related or indicative of the presence of a planet. Based on observations that show large-scale emission surrounding and connecting to the disk, we propose the infall of material from the surrounding cloud is responsible for exciting GI in the disk, which in turn causes the dust spiral arm features. Infall of material can also explains the perturbed emission layer constrained from the gas tracers. Additionally, if infall warped the disk, this would explain the brightness asymmetry in the channel and integrated emission maps. Depending on the warp location this could also explain the dust gap observed at higher angular resolution. Further, future, observations are necessary to effectively detect the presence of a warp and confirm ongoing infall.

# Acknowledgements

This thesis makes use of the following ALMA data: ADS/JAO.ALMA#2013.1.00498.S, ADS/JAO.ALMA#2016.1.00606.S and ADS/JAO.ALMA#2017.1.00069.S. ALMA is a partnership of ESO (representing its member states), NSF (USA), and NINS (Japan), together with NRC (Canada), NSC and ASIAA (Taiwan), and KASI (Republic of Korea), in cooperation with the Republic of Chile. The Joint ALMA Observatory is operated by ESO, auI/NRAO, and NAOJ. Powered@NLHPC: This thesis was partially supported by the supercomputing infrastructure of the NLHPC (ECM-02). This project has received funding from the European Union's Horizon 2020 research and innovation program under the Marie Sklodowska-Curie grant agreement No 823823 (DUSTBUSTERS). Teresa Paneque Carreño acknowledges support and funding from FONDECYT Iniciación project #11181068, the National Aeronautics and Space Administration under grant No. 15XRP15_20140 issued through the Exoplanets Research Program, FCFM/U. de Chile Fondo de Instalación Académica, CONICYT project Basal AFB-170002 and SOCHIAS grant through ALMA/CONICYT Project 31170021.

# Bibliography

Rachel L. Akeson, Eric L. N. Jensen, John Carpenter, Luca Ricci, Stefan Laos, Natasha F. Nogueira, and Emma M. Suen-Lewis. Resolved Young Binary Systems and Their Disks. , 872(2):158, February 2019. doi: 10.3847/1538-4357/aaff6a.

Eiji Akiyama, Jun Hashimoto, Hauyu Baobab Liu, Jennifer I-Hsiu Li, Michael Bonnefoy, Ruobing Dong, Yasuhiro Hasegawa, Thomas Henning, Michael L. Sitko, Markus Janson, Markus Feldt, John Wisniewski, Tomoyuki Kudo, Nobuhiko Kusakabe, Takashi Tsukagoshi, Munetake Momose, Takayuki Muto, Tetsuo Taki, Masayuki Kuzuhara, Mayama Satoshi, Michihiro Takami, Nagayoshi Ohashi, Carol A. Grady, Jungmi Kwon, Christian Thalmann, Lyu Abe, Wolfgang Brandner, Timothy D. Brand t, Joseph C. Carson, Sebastian Egner, Miwa Goto, Olivier Guyon, Yutaka Hayano, Masahiko Hayashi, Saeko S. Hayashi, Klaus W. Hodapp, Miki Ishii, Masanori Iye, Gillian R. Knapp, Ryo Kand ori, Taro Matsuo, Michael W. Mcelwain, Shoken Miyama, Jun-Ichi Morino, Amaya Moro-Martin, Tetsuo Nishimura, Tae-Soo Pyo, Eugene Serabyn, Takuya Suenaga, Hiroshi Suto, Ryuji Suzuki, Yasuhiro H. Takahashi, Naruhisa Takato, Hiroshi Terada, Daigo Tomono, Edwin L. Turner, Makoto Watanabe, Toru Yamada, Hideki Takami, Tomonori Usuda, and Motohide Tamura. Spiral Structure and Differential Dust Size Distribution in the LKH$\alpha$ 330 Disk. , 152(6):222, December 2016. doi: 10.3847/1538-3881/152/6/222.

ALMA Partnership, C. L. Brogan, L. M. Pérez, T. R. Hunter, W. R. F. Dent, A. S. Hales, R. E. Hills, S. Corder, E. B. Fomalont, C. Vlahakis, Y. Asaki, D. Barkats, A. Hirota, J. A. Hodge, C. M. V. Impellizzeri, R. Kneissl, E. Liuzzo, R. Lucas, N. Marcelino, S. Matsushita, K. Nakanishi, N. Phillips, A. M. S. Richards, I. Toledo, R. Aladro, D. Broguiere, J. R. Cortes, P. C. Cortes, D. Espada, F. Galarza, D. Garcia-Appadoo, L. Guzman-Ramirez, E. M. Humphreys, T. Jung, S. Kameno, R. A. Laing, S. Leon, G. Marconi, A. Mignano, B. Nikolic, L. A. Nyman, M. Radiszcz, A. Remijan, J. A. Rodón, T. Sawada, S. Takahashi, R. P. J. Tilanus, B. Vila Vilaro, L. C. Watson, T. Wiklind, E. Akiyama, E. Chapillon, I. de Gregorio-Monsalvo, J. Di Francesco, F. Gueth, A. Kawamura, C. F. Lee, Q. Nguyen Luong, J. Mangum, V. Pietu, P. Sanhueza, K. Saigo, S. Takakuwa, C. Ubach, T. van Kempen, A. Wootten, A. Castro-Carrizo, H. Francke, J. Gallardo, J. Garcia, S. Gonzalez, T. Hill, T. Kaminski, Y. Kurono, H. Y. Liu, C. Lopez, F. Morales, K. Plarre, G. Schieven, L. Testi, L. Videla, E. Villard, P. Andreani, J. E. Hibbard, and K. Tatematsu. The 2014 ALMA Long Baseline Campaign: First Results from High Angular Resolution Observations toward the HL Tau Region. , 808(1):L3, July 2015. doi: 10.1088/2041-8205/808/1/L3.

Hossam Aly and Giuseppe Lodato. Efficient dust ring formation in misaligned circumbinary discs. , 492(3):3306–3315, March 2020. doi: 10.1093/mnras/stz3633.

Sean M. Andrews. Observations of Solids in Protoplanetary Disks. , 127(956):961, October 2015. doi: 10.1086/683178.

Sean M. Andrews. Observations of Protoplanetary Disk Structures. *arXiv e-prints*, art. arXiv:2001.05007, January 2020.

Sean M. Andrews, D. J. Wilner, A. M. Hughes, Chunhua Qi, and C. P. Dullemond. Protoplanetary Disk Structures in Ophiuchus. , 700(2):1502–1523, August 2009. doi: 10.1088/0004-637X/700/2/1502.

Sean M. Andrews, Katherine A. Rosenfeld, Adam L. Kraus, and David J. Wilner. The Mass Dependence between Protoplanetary Disks and their Stellar Hosts. , 771(2):129, July 2013. doi: 10.1088/0004-637X/771/2/129.

Sean M. Andrews, Jane Huang, Laura M. Pérez, Andrea Isella, Cornelis P. Dullemond, Nicolás T. Kurtovic, Viviana V. Guzmán, John M. Carpenter, David J. Wilner, Shangjia Zhang, Zhaohuan Zhu, Tilman Birnstiel, Xue-Ning Bai, Myriam Benisty, A. Meredith Hughes, Karin I. Öberg, and Luca Ricci. The Disk Substructures at High Angular Resolution Project (DSHARP). I. Motivation, Sample, Calibration, and Overview. , 869(2):L41, December 2018a. doi: 10.3847/2041-8213/aaf741.

Sean M. Andrews, Marie Terrell, Anjali Tripathi, Megan Ansdell, Jonathan P. Williams, and David J. Wilner. Scaling Relations Associated with Millimeter Continuum Sizes in Protoplanetary Disks. , 865(2):157, October 2018b. doi: 10.3847/1538-4357/aadd9f.

M. Ansdell, J. P. Williams, N. van der Marel, J. M. Carpenter, G. Guidi, M. Hogerheijde, G. S. Mathews, C. F. Manara, A. Miotello, A. Natta, I. Oliveira, M. Tazzari, L. Testi, E. F. van Dishoeck, and S. E. van Terwisga. ALMA Survey of Lupus Protoplanetary Disks. I. Dust and Gas Masses. , 828(1):46, September 2016. doi: 10.3847/0004-637X/828/1/46.

M. Ansdell, J. P. Williams, L. Trapman, S. E. van Terwisga, S. Facchini, C. F. Manara, N. van der Marel, A. Miotello, M. Tazzari, M. Hogerheijde, G. Guidi, L. Testi, and E. F. van Dishoeck. ALMA Survey of Lupus Protoplanetary Disks. II. Gas Disk Radii. , 859(1): 21, May 2018. doi: 10.3847/1538-4357/aab890.

Philip J. Armitage. Physical processes in protoplanetary disks. *arXiv e-prints*, art. arXiv:1509.06382, September 2015.

Jaehan Bae and Zhaohuan Zhu. Planet-driven Spiral Arms in Protoplanetary Disks. I. Formation Mechanism. , 859(2):118, June 2018a. doi: 10.3847/1538-4357/aabf8c.

Jaehan Bae and Zhaohuan Zhu. Planet-driven Spiral Arms in Protoplanetary Disks. II. Implications. , 859(2):119, June 2018b. doi: 10.3847/1538-4357/aabf93.

Jaehan Bae, Zhaohuan Zhu, and Lee Hartmann. On the Formation of Multiple Concentric Rings and Gaps in Protoplanetary Disks. , 850(2):201, December 2017. doi: 10.3847/1538-4357/aa9705.

G. Ballabio, G. Dipierro, B. Veronesi, G. Lodato, M. Hutchison, G. Laibe, and D. J. Price. Enforcing dust mass conservation in 3D simulations of tightly coupled grains with the PHANTOM SPH code. , 477(2):2766–2771, June 2018. doi: 10.1093/mnras/sty642.

Scott A. Barenfeld, John M. Carpenter, Anneila I. Sargent, Andrea Isella, and Luca Ricci. Measurement of Circumstellar Disk Sizes in the Upper Scorpius OB Association with

ALMA. , 851(2):85, December 2017. doi: 10.3847/1538-4357/aa989d.

Clément Baruteau, Farzana Meru, and Sijme-Jan Paardekooper. Rapid inward migration of planets formed by gravitational instability. , 416(3):1971–1982, September 2011. doi: 10.1111/j.1365-2966.2011.19172.x.

M. R. Bate, G. Lodato, and J. E. Pringle. Chaotic star formation and the alignment of stellar rotation with disc and planetary orbital axes. , 401(3):1505–1513, January 2010. doi: 10.1111/j.1365-2966.2009.15773.x.

Matthew R. Bate, Ian A. Bonnell, and Nigel M. Price. Modelling accretion in protobinary systems. , 277(2):362–376, November 1995. doi: 10.1093/mnras/277.2.362.

Steven V. W. Beckwith, Anneila I. Sargent, Rolf S. Chini, and Rolf Guesten. A Survey for Circumstellar Disks around Young Stellar Objects. , 99:924, March 1990. doi: 10.1086/115385.

M. Benisty, A. Juhasz, A. Boccaletti, H. Avenhaus, J. Milli, C. Thalmann, C. Dominik, P. Pinilla, E. Buenzli, A. Pohl, J. L. Beuzit, T. Birnstiel, J. de Boer, M. Bonnefoy, G. Chauvin, V. Christiaens, A. Garufi, C. Grady, T. Henning, N. Huelamo, A. Isella, M. Langlois, F. Ménard, D. Mouillet, J. Olofsson, E. Pantin, C. Pinte, and L. Pueyo. Asymmetric features in the protoplanetary disk MWC 758. , 578:L6, June 2015. doi: 10.1051/0004-6361/201526011.

M. Benisty, T. Stolker, A. Pohl, J. de Boer, G. Lesur, C. Dominik, C. P. Dullemond, M. Langlois, M. Min, K. Wagner, T. Henning, A. Juhasz, P. Pinilla, S. Facchini, D. Apai, R. van Boekel, A. Garufi, C. Ginski, F. Ménard, C. Pinte, S. P. Quanz, A. Zurlo, A. Boccaletti, M. Bonnefoy, J. L. Beuzit, G. Chauvin, M. Cudel, S. Desidera, M. Feldt, C. Fontanive, R. Gratton, M. Kasper, A. M. Lagrange, H. LeCoroller, D. Mouillet, D. Mesa, E. Sissa, A. Vigan, J. Antichi, T. Buey, T. Fusco, D. Gisler, M. Llored, Y. Magnard, O. Moeller-Nilsson, J. Pragt, R. Roelfsema, J. F. Sauvage, and F. Wildi. Shadows and spirals in the protoplanetary disk HD 100453. , 597:A42, January 2017. doi: 10.1051/0004-6361/201629798.

M. Benisty, A. Juhász, S. Facchini, P. Pinilla, J. de Boer, L. M. Pérez, M. Keppler, G. Muro-Arena, M. Villenave, S. Andrews, C. Dominik, C. P. Dullemond, A. Gallenne, A. Garufi, C. Ginski, and A. Isella. Shadows and asymmetries in the T Tauri disk HD 143006: evidence for a misaligned inner disk. , 619:A171, November 2018. doi: 10.1051/0004-6361/201833913.

G. Bertin and G. Lodato. A class of self-gravitating accretion disks. , 350:694–704, October 1999.

T. Birnstiel, C. P. Dullemond, and P. Pinilla. Lopsided dust rings in transition disks. , 550:L8, February 2013. doi: 10.1051/0004-6361/201220847.

T. Birnstiel, M. Fang, and A. Johansen. Dust Evolution and the Formation of Planetesimals. , 205(1-4):41–75, December 2016. doi: 10.1007/s11214-016-0256-1.

Y. Boehler, A. Dutrey, S. Guilloteau, and V. Piétu. Probing dust settling in proto-planetary discs with ALMA. , 431(2):1573–1586, May 2013. doi: 10.1093/mnras/stt278.

A. P. Boss. Giant planet formation by gravitational instability. *Science*, 276:1836–1839, January 1997. doi: 10.1126/science.276.5320.1836.

Nuria Calvet, Alberto Patino, Gladis C. Magris, and Paola D'Alessio. Irradiation of Accretion Disks around Young Objects. I. Near-Infrared CO Bands. , 380:617, October 1991. doi: 10.1086/170618.

Simon Casassus, Chris M. Wright, Sebastian Marino, Sarah T. Maddison, Al Wootten, Pablo Roman, Sebastian Pérez, Paola Pinilla, Mark Wyatt, Victor Moral, Francois Ménard, Valentin Christiaens, Lucas Cieza, and Gerrit van der Plas. A Compact Concentration of Large Grains in the HD 142527 Protoplanetary Dust Trap. , 812(2):126, October 2015. doi: 10.1088/0004-637X/812/2/126.

Simon Casassus, Sebastián Marino, Wladimir Lyra, Clément Baruteau, Matías Vidal, Alwyn Wootten, Sebastián Pérez, Felipe Alarcon, Marcelo Barraza, Miguel Cárcamo, Ruobing Dong, Anibal Sierra, Zhaohuan Zhu, Luca Ricci, Valentin Christiaens, and Lucas Cieza. Cm-wavelength observations of MWC 758: resolved dust trapping in a vortex. , 483(3): 3278–3287, March 2019. doi: 10.1093/mnras/sty3269.

P. Cazzoletti, E. F. van Dishoeck, P. Pinilla, M. Tazzari, S. Facchini, N. van der Marel, M. Benisty, A. Garufi, and L. M. Pérez. Evidence for a massive dust-trapping vortex connected to spirals. Multi-wavelength analysis of the HD 135344B protoplanetary disk. , 619:A161, November 2018a. doi: 10.1051/0004-6361/201834006.

P. Cazzoletti, E. F. van Dishoeck, R. Visser, S. Facchini, and S. Bruderer. CN rings in full protoplanetary disks around young stars as probes of disk structure. , 609:A93, January 2018b. doi: 10.1051/0004-6361/201731457.

E. Chapillon, S. Guilloteau, A. Dutrey, V. Piétu, and M. Guélin. Chemistry in disks. VI. CN and HCN in protoplanetary disks. , 537:A60, January 2012. doi: 10.1051/0004-6361/201116762.

E. I. Chiang and P. Goldreich. Spectral Energy Distributions of T Tauri Stars with Passive Circumstellar Disks. , 490(1):368–376, November 1997. doi: 10.1086/304869.

V. Christiaens, S. Casassus, S. Perez, G. van der Plas, and F. Ménard. Spiral Arms in the Disk of HD 142527 from CO Emission Lines with ALMA. , 785(1):L12, April 2014. doi: 10.1088/2041-8205/785/1/L12.

Lucas A. Cieza, Deborah L. Padgett, Lori E. Allen, Caer E. McCabe, Timothy Y. Brooke, Sean J. Carey, Nicholas L. Chapman, Misato Fukagawa, Tracy L. Huard, Alberto Noriga-Crespo, Dawn E. Peterson, and Luisa M. Rebull. Primordial Circumstellar Disks in Binary Systems: Evidence for Reduced Lifetimes. , 696(1):L84–L88, May 2009. doi: 10.1088/0004-637X/696/1/L84.

Lucas A. Cieza, Dary Ruíz-Rodríguez, Antonio Hales, Simon Casassus, Sebastian Pérez, Camilo Gonzalez-Ruilova, Hector Cánovas, Jonathan P. Williams, Alice Zurlo, Megan Ansdell, Henning Avenhaus, Amelia Bayo, Gesa H. M. Bertrang, Valentin Christiaens, William Dent, Gabriel Ferrero, Roberto Gamen, Johan Olofsson, Santiago Orcajo, Karla Peña Ramírez, David Principe, Matthias R. Schreiber, and Gerrit van der Plas. The Ophiuchus DIsc Survey Employing ALMA (ODISEA) - I: project description and continuum images at 28 au resolution. , 482(1):698–714, January 2019. doi: 10.1093/mnras/sty2653.

Peter Cossins, Giuseppe Lodato, and C. J. Clarke. Characterizing the gravitational instability in cooling accretion discs. , 393(4):1157–1173, March 2009. doi: 10.1111/j.1365-2966.2008.14275.x.

Nicolás Cuello, Giovanni Dipierro, Daniel Mentiplay, Daniel J. Price, Christophe Pinte, Jorge Cuadra, Guillaume Laibe, François Ménard, Pedro P. Poblete, and Matías Montesinos. Flybys in protoplanetary discs: I. Gas and dust dynamics. , 483(3):4114–4139, March 2019. doi: 10.1093/mnras/sty3325.

Nicolás Cuello, Fabien Louvet, Daniel Mentiplay, Christophe Pinte, Daniel J. Price, Andrew J. Winter, Rebecca Nealon, François Ménard, Giuseppe Lodato, Giovanni Dipierro, Valentin Christiaens, Matías Montesinos, Jorge Cuadra, Guillaume Laibe, Lucas Cieza, Ruobing Dong, and Richard Alexander. Flybys in protoplanetary discs - II. Observational signatures. , 491(1):504–514, January 2020. doi: 10.1093/mnras/stz2938.

Paola D'Alessio, Jorge Cantö, Nuria Calvet, and Susana Lizano. Accretion Disks around Young Objects. I. The Detailed Vertical Structure. , 500(1):411–427, June 1998. doi: 10.1086/305702.

M. de Val-Borro, R. G. Edgar, P. Artymowicz, P. Ciecielag, P. Cresswell, G. D'Angelo, E. J. Delgado-Donate, G. Dirksen, S. Fromang, A. Gawryszczak, H. Klahr, W. Kley, W. Lyra, F. Masset, G. Mellema, R. P. Nelson, S. J. Paardekooper, A. Peplinski, A. Pierens, T. Plewa, K. Rice, C. Schäfer, and R. Speith. A comparative study of disc-planet interaction. , 370(2):529–558, August 2006. doi: 10.1111/j.1365-2966.2006.10488.x.

G. Dipierro, G. Lodato, L. Testi, and I. de Gregorio Monsalvo. How to detect the signatures of self-gravitating circumstellar discs with the Atacama Large Millimeter/sub-millimeter Array. , 444(2):1919–1929, October 2014. doi: 10.1093/mnras/stu1584.

Giovanni Dipierro, Paola Pinilla, Giuseppe Lodato, and Leonardo Testi. Dust trapping by spiral arms in gravitationally unstable protostellar discs. , 451(1):974–986, July 2015. doi: 10.1093/mnras/stv970.

Giovanni Dipierro, Guillaume Laibe, Richard Alexander, and Mark Hutchison. Gas and multispecies dust dynamics in viscous protoplanetary discs: the importance of the dust back-reaction. , 479(3):4187–4206, September 2018. doi: 10.1093/mnras/sty1701.

Ruobing Dong, Cassandra Hall, Ken Rice, and Eugene Chiang. Spiral Arms in Gravitationally Unstable Protoplanetary Disks as Imaged in Scattered Light. , 812(2):L32, October 2015a. doi: 10.1088/2041-8205/812/2/L32.

Ruobing Dong, Zhaohuan Zhu, Roman R. Rafikov, and James M. Stone. Observational Signatures of Planets in Protoplanetary Disks: Spiral Arms Observed in Scattered Light Imaging Can be Induced by Planets. , 809(1):L5, August 2015b. doi: 10.1088/2041-8205/809/1/L5.

Ruobing Dong, Sheng-yuan Liu, Josh Eisner, Sean Andrews, Jeffrey Fung, Zhaohuan Zhu, Eugene Chiang, Jun Hashimoto, Hauyu Baobab Liu, Simon Casassus, Thomas Esposito, Yasuhiro Hasegawa, Takayuki Muto, Yaroslav Pavlyuchenkov, David Wilner, Eiji Akiyama, Motohide Tamura, and John Wisniewski. The Eccentric Cavity, Triple Rings, Two-armed Spirals, and Double Clumps of the MWC 758 Disk. , 860(2):124, June 2018. doi: 10.3847/1538-4357/aac6cb.

B. T. Draine. On the Submillimeter Opacity of Protoplanetary Disks. , 636(2):1114–1120, January 2006. doi: 10.1086/498130.

B. T. Draine and H. M. Lee. Optical Properties of Interstellar Graphite and Silicate Grains.

, 285:89, October 1984. doi: 10.1086/162480.

A. Dutrey, D. Semenov, E. Chapillon, U. Gorti, S. Guilloteau, F. Hersant, M. Hogerheijde, M. Hughes, G. Meeus, H. Nomura, V. Piétu, C. Qi, and V. Wakelam. Physical and Chemical Structure of Planet-Forming Disks Probed by Millimeter Observations and Modeling. In Henrik Beuther, Ralf S. Klessen, Cornelis P. Dullemond, and Thomas Henning, editors, *Protostars and Planets VI*, page 317, January 2014. doi: 10.2458/azu_uapress_9780816531240-ch014.

Barbara Ercolano and Ilaria Pascucci. The dispersal of planet-forming discs: theory confronts observations. *Royal Society Open Science*, 4(4):170114, April 2017. doi: 10.1098/rsos.170114.

II Evans, Neal J., Michael M. Dunham, Jes K. Jørgensen, Melissa L. Enoch, Bruno Merín, Ewine F. van Dishoeck, Juan M. Alcalá, Philip C. Myers, Karl R. Stapelfeldt, Tracy L. Huard, Lori E. Allen, Paul M. Harvey, Tim van Kempen, Geoffrey A. Blake, David W. Koerner, Lee G. Mundy, Deborah L. Padgett, and Anneila I. Sargent. The Spitzer c2d Legacy Results: Star-Formation Rates and Efficiencies; Evolution and Lifetimes. , 181(2):321–350, April 2009. doi: 10.1088/0067-0049/181/2/321.

M. G. Evans, J. D. Ilee, A. C. Boley, P. Caselli, R. H. Durisen, T. W. Hartquist, and J. M. C. Rawlings. Gravitational instabilities in a protosolar-like disc - I. Dynamics and chemistry. , 453(2):1147–1163, October 2015. doi: 10.1093/mnras/stv1698.

Stefano Facchini, Attila Juhász, and Giuseppe Lodato. Signatures of broken protoplanetary discs in scattered light and in sub-millimetre observations. , 473(4):4459–4475, February 2018. doi: 10.1093/mnras/stx2523.

Daniel Foreman-Mackey, Will Farr, Manodeep Sinha, Anne Archibald, David Hogg, Jeremy Sanders, Joe Zuntz, Peter Williams, Andrew Nelson, Miguel de Val-Borro, Tobias Erhardt, Ilya Pashchenko, and Oriol Pla. emcee v3: A Python ensemble sampling toolkit for affine-invariant MCMC. *The Journal of Open Source Software*, 4(43):1864, November 2019. doi: 10.21105/joss.01864.

D. H. Forgan, C. Hall, F. Meru, and W. K. M. Rice. Towards a population synthesis model of self-gravitating disc fragmentation and tidal downsizing II: the effect of fragment-fragment interactions. , 474(4):5036–5048, March 2018a. doi: 10.1093/mnras/stx2870.

Duncan H. Forgan, John D. Ilee, and Farzana Meru. Are Elias 2-27's Spiral Arms Driven by Self-gravity, or by a Companion? A Comparative Spiral Morphology Study. , 860(1):L5, June 2018b. doi: 10.3847/2041-8213/aac7c9.

M. A. Frerking, W. D. Langer, and R. W. Wilson. The relationship between carbon monoxide abundance and visual extinction in interstellar clouds. , 262:590–605, November 1982. doi: 10.1086/160451.

Gaia Collaboration, A. G. A. Brown, A. Vallenari, T. Prusti, J. H. J. de Bruijne, C. Babusiaux, C. A. L. Bailer-Jones, M. Biermann, D. W. Evans, L. Eyer, F. Jansen, C. Jordi, S. A. Klioner, U. Lammers, L. Lindegren, X. Luri, F. Mignard, C. Panem, D. Pourbaix, S. Randich, P. Sartoretti, H. I. Siddiqui, C. Soubiran, F. van Leeuwen, N. A. Walton, F. Arenou, U. Bastian, M. Cropper, R. Drimmel, D. Katz, M. G. Lattanzi, J. Bakker, C. Cacciari, J. Castañeda, L. Chaoul, N. Cheek, F. De Angeli, C. Fabricius, R. Guerra, B. Holl, E. Masana, R. Messineo, N. Mowlavi, K. Nienartowicz, P. Panuzzo, J. Portell, M. Rie-

llo, G. M. Seabroke, P. Tanga, F. Thévenin, G. Gracia-Abril, G. Comoretto, M. Garcia-Reinaldos, D. Teyssier, M. Altmann, R. Andrae, M. Audard, I. Bellas-Velidis, K. Benson, J. Berthier, R. Blomme, P. Burgess, G. Busso, B. Carry, A. Cellino, G. Clementini, M. Clotet, O. Creevey, M. Davidson, J. De Ridder, L. Delchambre, A. Dell'Oro, C. Ducourant, J. Fernández-Hernández, M. Fouesneau, Y. Frémat, L. Galluccio, M. García-Torres, J. González-Núñez, J. J. González-Vidal, E. Gosset, L. P. Guy, J. L. Halbwachs, N. C. Hambly, D. L. Harrison, J. Hernández, D. Hestroffer, S. T. Hodgkin, A. Hutton, G. Jasniewicz, A. Jean-Antoine-Piccolo, S. Jordan, A. J. Korn, A. Krone-Martins, A. C. Lanzafame, T. Lebzelter, W. Löffler, M. Manteiga, P. M. Marrese, J. M. Martín-Fleitas, A. Moitinho, A. Mora, K. Muinonen, J. Osinde, E. Pancino, T. Pauwels, J. M. Petit, A. Recio-Blanco, P. J. Richards, L. Rimoldini, A. C. Robin, L. M. Sarro, C. Siopis, M. Smith, A. Sozzetti, M. Süveges, J. Torra, W. van Reeven, U. Abbas, A. Abreu Aramburu, S. Accart, C. Aerts, G. Altavilla, M. A. Álvarez, R. Alvarez, J. Alves, R. I. Anderson, A. H. Andrei, E. Anglada Varela, E. Antiche, T. Antoja, B. Arcay, T. L. Astraatmadja, N. Bach, S. G. Baker, L. Balaguer-Núñez, P. Balm, C. Barache, C. Barata, D. Barbato, F. Barblan, P. S. Barklem, D. Barrado, M. Barros, M. A. Barstow, S. Bartholomé Muñoz, J. L. Bassilana, U. Becciani, M. Bellazzini, A. Berihuete, S. Bertone, L. Bianchi, O. Bienaymé, S. Blanco-Cuaresma, T. Boch, C. Boeche, A. Bombrun, R. Borrachero, D. Bossini, S. Bouquillon, G. Bourda, A. Bragaglia, L. Bramante, M. A. Breddels, A. Bressan, N. Brouillet, T. Brüsemeister, E. Brugaletta, B. Bucciarelli, A. Burlacu, D. Busonero, A. G. Butkevich, R. Buzzi, E. Caffau, R. Cancelliere, G. Cannizzaro, T. Cantat-Gaudin, R. Carballo, T. Carlucci, J. M. Carrasco, L. Casamiquela, M. Castellani, A. Castro-Ginard, P. Charlot, L. Chemin, A. Chiavassa, G. Cocozza, G. Costigan, S. Cowell, F. Crifo, M. Crosta, C. Crowley, J. Cuypers, C. Dafonte, Y. Damerdji, A. Dapergolas, P. David, M. David, P. de Laverny, F. De Luise, R. De March, D. de Martino, R. de Souza, A. de Torres, J. Debosscher, E. del Pozo, M. Delbo, A. Delgado, H. E. Delgado, P. Di Matteo, S. Diakite, C. Diener, E. Distefano, C. Dolding, P. Drazinos, J. Durán, B. Edvardsson, H. Enke, K. Eriksson, P. Esquej, G. Eynard Bontemps, C. Fabre, M. Fabrizio, S. Faigler, A. J. Falcão, M. Farràs Casas, L. Federici, G. Fedorets, P. Fernique, F. Figueras, F. Filippi, K. Findeisen, A. Fonti, E. Fraile, M. Fraser, B. Frézouls, M. Gai, S. Galleti, D. Garabato, F. García-Sedano, A. Garofalo, N. Garralda, A. Gavel, P. Gavras, J. Gerssen, R. Geyer, P. Giacobbe, G. Gilmore, S. Girona, G. Giuffrida, F. Glass, M. Gomes, M. Granvik, A. Gueguen, A. Guerrier, J. Guiraud, R. Gutiérrez-Sánchez, R. Haigron, D. Hatzidimitriou, M. Hauser, M. Haywood, U. Heiter, A. Helmi, J. Heu, T. Hilger, D. Hobbs, W. Hofmann, G. Holland, H. E. Huckle, A. Hypki, V. Icardi, K.ßen@, G. Jevardat de Fombelle, P. G. Jonker, Á. L. Juhász, F. Julbe, A. Karampelas, A. Kewley, J. Klar, A. Kochoska, R. Kohley, K. Kolenberg, M. Kontizas, E. Kontizas, S. E. Koposov, G. Kordopatis, Z. Kostrzewa-Rutkowska, P. Koubsky, S. Lambert, A. F. Lanza, Y. Lasne, J. B. Lavigne, Y. Le Fustec, C. Le Poncin-Lafitte, Y. Lebreton, S. Leccia, N. Leclerc, I. Lecoeur-Taibi, H. Lenhardt, F. Leroux, S. Liao, E. Licata, H. E. P. Lindstrøm, T. A. Lister, E. Livanou, A. Lobel, M. López, S. Managau, R. G. Mann, G. Mantelet, O. Marchal, J. M. Marchant, M. Marconi, S. Marinoni, G. Marschalkó, D. J. Marshall, M. Martino, G. Marton, N. Mary, D. Massari, G. Matijevič, T. Mazeh, P. J. McMillan, S. Messina, D. Michalik, N. R. Millar, D. Molina, R. Molinaro, L. Molnár, P. Montegriffo, R. Mor, R. Morbidelli, T. Morel, D. Morris, A. F. Mulone, T. Muraveva, I. Musella, G. Nelemans, L. Nicastro, L. Noval, W. O'Mullane, C. Ordénovic, D. Ordóñez-Blanco, P. Osborne, C. Pagani, I. Pagano, F. Pailler, H. Palacin, L. Palaversa, A. Panahi, M. Pawlak, A. M. Piersimoni, F. X. Pineau, E. Plachy, G. Plum, E. Poggio, E. Poujoulet,

A. Prša, L. Pulone, E. Racero, S. Ragaini, N. Rambaux, M. Ramos-Lerate, S. Regibo, C. Reylé, F. Riclet, V. Ripepi, A. Riva, A. Rivard, G. Rixon, T. Roegiers, M. Roelens, M. Romero-Gómez, N. Rowell, F. Royer, L. Ruiz-Dern, G. Sadowski, T. Sagristà Sellés, J. Sahlmann, J. Salgado, E. Salguero, N. Sanna, T. Santana-Ros, M. Sarasso, H. Savietto, M. Schultheis, E. Sciacca, M. Segol, J. C. Segovia, D. Ségransan, I. C. Shih, L. Siltala, A. F. Silva, R. L. Smart, K. W. Smith, E. Solano, F. Solitro, R. Sordo, S. Soria Nieto, J. Souchay, A. Spagna, F. Spoto, U. Stampa, I. A. Steele, H. Steidelmüller, C. A. Stephenson, H. Stoev, F. F. Suess, J. Surdej, L. Szabados, E. Szegedi-Elek, D. Tapiador, F. Taris, G. Tauran, M. B. Taylor, R. Teixeira, D. Terrett, P. Teyssand ier, W. Thuillot, A. Titarenko, F. Torra Clotet, C. Turon, A. Ulla, E. Utrilla, S. Uzzi, M. Vaillant, G. Valentini, V. Valette, A. van Elteren, E. Van Hemelryck, M. van Leeuwen, M. Vaschetto, A. Vecchiato, J. Veljanoski, Y. Viala, D. Vicente, S. Vogt, C. von Essen, H. Voss, V. Votruba, S. Voutsinas, G. Walmsley, M. Weiler, O. Wertz, T. Wevers, L. Wyrzykowski, A. Yoldas, M. Žerjal, H. Ziaeepour, J. Zorec, S. Zschocke, S. Zucker, C. Zurbach, and T. Zwitter. Gaia Data Release 2. Summary of the contents and survey properties. , 616:A1, August 2018. doi: 10.1051/0004-6361/201833051.

C. F. Gammie. Nonlinear Outcome of Gravitational Instability in Cooling, Gaseous Disks. , 553:174–183, May 2001. doi: 10.1086/320631.

A. Garufi, M. Benisty, P. Pinilla, M. Tazzari, C. Dominik, C. Ginski, Th. Henning, Q. Kral, M. Langlois, F. Ménard, T. Stolker, J. Szulagyi, M. Villenave, and G. van der Plas. Evolution of protoplanetary disks from their taxonomy in scattered light: spirals, rings, cavities, and shadows. , 620:A94, December 2018. doi: 10.1051/0004-6361/201833872.

P. Goldreich and S. Tremaine. The excitation of density waves at the Lindblad and corotation resonances by an external potential. , 233:857–871, November 1979. doi: 10.1086/157448.

Jonathan Goodman and Jonathan Weare. Ensemble samplers with affine invariance. *Communications in Applied Mathematics and Computational Science*, 5(1):65–80, January 2010. doi: 10.2140/camcos.2010.5.65.

C. A. Grady, T. Muto, J. Hashimoto, M. Fukagawa, T. Currie, B. Biller, C. Thalmann, M. L. Sitko, R. Russell, J. Wisniewski, R. Dong, J. Kwon, S. Sai, J. Hornbeck, G. Schneider, D. Hines, A. Moro Martín, M. Feldt, Th. Henning, J. U. Pott, M. Bonnefoy, J. Bouwman, S. Lacour, A. Mueller, A. Juhász, A. Crida, G. Chauvin, S. Andrews, D. Wilner, A. Kraus, S. Dahm, T. Robitaille, H. Jang-Condell, L. Abe, E. Akiyama, W. Brandner, T. Brandt, J. Carson, S. Egner, K. B. Follette, M. Goto, O. Guyon, Y. Hayano, M. Hayashi, S. Hayashi, K. Hodapp, M. Ishii, M. Iye, M. Janson, R. Kandori, G. Knapp, T. Kudo, N. Kusakabe, M. Kuzuhara, S. Mayama, M. McElwain, T. Matsuo, S. Miyama, J. I. Morino, T. Nishimura, T. S. Pyo, G. Serabyn, H. Suto, R. Suzuki, M. Takami, N. Takato, H. Terada, D. Tomono, E. Turner, M. Watanabe, T. Yamada, H. Takami, T. Usuda, and M. Tamura. Spiral Arms in the Asymmetrically Illuminated Disk of MWC 758 and Constraints on Giant Planets. , 762(1):48, January 2013. doi: 10.1088/0004-637X/762/1/48.

S. F. Gull and G. J. Daniell. Image reconstruction from incomplete and noisy data. , 272 (5655):686–690, April 1978. doi: 10.1038/272686a0.

Viviana V. Guzmán, Jane Huang, Sean M. Andrews, Andrea Isella, Laura M. Pérez, John M. Carpenter, Cornelis P. Dullemond, Luca Ricci, Tilman Birnstiel, Shangjia Zhang, Zhaohuan Zhu, Xue-Ning Bai, Myriam Benisty, Karin I. Öberg, and David J. Wilner.

The Disk Substructures at High Angular Resolution Program (DSHARP). VIII. The Rich Ringed Substructures in the AS 209 Disk. , 869(2):L48, December 2018. doi: 10.3847/2041-8213/aaedae.

C. Hall, R. Dong, R. Teague, J. Terry, C. Pinte, T. Paneque-Carreño, B. Veronesi, R. D. Alexand er, and G. Lodato. Predicting the kinematic evidence of gravitational instability. *arXiv e-prints*, art. arXiv:2007.15686, July 2020.

Cassandra Hall, Duncan Forgan, Ken Rice, Tim J. Harries, Pamela D. Klaassen, and Beth Biller. Directly observing continuum emission from self-gravitating spiral waves. , 458(1): 306–318, May 2016. doi: 10.1093/mnras/stw296.

Cassandra Hall, Duncan Forgan, and Ken Rice. Identifying and analysing protostellar disc fragments in smoothed particle hydrodynamics simulations. , 470(3):2517–2538, September 2017. doi: 10.1093/mnras/stx1244.

Cassandra Hall, Ken Rice, Giovanni Dipierro, Duncan Forgan, Tim Harries, and Richard Alexander. Is the spiral morphology of the Elias 2-27 circumstellar disc due to gravitational instability? , 477(1):1004–1014, June 2018. doi: 10.1093/mnras/sty550.

Cassandra Hall, Ruobing Dong, Ken Rice, Tim J. Harries, Joan Najita, Richard Alexander, and Sean Brittain. The Temporal Requirements of Directly Observing Self-gravitating Spiral Waves in Protoplanetary Disks with ALMA. , 871(2):228, February 2019. doi: 10.3847/1538-4357/aafac2.

D. Harsono, R. D. Alexander, and Y. Levin. Global gravitational instabilities in discs with infall. , 413(1):423–433, May 2011. doi: 10.1111/j.1365-2966.2010.18146.x.

Patrick Hennebelle, Geoffroy Lesur, and Sébastien Fromang. Spiral-driven accretion in protoplanetary discs . III. Tridimensional simulations. , 599:A86, March 2017. doi: 10.1051/0004-6361/201629779.

J. A. Högbom. Aperture Synthesis with a Non-Regular Distribution of Interferometer Baselines. , 15:417, June 1974.

Jane Huang, Sean M. Andrews, L. Ilsedore Cleeves, Karin I. Öberg, David J. Wilner, Xuening Bai, Til Birnstiel, John Carpenter, A. Meredith Hughes, Andrea Isella, Laura M. Pérez, Luca Ricci, and Zhaohuan Zhu. CO and Dust Properties in the TW Hya Disk from High-resolution ALMA Observations. , 852(2):122, January 2018a. doi: 10.3847/1538-4357/aaa1e7.

Jane Huang, Sean M. Andrews, Cornelis P. Dullemond, Andrea Isella, Laura M. Pérez, Viviana V. Guzmán, Karin I. Öberg, Zhaohuan Zhu, Shangjia Zhang, Xue-Ning Bai, Myriam Benisty, Tilman Birnstiel, John M. Carpenter, A. Meredith Hughes, Luca Ricci, Erik Weaver, and David J. Wilner. The Disk Substructures at High Angular Resolution Project (DSHARP). II. Characteristics of Annular Substructures. , 869(2):L42, December 2018b. doi: 10.3847/2041-8213/aaf740.

Jane Huang, Sean M. Andrews, Laura M. Pérez, Zhaohuan Zhu, Cornelis P. Dullemond, Andrea Isella, Myriam Benisty, Xue-Ning Bai, Tilman Birnstiel, John M. Carpenter, Viviana V. Guzmán, A. Meredith Hughes, Karin I. Öberg, Luca Ricci, David J. Wilner, and Shangjia Zhang. The Disk Substructures at High Angular Resolution Project (DSHARP). III. Spiral Structures in the Millimeter Continuum of the Elias 27, IM Lup, and WaOph 6

Disks. , 869(2):L43, December 2018c. doi: 10.3847/2041-8213/aaf7a0.

J. D. Ilee, A. C. Boley, P. Caselli, R. H. Durisen, T. W. Hartquist, and J. M. C. Rawlings. Chemistry in a gravitationally unstable protoplanetary disc. , 417(4):2950–2961, November 2011. doi: 10.1111/j.1365-2966.2011.19455.x.

J. D. Ilee, D. H. Forgan, M. G. Evans, C. Hall, R. Booth, C. J. Clarke, W. K. M. Rice, A. C. Boley, P. Caselli, T. W. Hartquist, and J. M. C. Rawlings. The chemistry of protoplanetary fragments formed via gravitational instabilities. , 472(1):189–204, November 2017. doi: 10.1093/mnras/stx1966.

Andrea Isella, John M. Carpenter, and Anneila I. Sargent. Structure and Evolution of Pre-main-sequence Circumstellar Disks. , 701(1):260–282, August 2009. doi: 10.1088/0004-637X/701/1/260.

A. Johansen, A. Youdin, and H. Klahr. Zonal Flows and Long-lived Axisymmetric Pressure Bumps in Magnetorotational Turbulence. , 697(2):1269–1289, June 2009. doi: 10.1088/0004-637X/697/2/1269.

A. Juhász, M. Benisty, A. Pohl, C. P. Dullemond, C. Dominik, and S. J. Paardekooper. Spiral arms in scattered light images of protoplanetary discs: are they the signposts of planets? , 451(2):1147–1157, August 2015. doi: 10.1093/mnras/stv1045.

Attila Juhász and Stefano Facchini. Observational signatures of linear warps in circumbinary discs. , 466(4):4053–4073, April 2017. doi: 10.1093/mnras/stw3389.

Attila Juhász and Giovanni P. Rosotti. Spiral arms in thermally stratified protoplanetary discs. , 474(1):L32–L36, February 2018. doi: 10.1093/mnrasl/slx182.

M. Kama, S. Bruderer, E. F. van Dishoeck, M. Hogerheijde, C. P. Folsom, A. Miotello, D. Fedele, A. Belloche, R. Güsten, and F. Wyrowski. Volatile-carbon locking and release in protoplanetary disks. A study of TW Hya and HD 100546. , 592:A83, August 2016. doi: 10.1051/0004-6361/201526991.

H. H. Klahr and P. Bodenheimer. Turbulence in Accretion Disks: Vorticity Generation and Angular Momentum Transport via the Global Baroclinic Instability. , 582(2):869–892, January 2003. doi: 10.1086/344743.

Hubert Klahr and Peter Bodenheimer. Formation of Giant Planets by Concurrent Accretion of Solids and Gas inside an Anticyclonic Vortex. , 639(1):432–440, March 2006. doi: 10.1086/498928.

Kaitlin Kratter and Giuseppe Lodato. Gravitational Instabilities in Circumstellar Disks. , 54:271–311, September 2016. doi: 10.1146/annurev-astro-081915-023307.

S. Krijt, C. W. Ormel, C. Dominik, and A. G. G. M. Tielens. Erosion and the limits to planetesimal growth. , 574:A83, February 2015. doi: 10.1051/0004-6361/201425222.

Nicolás T. Kurtovic, Laura M. Pérez, Myriam Benisty, Zhaohuan Zhu, Shangjia Zhang, Jane Huang, Sean M. Andrews, Cornelis P. Dullemond, Andrea Isella, Xue-Ning Bai, John M. Carpenter, Viviana V. Guzmán, Luca Ricci, and David J. Wilner. The Disk Substructures at High Angular Resolution Project (DSHARP). IV. Characterizing Substructures and Interactions in Disks around Multiple Star Systems. , 869(2):L44, December 2018. doi: 10.3847/2041-8213/aaf746.

Charles J. Lada. Star formation: from OB associations to protostars. In Manuel Peimbert and Jun Jugaku, editors, *Star Forming Regions*, volume 115 of *IAU Symposium*, page 1, January 1987.

Guillaume Laibe and Daniel J. Price. Dusty gas with smoothed particle hydrodynamics - I. Algorithm and test suite. , 420(3):2345–2364, March 2012a. doi: 10.1111/j.1365-2966.2011.20202.x.

Guillaume Laibe and Daniel J. Price. Dusty gas with smoothed particle hydrodynamics - II. Implicit timestepping and astrophysical drag regimes. , 420(3):2365–2376, March 2012b. doi: 10.1111/j.1365-2966.2011.20201.x.

Y. Y. Lau and G. Bertin. Discrete spiral modes, spiral waves, and the local dispersion relationship. , 226:508–520, December 1978. doi: 10.1086/156635.

Geoffroy Lesur, Patrick Hennebelle, and Sébastien Fromang. Spiral-driven accretion in protoplanetary discs. I. 2D models. , 582:L9, October 2015. doi: 10.1051/0004-6361/201526734.

Hauyu Baobab Liu. The Anomalously Low (Sub)Millimeter Spectral Indices of Some Protoplanetary Disks May Be Explained By Dust Self-scattering. , 877(2):L22, June 2019. doi: 10.3847/2041-8213/ab1f8e.

G. Lodato. Self-gravitating accretion discs. *Nuovo Cimento Rivista Serie*, 30:293, January 2007. doi: 10.1393/ncr/i2007-10022-x.

G. Lodato and W. K. M. Rice. Testing the locality of transport in self-gravitating accretion discs - II. The massive disc case. , 358(4):1489–1500, April 2005. doi: 10.1111/j.1365-2966.2005.08875.x.

Giuseppe Lodato and Daniel J. Price. On the diffusive propagation of warps in thin accretion discs. , 405(2):1212–1226, June 2010. doi: 10.1111/j.1365-2966.2010.16526.x.

Feng Long, Gregory J. Herczeg, Ilaria Pascucci, Dániel Apai, Thomas Henning, Carlo F. Manara, Gijs D. Mulders, László. SzHucs, and Nathanial P. Hendler. An ALMA Survey of Faint Disks in the Chamaeleon I Star-forming Region: Why Are Some Class II Disks so Faint? , 863(1):61, August 2018a. doi: 10.3847/1538-4357/aacce9.

Feng Long, Paola Pinilla, Gregory J. Herczeg, Daniel Harsono, Giovanni Dipierro, Ilaria Pascucci, Nathan Hendler, Marco Tazzari, Enrico Ragusa, Colette Salyk, Suzan Edwards, Giuseppe Lodato, Gerrit van de Plas, Doug Johnstone, Yao Liu, Yann Boehler, Sylvie Cabrit, Carlo F. Manara, Francois Menard, Gijs D. Mulders, Brunella Nisini, William J. Fischer, Elisabetta Rigliaco, Andrea Banzatti, Henning Avenhaus, and Michael Gully-Santiago. Gaps and Rings in an ALMA Survey of Disks in the Taurus Star-forming Region. , 869(1):17, December 2018b. doi: 10.3847/1538-4357/aae8e1.

R. V. E. Lovelace, H. Li, S. A. Colgate, and A. F. Nelson. Rossby Wave Instability of Keplerian Accretion Disks. , 513(2):805–810, March 1999. doi: 10.1086/306900.

K. L. Luhman and G. H. Rieke. Low-Mass Star Formation and the Initial Mass Function in the $\rho$ Ophiuchi Cloud Core. , 525(1):440–465, November 1999. doi: 10.1086/307891.

D. Lynden-Bell and J. E. Pringle. The evolution of viscous discs and the origin of the nebular variables. , 168:603–637, September 1974. doi: 10.1093/mnras/168.3.603.

W. Lyra, A. Johansen, H. Klahr, and N. Piskunov. Standing on the shoulders of giants.

Trojan Earths and vortex trapping in low mass self-gravitating protoplanetary disks of gas and solids. , 493(3):1125–1139, January 2009. doi: 10.1051/0004-6361:200810797.

Enrique Macías, Catherine C. Espaillat, Mayra Osorio, Guillem Anglada, José M. Torrelles, Carlos Carrasco-González, Mario Flock, Hendrik Linz, Gesa H. M. Bertrang, Thomas Henning, José F. Gómez, Nuria Calvet, and William R. F. Dent. Characterization of Ring Substructures in the Protoplanetary Disk of HD 169142 from Multiwavelength Atacama Large Millimeter/submillimeter Array Observations. , 881(2):159, August 2019. doi: 10.3847/1538-4357/ab31a2.

S. Marino, S. Perez, and S. Casassus. Shadows Cast by a Warp in the HD 142527 Protoplanetary Disk. , 798(2):L44, January 2015. doi: 10.1088/2041-8205/798/2/L44.

M. K. McClure and C. Dominik. Measuring the atomic composition of planetary building blocks. *arXiv e-prints*, art. arXiv:1910.07345, October 2019.

J. P. McMullin, B. Waters, D. Schiebel, W. Young, and K. Golap. CASA Architecture and Applications. In R. A. Shaw, F. Hill, and D. J. Bell, editors, *Astronomical Data Analysis Software and Systems XVI*, volume 376 of *Astronomical Society of the Pacific Conference Series*, page 127, October 2007.

Farzana Meru, Attila Juhász, John D. Ilee, Cathie J. Clarke, Giovanni P. Rosotti, and Richard A. Booth. On the Origin of the Spiral Morphology in the Elias 2-27 Circumstellar Disk. , 839(2):L24, April 2017. doi: 10.3847/2041-8213/aa6837.

T. Muto, C. A. Grady, J. Hashimoto, M. Fukagawa, J. B. Hornbeck, M. Sitko, R. Russell, C. Werren, M. Curé, T. Currie, N. Ohashi, Y. Okamoto, M. Momose, M. Honda, S. Inutsuka, T. Takeuchi, R. Dong, L. Abe, W. Brandner, T. Brandt, J. Carson, S. Egner, M. Feldt, T. Fukue, M. Goto, O. Guyon, Y. Hayano, M. Hayashi, S. Hayashi, T. Henning, K. W. Hodapp, M. Ishii, M. Iye, M. Janson, R. Kandori, G. R. Knapp, T. Kudo, N. Kusakabe, M. Kuzuhara, T. Matsuo, S. Mayama, M. W. McElwain, S. Miyama, J. I. Morino, A. Moro-Martin, T. Nishimura, T. S. Pyo, E. Serabyn, H. Suto, R. Suzuki, M. Takami, N. Takato, H. Terada, C. Thalmann, D. Tomono, E. L. Turner, M. Watanabe, J. P. Wisniewski, T. Yamada, H. Takami, T. Usuda, and M. Tamura. Discovery of Small-scale Spiral Structures in the Disk of SAO 206462 (HD 135344B): Implications for the Physical State of the Disk from Spiral Density Wave Theory. , 748(2):L22, April 2012. doi: 10.1088/2041-8205/748/2/L22.

Y. Nakagawa, M. Sekiya, and C. Hayashi. Settling and growth of dust particles in a laminar phase of a low-mass solar nebula. , 67(3):375–390, September 1986. doi: 10.1016/0019-1035(86)90121-1.

Sergei Nayakshin. Formation of planets by tidal downsizing of giant planet embryos. , 408 (1):L36–L40, October 2010. doi: 10.1111/j.1745-3933.2010.00923.x.

Rebecca Nealon, Giovanni Dipierro, Richard Alexander, Rebecca G. Martin, and Chris Nixon. Warping a protoplanetary disc with a planet on an inclined orbit. , 481(1):20–35, November 2018. doi: 10.1093/mnras/sty2267.

C. J. Nixon and J. E. Pringle. The observable effects of tidally induced warps in protostellar discs. , 403(4):1887–1893, April 2010. doi: 10.1111/j.1365-2966.2010.16331.x.

G. I. Ogilvie and S. H. Lubow. On the wake generated by a planet in a disc. , 330(4):950–954,

March 2002. doi: 10.1046/j.1365-8711.2002.05148.x.

I. Pascucci, L. Testi, G. J. Herczeg, F. Long, C. F. Manara, N. Hendler, G. D. Mulders, S. Krijt, F. Ciesla, Th. Henning, S. Mohanty, E. Drabek-Maunder, D. Apai, L.Hucs@ Sz-Hucs, G. Sacco, and J. Olofsson. A Steeper than Linear Disk Mass-Stellar Mass Scaling Relation. , 831(2):125, November 2016. doi: 10.3847/0004-637X/831/2/125.

Laura M. Pérez, John M. Carpenter, Sean M. Andrews, Luca Ricci, Andrea Isella, Hendrik Linz, Anneila I. Sargent, David J. Wilner, Thomas Henning, Adam T. Deller, Claire J. Chandler, Cornelis P. Dullemond, Joseph Lazio, Karl M. Menten, Stuartt A. Corder, Shaye Storm, Leonardo Testi, Marco Tazzari, Woojin Kwon, Nuria Calvet, Jane S. Greaves, Robert J. Harris, and Lee G. Mundy. Spiral density waves in a young protoplanetary disk. *Science*, 353(6307):1519–1521, September 2016. doi: 10.1126/science.aaf8296.

Laura M. Pérez, Myriam Benisty, Sean M. Andrews, Andrea Isella, Cornelis P. Dullemond, Jane Huang, Nicolás T. Kurtovic, Viviana V. Guzmán, Zhaohuan Zhu, Tilman Birnstiel, Shangjia Zhang, John M. Carpenter, David J. Wilner, Luca Ricci, Xue-Ning Bai, Erik Weaver, and Karin I. Öberg. The Disk Substructures at High Angular Resolution Project (DSHARP). X. Multiple Rings, a Misaligned Inner Disk, and a Bright Arc in the Disk around the T Tauri star HD 143006. , 869(2):L50, December 2018a. doi: 10.3847/2041-8213/aaf745.

Sebastian Perez, A. Dunhill, S. Casassus, P. Roman, J. Szulágyi, C. Flores, S. Marino, and M. Montesinos. Planet Formation Signposts: Observability of Circumplanetary Disks via Gas Kinematics. , 811(1):L5, September 2015. doi: 10.1088/2041-8205/811/1/L5.

Sebastián Pérez, S. Casassus, and P. Benítez-Llambay. Observability of planet-disc interactions in CO kinematics. , 480(1):L12–L17, October 2018b. doi: 10.1093/mnrasl/sly109.

Sebastián Pérez, Simon Casassus, Antonio Hales, Sebastián Marino, Anthony Cheetham, Alice Zurlo, Lucas Cieza, Ruobing Dong, Felipe Alarcón, Pablo Benítez-Llambay, Ed Fomalont, and Henning Avenhaus. Long Baseline Observations of the HD 100546 Protoplanetary Disk with ALMA. , 889(1):L24, January 2020. doi: 10.3847/2041-8213/ab6b2b.

Alex R. Pettitt, Clare L. Dobbs, David M. Acreman, and Daniel J. Price. The morphology of the Milky Way - I. Reconstructing CO maps from simulations in fixed potentials. , 444 (1):919–941, October 2014. doi: 10.1093/mnras/stu1075.

P. Pinilla, T. Birnstiel, L. Ricci, C. P. Dullemond, A. L. Uribe, L. Testi, and A. Natta. Trapping dust particles in the outer regions of protoplanetary disks. , 538:A114, February 2012. doi: 10.1051/0004-6361/201118204.

P. Pinilla, L. M. Pérez, S. Andrews, N. van der Marel, E. F. van Dishoeck, S. Ataiee, M. Benisty, T. Birnstiel, A. Juhász, A. Natta, L. Ricci, and L. Testi. A Multi-wavelength Analysis of Dust and Gas in the SR 24S Transition Disk. , 839(2):99, April 2017. doi: 10.3847/1538-4357/aa6973.

C. Pinte, F. Ménard, G. Duchêne, and P. Bastien. Monte Carlo radiative transfer in protoplanetary disks. , 459(3):797–804, December 2006. doi: 10.1051/0004-6361:20053275.

C. Pinte, T. J. Harries, M. Min, A. M. Watson, C. P. Dullemond, P. Woitke, F. Ménard, and M. C. Durán-Rojas. Benchmark problems for continuum radiative transfer. High optical depths, anisotropic scattering, and polarisation. , 498(3):967–980, May 2009. doi:

10.1051/0004-6361/200811555.

C. Pinte, F. Ménard, G. Duchêne, T. Hill, W. R. F. Dent, P. Woitke, S. Maret, G. van der Plas, A. Hales, I. Kamp, W. F. Thi, I. de Gregorio-Monsalvo, C. Rab, S. P. Quanz, H. Avenhaus, A. Carmona, and S. Casassus. Direct mapping of the temperature and velocity gradients in discs. Imaging the vertical CO snow line around IM Lupi. , 609:A47, January 2018a. doi: 10.1051/0004-6361/201731377.

C. Pinte, D. J. Price, F. Ménard, G. Duchêne, W. R. F. Dent, T. Hill, I. de Gregorio-Monsalvo, A. Hales, and D. Mentiplay. Kinematic Evidence for an Embedded Protoplanet in a Circumstellar Disk. , 860(1):L13, June 2018b. doi: 10.3847/2041-8213/aac6dc.

C. Pinte, G. van der Plas, F. Ménard, D. J. Price, V. Christiaens, T. Hill, D. Mentiplay, C. Ginski, E. Choquet, Y. Boehler, G. Duchêne, S. Perez, and S. Casassus. Kinematic detection of a planet carving a gap in a protoplanetary disk. *Nature Astronomy*, 3:1109–1114, August 2019. doi: 10.1038/s41550-019-0852-6.

C. Pinte, D. J. Price, F. Ménard, G. Duchêne, V. Christiaens, S. M. Andrews, J. Huang, T. Hill, G. van der Plas, L. M. Perez, A. Isella, Y. Boehler, W. R. F. Dent, D. Mentiplay, and R. A. Loomis. Nine Localized Deviations from Keplerian Rotation in the DSHARP Circumstellar Disks: Kinematic Evidence for Protoplanets Carving the Gaps. , 890(1):L9, February 2020. doi: 10.3847/2041-8213/ab6dda.

D. J. Price. Smoothed Particle Hydrodynamics: Things I Wish My Mother Taught Me. In R. Capuzzo-Dolcetta, M. Limongi, and A. Tornambè, editors, *Advances in Computational Astrophysics: Methods, Tools, and Outcome*, volume 453 of *Astronomical Society of the Pacific Conference Series*, page 249, July 2012.

Daniel J. Price and Guillaume Laibe. A fast and explicit algorithm for simulating the dynamics of small dust grains with smoothed particle hydrodynamics. , 451(1):813–826, July 2015. doi: 10.1093/mnras/stv996.

Daniel J. Price, James Wurster, Terrence S. Tricco, Chris Nixon, Stéven Toupin, Alex Pettitt, Conrad Chan, Daniel Mentiplay, Guillaume Laibe, Simon Glover, Clare Dobbs, Rebecca Nealon, David Liptai, Hauke Worpel, Clément Bonnerot, Giovanni Dipierro, Giulia Ballabio, Enrico Ragusa, Christoph Federrath, Roberto Iaconi, Thomas Reichardt, Duncan Forgan, Mark Hutchison, Thomas Constantino, Ben Ayliffe, Kieran Hirsh, and Giuseppe Lodato. Phantom: A Smoothed Particle Hydrodynamics and Magnetohydrodynamics Code for Astrophysics. , 35:e031, September 2018. doi: 10.1017/pasa.2018.25.

K. M. Punzi, P. Hily-Blant, J. H. Kastner, G. G. Sacco, and T. Forveille. An Unbiased 1.3 mm Emission Line Survey of the Protoplanetary Disk Orbiting LkCa 15. , 805(2):147, June 2015. doi: 10.1088/0004-637X/805/2/147.

L. Ricci, L. Testi, A. Natta, and K. J. Brooks. Dust grain growth in $\rho$-Ophiuchi protoplanetary disks. , 521:A66, October 2010. doi: 10.1051/0004-6361/201015039.

Ken Rice. The Evolution of Self-Gravitating Accretion Discs. , 33:e012, March 2016. doi: 10.1017/pasa.2016.12.

Ken Rice, Eric Lopez, Duncan Forgan, and Beth Biller. Disc fragmentation rarely forms planetary-mass objects. , 454(2):1940–1947, December 2015. doi: 10.1093/mnras/stv1997.

W. K. M. Rice, G. Lodato, J. E. Pringle, P. J. Armitage, and I. A. Bonnell. Accelerated

planetesimal growth in self-gravitating protoplanetary discs. , 355(2):543–552, December 2004. doi: 10.1111/j.1365-2966.2004.08339.x.

W. K. M. Rice, Philip J. Armitage, Kenneth Wood, and G. Lodato. Dust filtration at gap edges: implications for the spectral energy distributions of discs with embedded planets. , 373(4):1619–1626, December 2006. doi: 10.1111/j.1365-2966.2006.11113.x.

Samuel Richard, Richard P. Nelson, and Orkan M. Umurhan. Vortex formation in protoplanetary discs induced by the vertical shear instability. , 456(4):3571–3584, March 2016. doi: 10.1093/mnras/stv2898.

Katherine A. Rosenfeld, Sean M. Andrews, A. Meredith Hughes, David J. Wilner, and Chunhua Qi. A Spatially Resolved Vertical Temperature Gradient in the HD 163296 Disk. , 774(1):16, September 2013. doi: 10.1088/0004-637X/774/1/16.

G. P. Rosotti, M. Benisty, A. Juhász, R. Teague, C. Clarke, C. Dominik, C. P. Dullemond, P. D. Klaassen, L. Matrà, and T. Stolker. Spiral arms in the protoplanetary disc HD100453 detected with ALMA: evidence for binary-disc interaction and a vertical temperature gradient. , 491(1):1335–1347, January 2020. doi: 10.1093/mnras/stz3090.

D. Ruíz-Rodríguez, L. A. Cieza, J. P. Williams, S. M. Andrews, D. A. Principe, C. Caceres, H. Canovas, S. Casassus, M. R. Schreiber, and J. H. Kastner. ALMA survey of circumstellar discs in the young stellar cluster IC 348. , 478(3):3674–3692, August 2018. doi: 10.1093/mnras/sty1351.

Nami Sakai, Tomoyuki Hanawa, Yichen Zhang, Aya E. Higuchi, Satoshi Ohashi, Yoko Oya, and Satoshi Yamamoto. A warped disk around an infant protostar. , 565(7738):206–208, January 2019. doi: 10.1038/s41586-018-0819-2.

Anibal Sierra and Susana Lizano. Effects of Scattering, Temperature Gradients, and Settling on the Derived Dust Properties of Observed Protoplanetary Disks. , 892(2):136, April 2020. doi: 10.3847/1538-4357/ab7d32.

Jacob B. Simon and Philip J. Armitage. Efficiency of Particle Trapping in the Outer Regions of Protoplanetary Disks. , 784(1):15, March 2014. doi: 10.1088/0004-637X/784/1/15.

Volker Springel, Naoki Yoshida, and Simon D. M. White. GADGET: a code for collisionless and gasdynamical cosmological simulations. , 6(2):79–117, April 2001. doi: 10.1016/S1384-1076(01)00042-2.

Tomas Stolker, Mike Sitko, Bernard Lazareff, Myriam Benisty, Carsten Dominik, Rens Waters, Michiel Min, Sebastian Perez, Julien Milli, Antonio Garufi, Jozua de Boer, Christian Ginski, Stefan Kraus, Jean-Philippe Berger, and Henning Avenhaus. Variable Dynamics in the Inner Disk of HD 135344B Revealed with Multi-epoch Scattered Light Imaging. , 849(2):143, November 2017. doi: 10.3847/1538-4357/aa886a.

Clément Surville, Lucio Mayer, and Douglas N. C. Lin. Dust Capture and Long-lived Density Enhancements Triggered by Vortices in 2D Protoplanetary Disks. , 831(1):82, November 2016. doi: 10.3847/0004-637X/831/1/82.

Sanemichi Z. Takahashi and Takayuki Muto. Structure Formation in a Young Protoplanetary Disk by a Magnetic Disk Wind. , 865(2):102, October 2018. doi: 10.3847/1538-4357/aadda0.

Y. Wen Tang, S. Guilloteau, V. Piétu, A. Dutrey, N. Ohashi, and P. T. P. Ho. The circumstellar disk of AB Aurigae: evidence for envelope accretion at late stages of star formation? , 547:A84, November 2012. doi: 10.1051/0004-6361/201219414.

Marco Tazzari, Frederik Beaujean, and Leonardo Testi. GALARIO: a GPU accelerated library for analysing radio interferometer observations. , 476(4):4527–4542, June 2018. doi: 10.1093/mnras/sty409.

Richard Teague. eddy: Extracting Protoplanetary Disk Dynamics with Python. *The Journal of Open Source Software*, 4(34):1220, February 2019. doi: 10.21105/joss.01220.

Richard Teague and Daniel Foreman-Mackey. bettermoments: Line-of-sight velocity calculation, January 2019.

Richard Teague, Jaehan Bae, Edwin A. Bergin, Tilman Birnstiel, and Daniel Foreman-Mackey. A Kinematical Detection of Two Embedded Jupiter-mass Planets in HD 163296. , 860(1):L12, June 2018a. doi: 10.3847/2041-8213/aac6d7.

Richard Teague, Jaehan Bae, Tilman Birnstiel, and Edwin A. Bergin. Evidence for a Vertical Dependence on the Pressure Structure in AS 209. , 868(2):113, December 2018b. doi: 10.3847/1538-4357/aae836.

Richard Teague, Jaehan Bae, Jane Huang, and Edwin A. Bergin. Spiral Structure in the Gas Disk of TW Hya. , 884(2):L56, October 2019. doi: 10.3847/2041-8213/ab4a83.

Jens Teiser and Gerhard Wurm. High-velocity dust collisions: forming planetesimals in a fragmentation cascade with final accretion. , 393(4):1584–1594, March 2009. doi: 10.1111/j.1365-2966.2008.14289.x.

S. Terebey, F. H. Shu, and P. Cassen. The collapse of the cores of slowly rotating isothermal clouds. , 286:529–551, November 1984. doi: 10.1086/162628.

L. Testi, T. Birnstiel, L. Ricci, S. Andrews, J. Blum, J. Carpenter, C. Dominik, A. Isella, A. Natta, J. P. Williams, and D. J. Wilner. Dust Evolution in Protoplanetary Disks. In Henrik Beuther, Ralf S. Klessen, Cornelis P. Dullemond, and Thomas Henning, editors, *Protostars and Planets VI*, page 339, January 2014. doi: 10.2458/azu_uapress_9780816531240-ch015.

A. Richard Thompson, James M. Moran, and Jr. Swenson, George W. *Interferometry and Synthesis in Radio Astronomy, 3rd Edition*. 2017. doi: 10.1007/978-3-319-44431-4.

John J. Tobin, Leslie W. Looney, David J. Wilner, Woojin Kwon, Claire J. Chandler, Tyler L. Bourke, Laurent Loinard, Hsin-Fang Chiang, Scott Schnee, and Xuepeng Chen. A Sub-arcsecond Survey Toward Class 0 Protostars in Perseus: Searching for Signatures of Protostellar Disks. , 805(2):125, June 2015. doi: 10.1088/0004-637X/805/2/125.

Kengo Tomida, Masahiro N. Machida, Takashi Hosokawa, Yuya Sakurai, and Chia Hui Lin. Grand-design Spiral Arms in a Young Forming Circumstellar Disk. , 835(1):L11, January 2017. doi: 10.3847/2041-8213/835/1/L11.

A. Toomre. On the gravitational stability of a disk of stars. , 139:1217–1238, May 1964. doi: 10.1086/147861.

Takashi Tsukagoshi, Hideko Nomura, Takayuki Muto, Ryohei Kawabe, Daiki Ishimoto, Kazuhiro D. Kanagawa, Satoshi Okuzumi, Shigeru Ida, Catherine Walsh, and T. J. Millar. A

Gap with a Deficit of Large Grains in the Protoplanetary Disk around TW Hya. , 829(2): L35, October 2016. doi: 10.3847/2041-8205/829/2/L35.

Y. Tsukamoto, S. Okuzumi, and A. Kataoka. Apparent Disk-mass Reduction and Planetisimal Formation in Gravitationally Unstable Disks in Class 0/I Young Stellar Objects. , 838(2):151, April 2017. doi: 10.3847/1538-4357/aa6081.

N. J. Turner, S. Fromang, C. Gammie, H. Klahr, G. Lesur, M. Wardle, and X. N. Bai. Transport and Accretion in Planet-Forming Disks. In Henrik Beuther, Ralf S. Klessen, Cornelis P. Dullemond, and Thomas Henning, editors, *Protostars and Planets VI*, page 411, January 2014. doi: 10.2458/azu_uapress_9780816531240-ch018.

A. L. Uribe, H. Klahr, M. Flock, and Th. Henning. Three-dimensional Magnetohydrodynamic Simulations of Planet Migration in Turbulent Stratified Disks. , 736(2):85, August 2011. doi: 10.1088/0004-637X/736/2/85.

N. van der Marel, P. Pinilla, J. Tobin, T. van Kempen, S. Andrews, L. Ricci, and T. Birnstiel. A Concentration of Centimeter-sized Grains in the Ophiuchus IRS 48 Dust Trap. , 810(1): L7, September 2015. doi: 10.1088/2041-8205/810/1/L7.

Nienke van der Marel. *Mind the gap: gas and dust in planet-forming disks*. PhD thesis, Leiden University, September 2015.

Nienke van der Marel, Ewine F. van Dishoeck, Simon Bruderer, Til Birnstiel, Paola Pinilla, Cornelis P. Dullemond, Tim A. van Kempen, Markus Schmalzl, Joanna M. Brown, Gregory J. Herczeg, Geoffrey S. Mathews, and Vincent Geers. A Major Asymmetric Dust Trap in a Transition Disk. *Science*, 340(6137):1199–1202, June 2013. doi: 10.1126/science.1236770.

S. E. van Terwisga, E. F. van Dishoeck, P. Cazzoletti, S. Facchini, L. Trapman, J. P. Williams, C. F. Manara, A. Miotello, N. van der Marel, M. Ansdell, M. R. Hogerheijde, M. Tazzari, and L. Testi. The ALMA Lupus protoplanetary disk survey: evidence for compact gas disks and molecular rings from CN. , 623:A150, March 2019. doi: 10.1051/0004-6361/201834257.

A. Vigan, M. Bonavita, B. Biller, D. Forgan, K. Rice, G. Chauvin, S. Desidera, J. C. Meunier, P. Delorme, J. E. Schlieder, M. Bonnefoy, J. Carson, E. Covino, J. Hagelberg, T. Henning, M. Janson, A. M. Lagrange, S. P. Quanz, A. Zurlo, J. L. Beuzit, A. Boccaletti, E. Buenzli, M. Feldt, J. H. V. Girard, R. Gratton, M. Kasper, H. Le Coroller, D. Mesa, S. Messina, M. Meyer, G. Montagnier, C. Mordasini, D. Mouillet, C. Moutou, M. Reggiani, D. Segransan, and C. Thalmann. The VLT/NaCo large program to probe the occurrence of exoplanets and brown dwarfs at wide orbits. IV. Gravitational instability rarely forms wide, giant planets. , 603:A3, June 2017. doi: 10.1051/0004-6361/201630133.

A. Vigan, C. Fontanive, M. Meyer, B. Biller, M. Bonavita, M. Feldt, S. Desidera, G. D. Marleau, A. Emsenhuber, R. Galicher, K. Rice, D. Forgan, C. Mordasini, R. Gratton, H. Le Coroller, A. L. Maire, F. Cantalloube, G. Chauvin, A. Cheetham, J. Hagelberg, A. M. Lagrange, M. Langlois, M. Bonnefoy, J. L. Beuzit, A. Boccaletti, V. D'Orazi, P. Delorme, C. Dominik, Th. Henning, M. Janson, E. Lagadec, C. Lazzoni, R. Ligi, F. Menard, D. Mesa, S. Messina, C. Moutou, A. Müller, C. Perrot, M. Samland, H. M. Schmid, T. Schmidt, E. Sissa, M. Turatto, S. Udry, A. Zurlo, L. Abe, J. Antichi, R. Asensio-Torres, A. Baruffolo, P. Baudoz, J. Baudrand, A. Bazzon, P. Blanchard, A. J. Bohn, S. Brown Sevilla, M. Carbillet, M. Carle, E. Cascone, J. Charton, R. Claudi, A. Costille, V. De Caprio, A. Delboulbé,

K. Dohlen, N. Engler, D. Fantinel, P. Feautrier, T. Fusco, P. Gigan, J. H. Girard, E. Giro, D. Gisler, L. Gluck, C. Gry, N. Hubin, E. Hugot, M. Jaquet, M. Kasper, D. Le Mignant, M. Llored, F. Madec, Y. Magnard, P. Martinez, D. Maurel, O. Möller-Nilsson, D. Mouillet, T. Moulin, A. Origné, A. Pavlov, D. Perret, C. Petit, J. Pragt, P. Puget, P. Rabou, J. Ramos, E. L. Rickman, F. Rigal, S. Rochat, R. Roelfsema, G. Rousset, A. Roux, B. Salasnich, J. F. Sauvage, A. Sevin, C. Soenke, E. Stadler, M. Suarez, Z. Wahhaj, L. Weber, and F. Wildi. The SPHERE infrared survey for exoplanets (SHINE). III. The demographics of young giant exoplanets below 300 au with SPHERE. *arXiv e-prints*, art. arXiv:2007.06573, July 2020.

Catherine Walsh, T. J. Millar, and Hideko Nomura. Chemical Processes in Protoplanetary Disks. , 722(2):1607–1623, October 2010. doi: 10.1088/0004-637X/722/2/1607.

Catherine Walsh, Cail Daley, Stefano Facchini, and Attila Juhász. CO emission tracing a warp or radial flow within $\lesssim$100 au in the HD 100546 protoplanetary disk. , 607:A114, November 2017. doi: 10.1051/0004-6361/201731334.

S. J. Weidenschilling. Aerodynamics of solid bodies in the solar nebula. , 180:57–70, July 1977. doi: 10.1093/mnras/180.1.57.

F. L. Whipple. On certain aerodynamic processes for asteroids and comets. In Aina Elvius, editor, *From Plasma to Planet*, page 211, January 1972.

Jonathan P. Williams and Lucas A. Cieza. Protoplanetary Disks and Their Evolution. , 49 (1):67–117, September 2011. doi: 10.1146/annurev-astro-081710-102548.

Jonathan P. Williams, Lucas Cieza, Antonio Hales, Megan Ansdell, Dary Ruiz-Rodriguez, Simon Casassus, Sebastian Perez, and Alice Zurlo. The Ophiuchus DIsk Survey Employing ALMA (ODISEA): Disk Dust Mass Distributions across Protostellar Evolutionary Classes. , 875(2):L9, April 2019. doi: 10.3847/2041-8213/ab1338.

James Wurster, Daniel J. Price, and Matthew R. Bate. Can non-ideal magnetohydrodynamics solve the magnetic braking catastrophe? , 457(1):1037–1061, March 2016. doi: 10.1093/mnras/stw013.

Ke Zhang, Edwin A. Bergin, Geoffrey A. Blake, L. Ilsedore Cleeves, Michiel Hogerheijde, Vachail Salinas, and Kamber R. Schwarz. On the Commonality of 10-30 AU Sized Axisymmetric Dust Structures in Protoplanetary Disks. , 818(1):L16, February 2016. doi: 10.3847/2041-8205/818/1/L16.

Shangjia Zhang and Zhaohuan Zhu. The effects of disc self-gravity and radiative cooling on the formation of gaps and spirals by young planets. , 493(2):2287–2305, April 2020. doi: 10.1093/mnras/staa404.

Shangjia Zhang, Zhaohuan Zhu, Jane Huang, Viviana V. Guzmán, Sean M. Andrews, Tilman Birnstiel, Cornelis P. Dullemond, John M. Carpenter, Andrea Isella, Laura M. Pérez, Myriam Benisty, David J. Wilner, Clément Baruteau, Xue-Ning Bai, and Luca Ricci. The Disk Substructures at High Angular Resolution Project (DSHARP). VII. The Planet-Disk Interactions Interpretation. , 869(2):L47, December 2018. doi: 10.3847/2041-8213/aaf744.

Zhaohuan Zhu, Richard P. Nelson, Lee Hartmann, Catherine Espaillat, and Nuria Calvet. Transitional and Pre-transitional Disks: Gap Opening by Multiple Planets? , 729(1):47, March 2011. doi: 10.1088/0004-637X/729/1/47.

Zhaohuan Zhu, Ruobing Dong, James M. Stone, and Roman R. Rafikov. The Structure of Spiral Shocks Excited by Planetary-mass Companions. , 813(2):88, November 2015. doi: 10.1088/0004-637X/813/2/88.

Zhaohuan Zhu, Shangjia Zhang, Yan-Fei Jiang, Akimasa Kataoka, Tilman Birnstiel, Cornelis P. Dullemond, Sean M. Andrews, Jane Huang, Laura M. Pérez, John M. Carpenter, Xue-Ning Bai, David J. Wilner, and Luca Ricci. One Solution to the Mass Budget Problem for Planet Formation: Optically Thick Disks with Dust Scattering. , 877(2):L18, June 2019. doi: 10.3847/2041-8213/ab1f8c.

L. M. Ziurys, R. J. Saykally, R. L. Plambeck, and N. R. Erickson. Detection of the N = 3-2 transition of CCH in Orion and determination of the molecular rotational constants. , 254: 94–99, March 1982. doi: 10.1086/159709.

A. Zsom, C. W. Ormel, C. Güttler, J. Blum, and C. P. Dullemond. The outcome of protoplanetary dust growth: pebbles, boulders, or planetesimals? II. Introducing the bouncing barrier. , 513:A57, April 2010. doi: 10.1051/0004-6361/200912976.

Alice Zurlo, Lucas A. Cieza, Sebastián Pérez, Valentin Christiaens, Jonathan P. Williams, Greta Guidi, Hector Cánovas, Simon Casassus, Antonio Hales, David A. Principe, Dary Ruíz-Rodríguez, and Antonia Fernand ez-Figueroa. The Ophiuchus DIsc Survey Employing ALMA (ODISEA). II. The effect of stellar multiplicity on disc properties. , July 2020. doi: 10.1093/mnras/staa1886.

# Appendix A

# Additional Azimuthal cuts Spectral Index

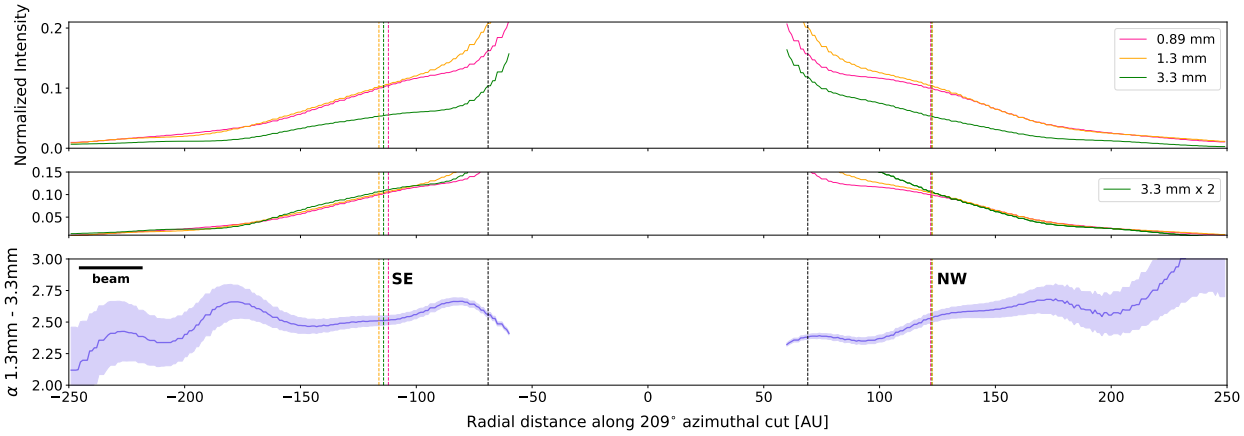


Figure A.1: Analogous to Figure 3.10, which showed an azimuthal cut along the azimuthal angle of maximum spiral contrast (224°). Here an azimuthal cut showing the emission and spectral index variations -15° from the location of maximum contrast.

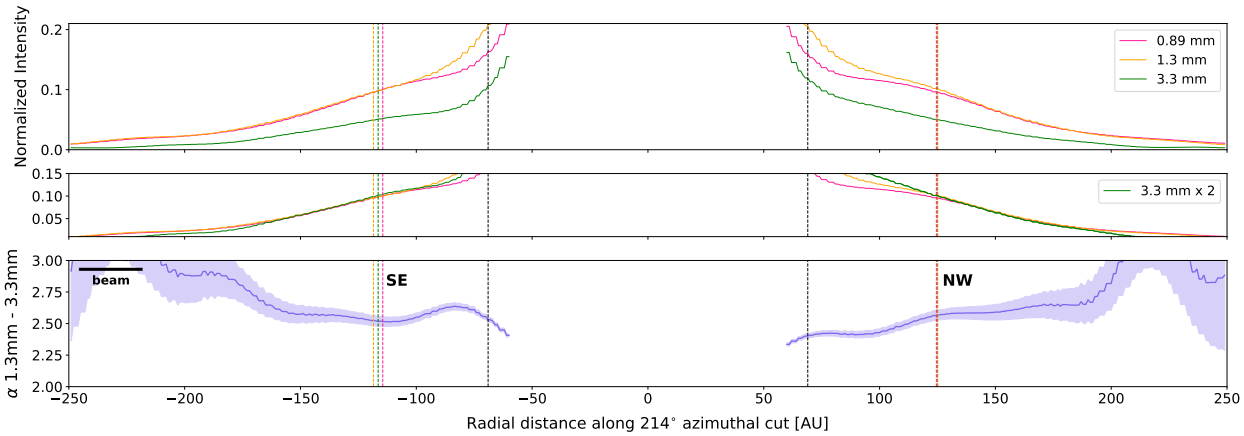


Figure A.2: Analogous to Figure A.1, showing azimuthal cut -10° from the location of maximum contrast.

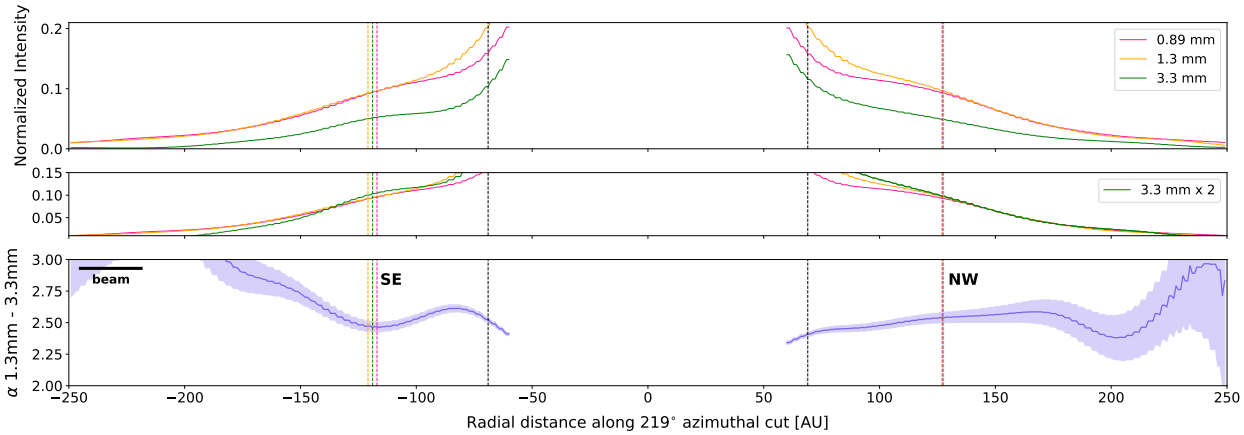


Figure A.3: Analogous to Figure A.1, showing azimuthal cut -5° from the location of maximum contrast.

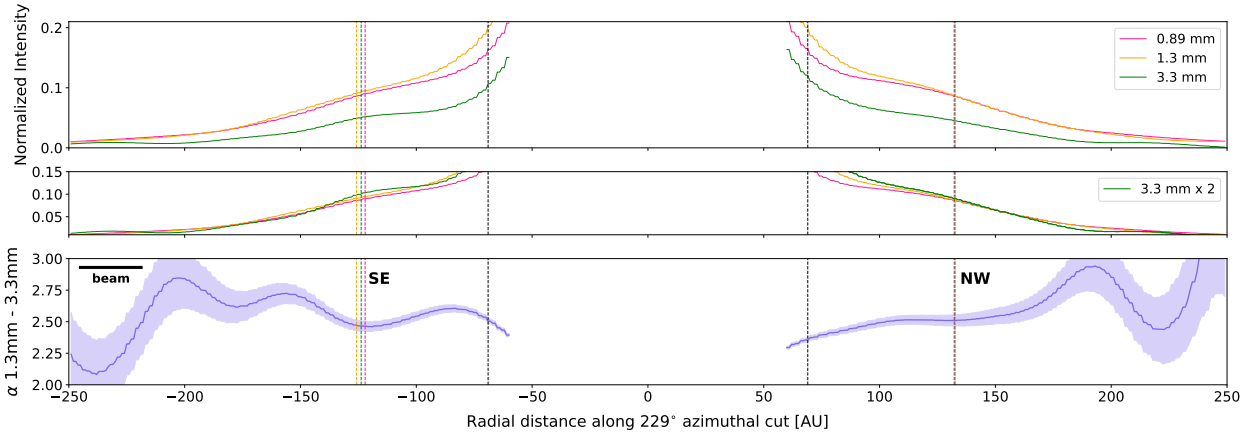


Figure A.4: Analogous to Figure A.1, showing azimuthal cut +5° from the location of maximum contrast.

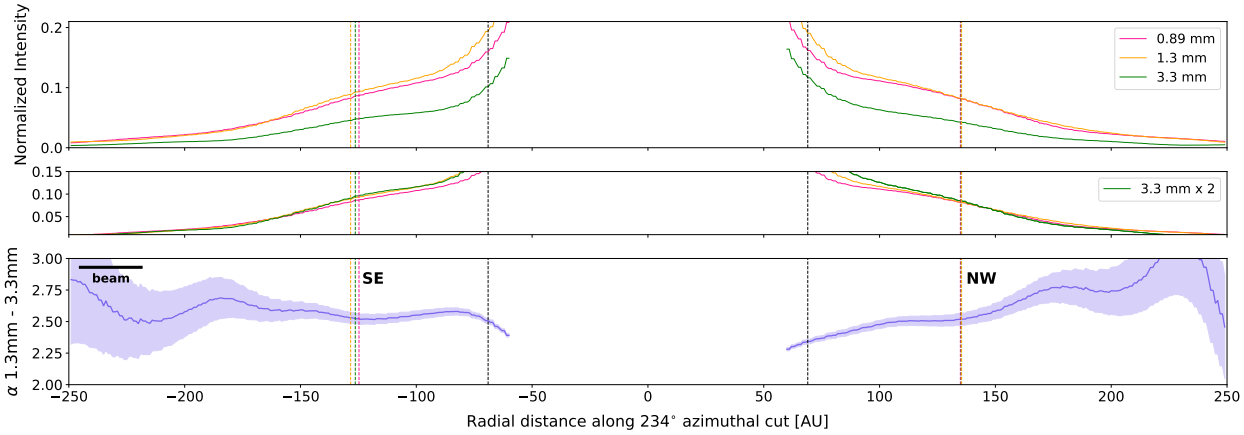


Figure A.5: Analogous to Figure A.1, showing azimuthal cut +10° from the location of maximum contrast.

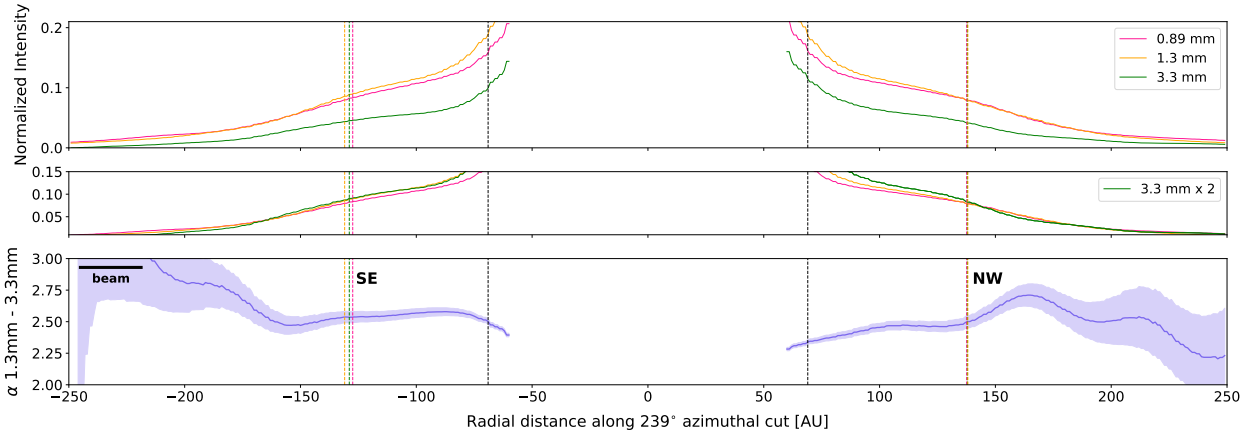


Figure A.6: Analogous to Figure A.1, showing azimuthal cut +15° from the location of maximum contrast.

# Appendix B

# Rejected SPH Simulations

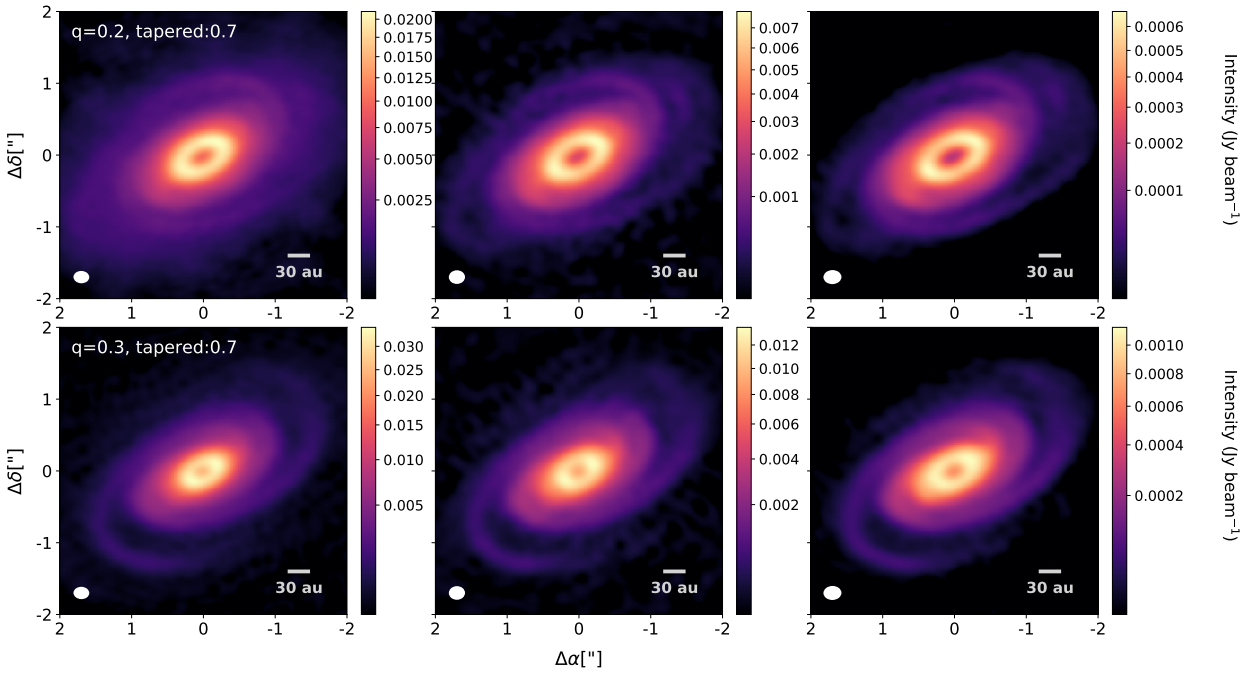


Figure B.1: All panels from Left to Right correspond to data from the 0.87mm, 1.3mm and 3mm simulated observations, each row corresponds to a simulation done with disk-to-mass ratio ($q$) and exponentially tapered dust density profile with $p$ index 0.7 indicated in top left corner of first panel. Images correspond to the simulated emission at each observed wavelength, beam is shown in the bottom left of each panel, and 30au scale for reference.

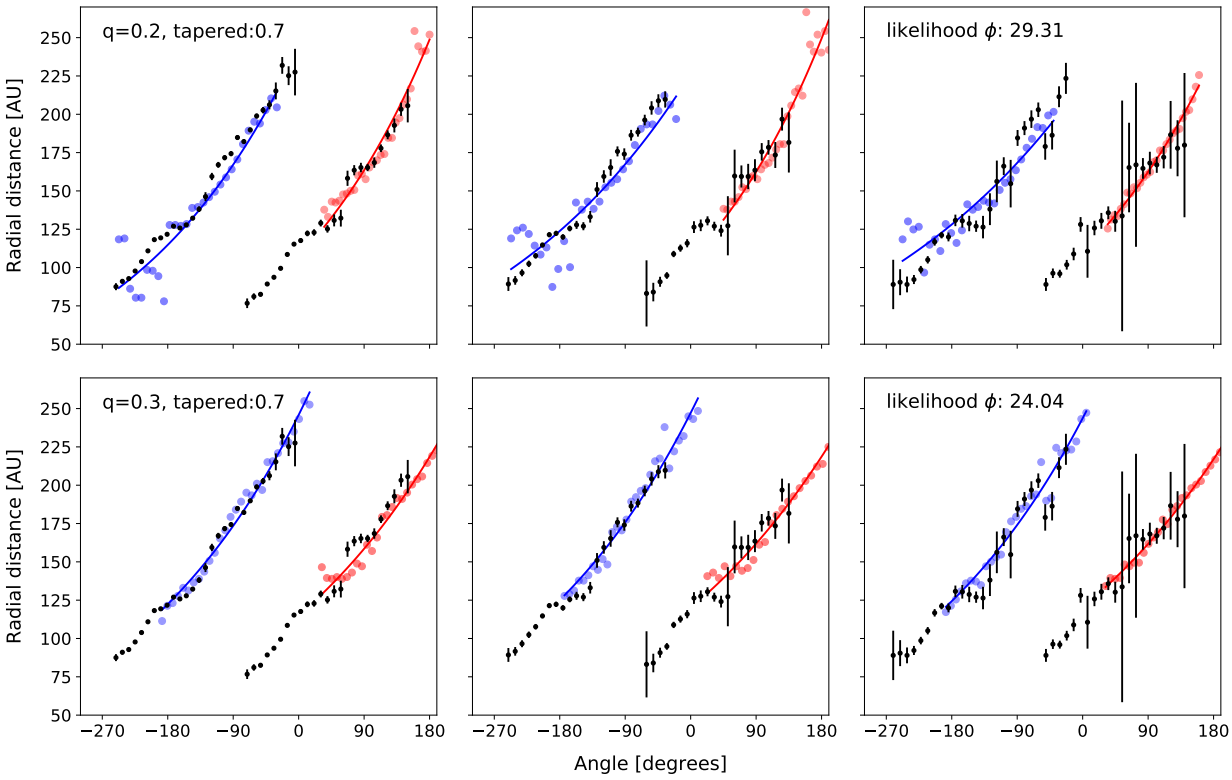


Figure B.2: Following the same distribution as Figure B.1, showing the deprojected radial location of the maxima along the simulated substracted images and the constant pitch angle logarithmic spiral fit to the data. Black data points are the deprojected radial location of the maxima found along the observed substracted image and their astrometric error. The pitch angle likelihood parameter is indicates in the top left corner of third panel in each row.

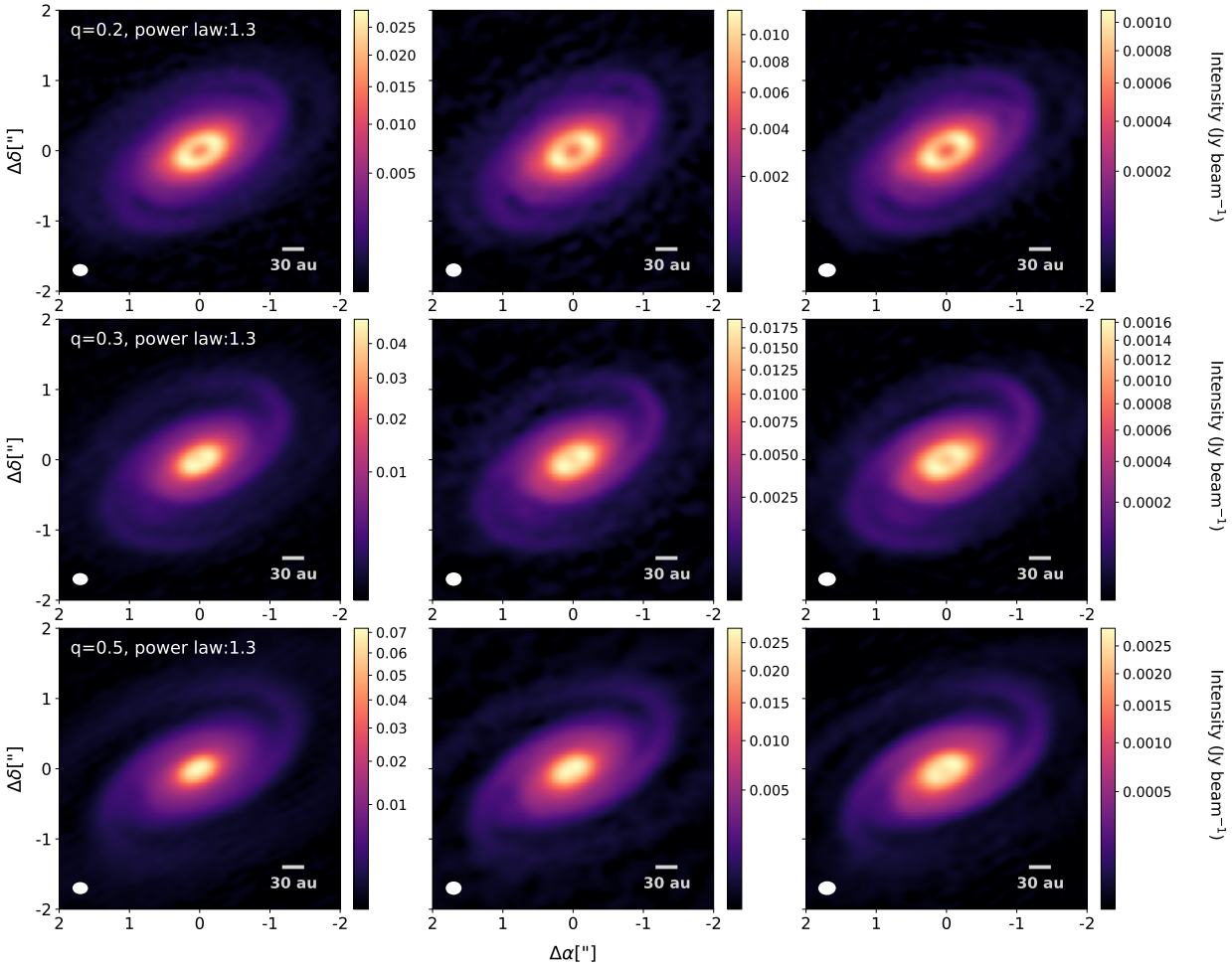


Figure B.3: Analogous to figure B.1 but for simulations done with a power-law dust density profile of index 1.3. Each row shows a different disk-to-mass ratio.

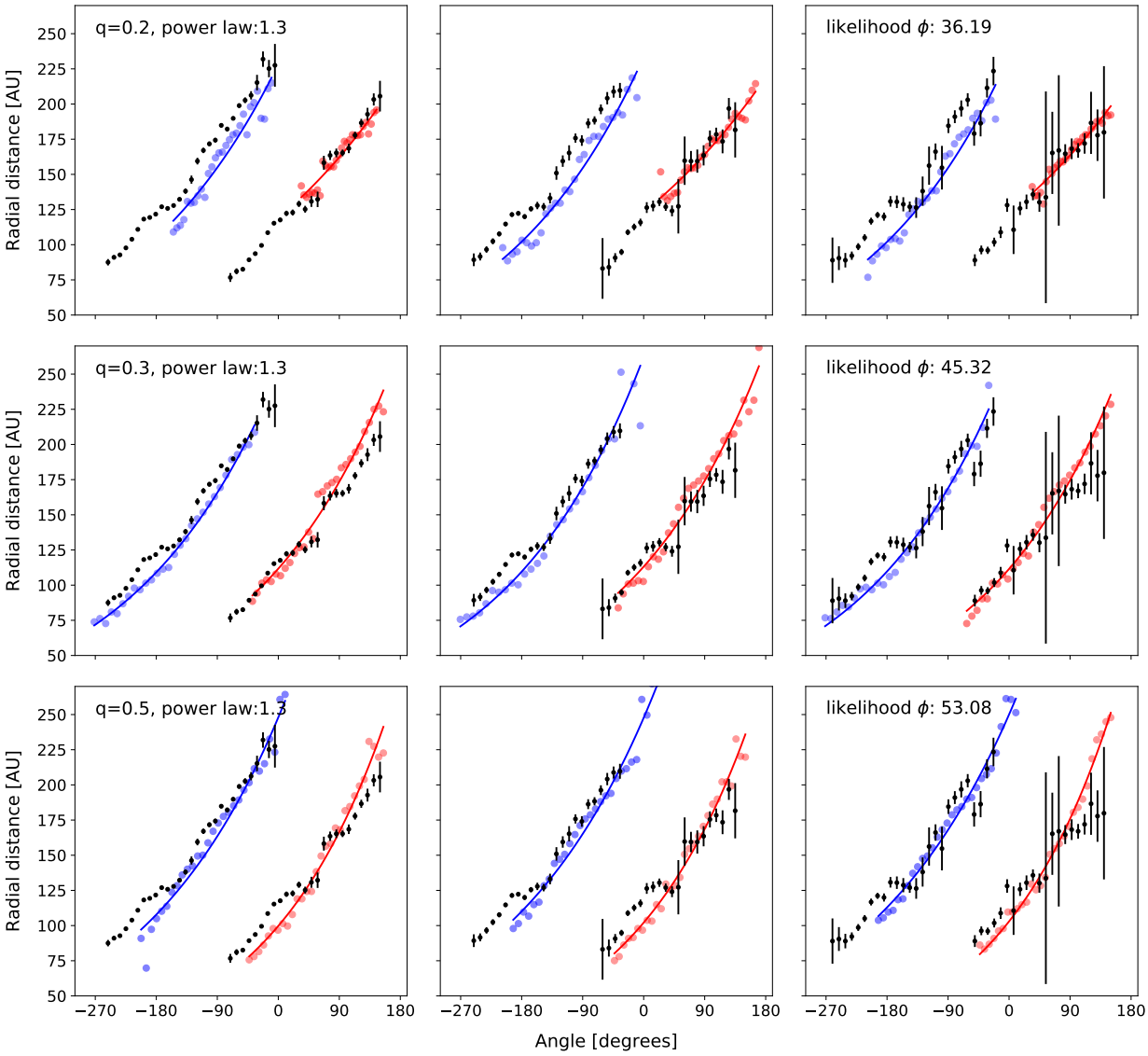


Figure B.4: Analogous to figure B.2 but for simulations done with a power-law dust density profile of index 1.3. Each row shows a different disk-to-mass ratio.

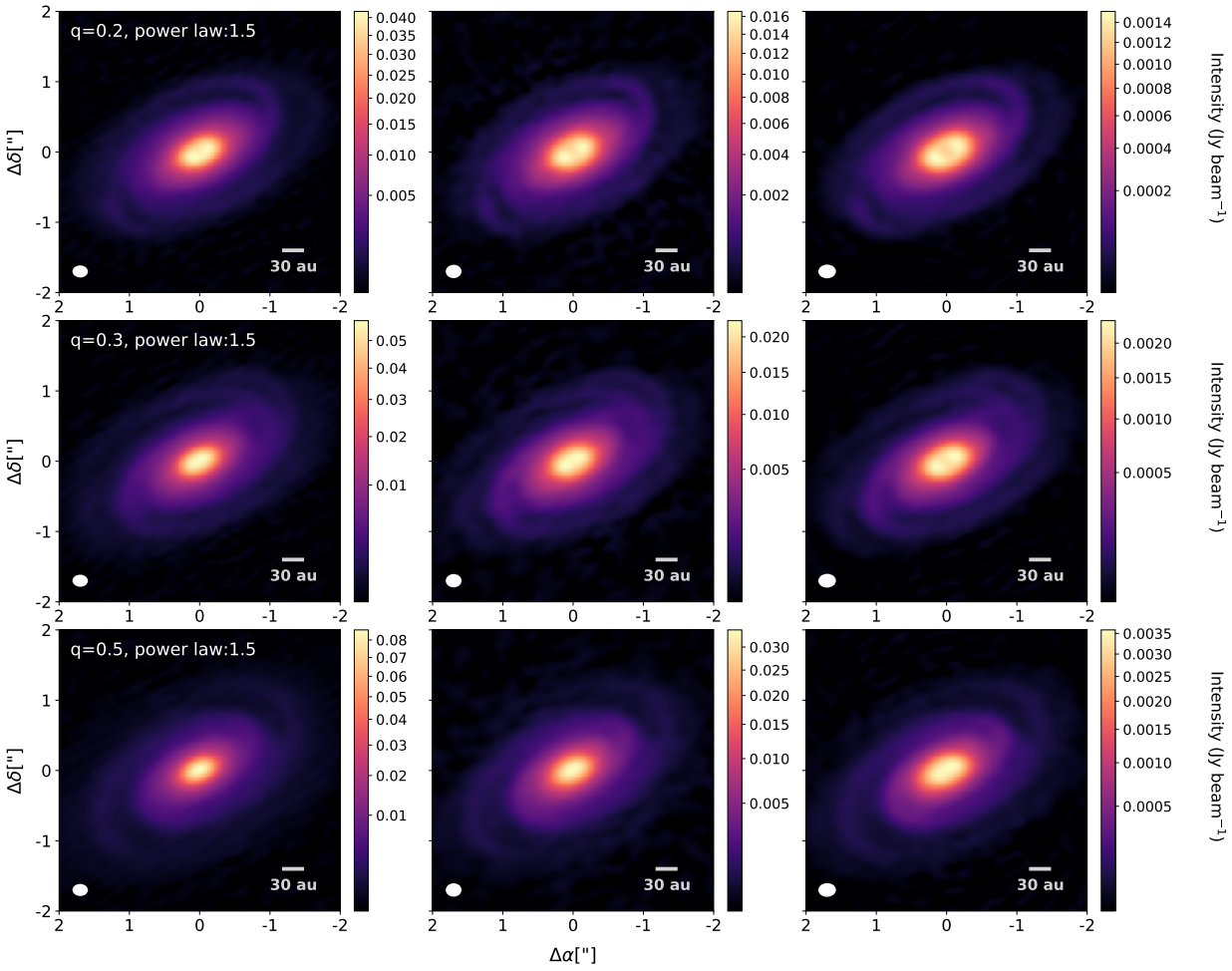


Figure B.5: Analogous to figure B.1 but for simulations done with a power-law dust density profile of index 1.5. Each row shows a different disk-to-mass ratio.

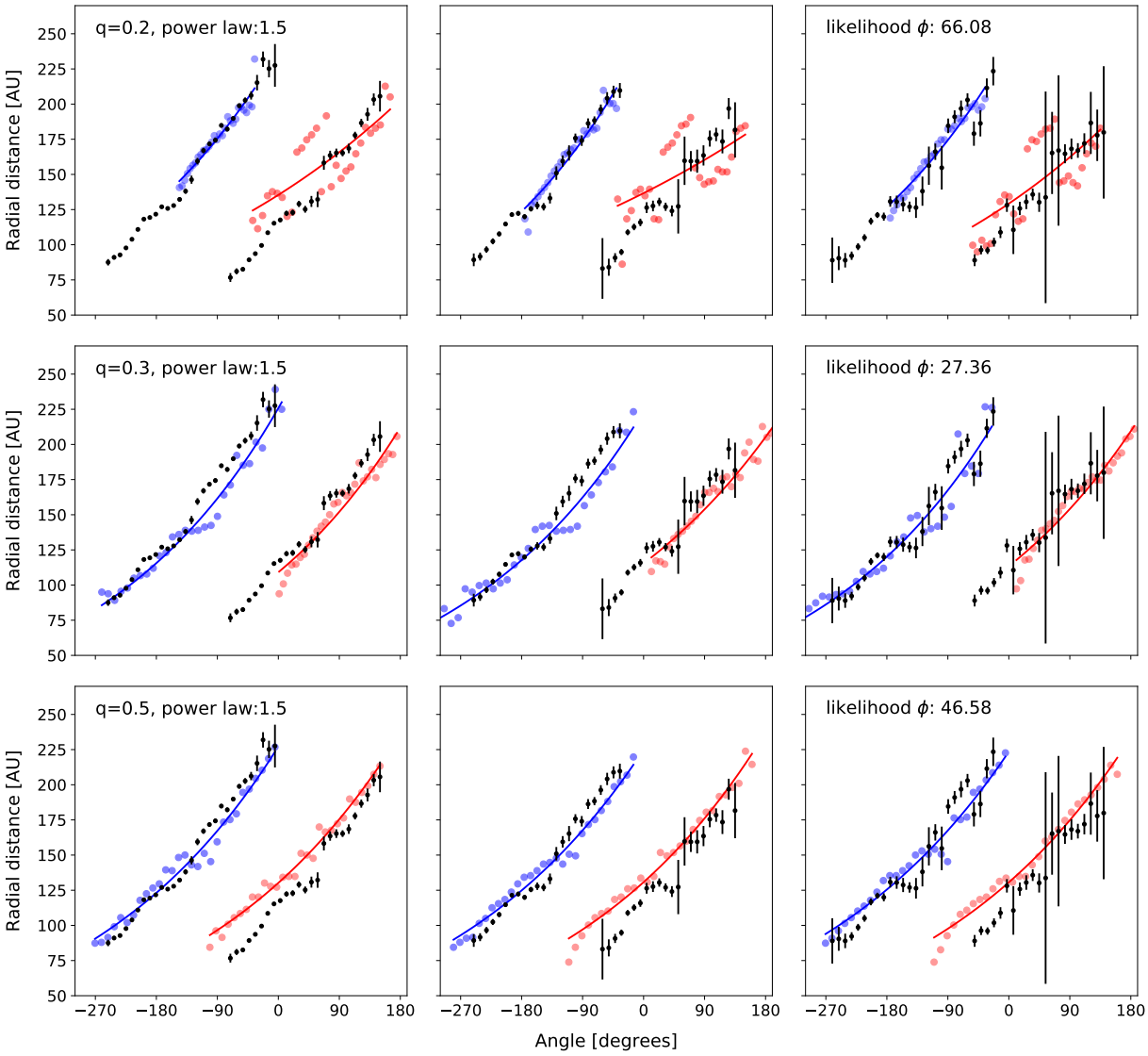


Figure B.6: Analogous to figure B.2 but for simulations done with a power-law dust density profile of index 1.5. Each row shows a different disk-to-mass ratio.